

Characterisation of Wood-Fibre–Based Materials using Image Analysis

Erik L. G. Wernersson
*Faculty of Forest Sciences
Centre for Image Analysis
Uppsala*

Doctoral Thesis
Swedish University of Agricultural Sciences
Uppsala 2014

Acta Universitatis agriculturae Sueciae
2014:99

ISSN, 1652-6880
ISBN (print version) 978-91-576-8146-1
ISBN (electronic version) 978-91-576-8147-8
©2014 Erik L. G. Wernersson, Uppsala
Print: SLU Service/Repro, Uppsala 2014

Characterisation of Wood-Fibre-Based Materials using Image Analysis

Abstract

Wood fibres are the main constituent of paper and are also used to alter properties of plastics in wood-fibre-based composite materials. The manufacturing of these materials involves numerous parameters that determine the quality of the products. The link between the manufacturing parameters and the final products can often be found in properties of the microstructure, which calls for advanced characterisation methods of the materials.

Computerised image analysis is the discipline of using computers to automatically extract information from digital images. Computerised image analysis can be used to create automated methods suitable for the analysis of large data volumes. Inherently these methods give reproducible results and are not biased by individual analysts.

In this thesis, three-dimensional X-ray computed tomography (CT) at micrometre resolution is used to image paper and composites. Image analysis methods are developed to characterise properties of individual fibres, properties of fibre-fibre bonds, and properties of the whole fibre networks based on these CT images.

The main contributions of this thesis is the development of new automated image-analysis methods for characterisation of wood-fibre-based materials. This include the areas of fibre-fibre contacts and the free-fibre lengths. A method for reduction of phase contrast in mixed mode CT images is presented. This method retrieves absorption from images with both absorption and phase contrast. Curvature calculations in volumetric images are discussed and a new method is proposed that is suitable for three-dimensional images of materials with wood fibres, where the surfaces of the objects are close together.

Keywords: image analysis, wood fibres, paper, wood-fibre-based composites, micro-computed tomography, curvature, phase contrast, microstructure

Author's address: Erik L. G. Wernersson, SLU, Centre for image analysis,
Box 337, SE-751 05 Uppsala, Sweden
E-mail: erikw@cb.uu.se

Contents

Notation and abbreviations	10
1 Introduction	11
1.1 Summary of the chapters	11
2 Characterisation of fibrous materials	13
2.1 Wood fibres	14
2.2 Approaches	15
2.3 Acquisition and pre-processing	18
2.4 Validation and simulations	19
2.5 Area of fibre-fibre bonds	19
2.6 Surface area, thickness and volume of paper sheets	20
2.7 Pulp-to-paper shrinkage	21
3 Digital Images	25
3.1 Derivatives	26
3.2 Segmentation and measurements	28
3.3 Scales and resolution	28
3.4 The Discrete Fourier transform	28
4 X-ray computed tomography	31
4.1 Geometric optics	32
4.2 Physical optics and diffraction	35
4.3 Absorption retrieval	37
4.4 Image quality and artefacts	39
5 Directional data	41
5.1 Directions from images	41
5.2 Representing directions and orientation	42
6 Surfaces and curvatures	47
6.1 Differential geometry of curves	48
6.2 Differential geometry of surfaces	50
6.3 Curvature in digital images from differentials	53
6.4 Curvature from orientation fields	55
6.5 Curvature signature of shapes	62
7 Maximal flow algorithms	65
7.1 Maximal flow in graphs	65
7.2 Maximal flow in continuous domains	67

8	Summary of the papers	71
9	Conclusions and future work	77
9.1	Summary of contributions	77
9.2	Future work	80
	Sammanfattning (in Swedish)	81
	Acknowledgements	83
	Appendices	
A	Parameters in the phase contrast filter	87
A.1	Derivation	87
A.2	Experiments	88
B	Series for KDEs on S^1 and S^2	91
B.1	S^1	91
B.2	S^2	94
B.3	Averaging and the diffusions equation	95
B.4	Orientation space construction	97
C	Jacobi's method	99
C.1	Algorithm and implementation	99
C.2	Discussion	101
	Bibliography	103

Enclosed Publications

This thesis is based on the following papers, which are referred to in the text by their Roman numerals.

- I E. L. G. Wernersson, M. N. Boone, J. Van den Bulcke, L. Van Hoorebeke and C. L. Luengo Hendriks, “Postprocessing method for reducing phase effects in reconstructed microcomputed-tomography data”, *Journal of the Optical Society of America A (JOSA A)*, vol. 30, no. 3, pp. 455–461, 2013
- II E. L. G. Wernersson, C. L. Luengo Hendriks and A. Brun, “Accurate estimation of gaussian and mean curvature in volumetric images”, in *3D Imaging Modeling Processing Visualization Transmission (3DIMPVT)*, Hangzhou, China, May 16-19, 2011, pp. 312–317
- III E. L. G. Wernersson, C. L. Luengo Hendriks and A. Brun, “Robust and unbiased curvature of isophote surfaces in volumetric images”, manuscript
- IV E. L. G. Wernersson, C. L. Luengo Hendriks and A. Brun, “Generating synthetic μ CT images of wood fibre materials”, in *Proceedings, 6th International Symposium on Image and Signal Processing and Analysis (ISPA)*, 2009, pp. 365–370
- V E. L. G. Wernersson, A. Brun and C. L. Luengo Hendriks, “Segmentation of wood fibres in 3D CT images using graph cuts”, in *Proceedings, Image Analysis and Processing, (ICIAP)*, ser. Lecture Notes in Computer Science, P. Foggia, C. Sansone and M. Vento, Eds., vol. 5716, Springer Berlin / Heidelberg, 2009, pp. 92–102
- VI E. L. G. Wernersson, S. Borodulina, A. Kulachenko and G. Borgefors, “Characterisations of fibre networks in paper using computed tomography images”, *Nordic Pulp & Paper Research Journal (NPPRJ)*, vol. 29, no. 3, pp. 468–475, 2014
- VII T. Joffre, A. Miettinen, E. L. G. Wernersson, P. Isaksson and E. K. Gamstedt, “Effects of defects on the tensile strength of short-fibre composite materials”, *Mechanics of Materials*, vol. 75, pp. 125–134, 2014
- VIII T. Linder, T. Löfqvist, E. L. G. Wernersson and P. Gren, “Light scattering in fibrous media with different degrees of in-plane fiber alignment”, *Optics Express*, vol. 22, no. 14, pp. 16 829–16 840, 2014

- IX J. Van den Bulcke, E. L. G. Wernersson, M. Dierick, D. Van Loo, B. Masschaele, L. Brabant, M. N. Boone, L. Van Hoorebeke, K. Haneca, A. Brun, C. L. Luengo Hendriks and J. Van Acker, “3D tree-ring analysis using helical X-ray tomography”, *Dendrochronologia*, vol. 32, no. 1, pp. 39–46, 2014

Reprints were made with permission from the publishers.

Related work

While working on this thesis, the author also contributed to the following work

Journal publications

- x T. Joffre, E. L. G. Wernersson, A. Miettinen, C. L. Luengo Hendriks and E. K. Gamstedt, “Swelling of cellulose fibres in composite materials: constraint effects of the surrounding matrix”, *Composites Science and Technology*, vol. 74, pp. 52–59, 2013
- xi A. Marais, M. S. Magnusson, T. Joffre, E. L. G. Wernersson and L. Wågberg, “New insights into the mechanisms behind the strengthening of lignocellulosic fibrous networks with polyamines”, *Cellulose*, pp. 1–10, 2014

Other work

- xii E. L. G. Wernersson, A. Brun and C. L. Luengo Hendriks, “Closing pores and segmenting individual fibres in 3D images of wood fibre composites using curvature information and graph cuts”, in *Proceedings, Symposium on Image Analysis (SSBA)*, J. Bigun and A. Verikas, Eds., Halmstad, Sweden, 2009, pp. 113–116
- xiii E. L. G. Wernersson, A. Brun and C. L. Luengo Hendriks, “Calculating curvature from orientation fields in volumetric images”, in *Proceedings, Symposium on Image Analysis (SSBA)*, R. Lenz, Ed., paper 26, 4 pp., Linköping, Sweden, 2011
- xiv M. Boone, E. L. G. Wernersson, M. Dierick, L. Brabant, E. Pauwels, C. L. Luengo Hendriks and L. Van Hoorebeke, “Comparison of several phase retrieval and phase correction methods for single-image in-line

X-ray phase contrast tomography”, in *Proceedings of IEEE 10th International symposium on biomedical imaging: From nano to macro*, abstract, San Francisco, CA, USA, 2013

- xv T. Joffre, E. K. Gamstedt, A. Miettinen and E. L. G. Wernersson, *Effects of fibre agglomeration on strength of wood-fibre composites*, Workshop: Mixed numerical and experimental methods applied to the mechanical characterization of bio-based materials, Vila Real, Portugal, April 27-28, 2011
- xvi E. L. G. Wernersson, M. N. Boone, J. Van den Bulcke, L. Van Hoorebeke and C. L. Luengo Hendriks, “Understanding phase contrast artefacts in micro computed absorption tomography”, in *Proceedings, Symposium on Image Analysis (SSBA)*, Luleå, Sweden, 2014, pp. 40–45

Notation and abbreviations

a, b, c	lower case for scalars
$\mathbf{a}, \mathbf{b}, \mathbf{c}$	bold face for row vectors
A, B, C	upper case for matrices and sets
$A \otimes B$	Cartesian product
$\langle \mathbf{a}, \mathbf{b} \rangle$	scalar product
$\mathbf{a} \times \mathbf{b}$	cross product
$\ \mathbf{a}\ _N$	L^N -norm of \mathbf{a}
$\ \mathbf{a}\ $	short for $\ \mathbf{a}\ _2$
a^T, A^T	vector and matrix transpose
a^*, A^*	vector and matrix conjugate transpose
$\angle a$	angle of a
$\text{Tr} A$	trace of A
$ a $	absolute value of a
$ M $	determinant of M
$A \cup B$	union of set A and B
$A \cap B$	intersection of set A and B
\emptyset	the empty set
$f * g$	N -dimensional convolution of f by g
$\mathcal{F}\{f\}$	the Fourier transform of f
$\mathcal{O}(p)$	complexity, Ordo p
\mathbb{Z}	the set of integers
\mathbb{R}	the set of real numbers
$\mathbf{1}$	the unit matrix
CT	X-ray Computed Tomography
FFT	Fast Fourier Transform
FST	Fourier Slice Theorem
FBP	Filtered Back Projection
KDE	Kernel Density Estimator

1 Introduction

The use of wood precedes most technology ever developed. Nowadays wood is not only a source of energy and a construction material, wood is also the primary source of fibres for paper making. Wood fibres are also used to reinforce plastics in wood-fibre-plastic composites. This thesis focusses on these two applications: paper, and wood-fibre-based composite materials.

The cultural impact of paper is vast and the use of paper has in a long time been linked to economic growth. Since the Fourdrinier machine was invented in the 19th century, most paper is made from wood fibres. Paper is not just one material. There is an overwhelming number of formats and qualities, ranging from toilet paper to glossy photo paper. Much of the difference between these products can be found in the microstructure and be characterised in terms of geometrical properties of fibres and in the way that fibres organise in the paper sheets.

The motivation for the work presented in this thesis is to develop automated methods for characterisation of wood-fibre-based materials using three-dimensional images calculated from X-ray projections. For most of the methods that are presented, images with a resolution around 1 μm has been used. At this resolution, individual fibres can be seen and much of the individual fibre structure is revealed, including the hollow interior, *lumen*, when it is not collapsed. Knowledge about overall configuration of wood fibres can also be gained at this resolution since the images can have a side length of up to 4 mm.

Information about fibres and their organisation can be used to give insight about paper, composites and other wood-fibre based materials. This thesis provides methods that extract information from paper and composites and with this information, mechanical models can be refined and manufacturing techniques diagnosed and optimised. Hopefully, a whole array of new ideas can spark off this thesis.

1.1 Summary of the chapters

Chapter 2 describes which properties of wood-fibre-based materials that can be measured from CT images, using automatic and semi-automatic methods. This chapter constitutes the core of the thesis and motivates the other chapters in the thesis as well as all the included publications.

Chapter 3 reviews the basis concepts of digital image analysis used in this thesis.

Chapter 4 contains a brief review of electromagnetic waves and a dis-

discussion on the relation between the imaged object and the digital image. Then the main concepts X-ray computed tomography is introduced, which are the Fourier Slice Theorem and the Filtered Back Projection. Last, phase contrast is introduced and discussed in the context of absorption retrieval.

Chapter 5 reviews how local orientation in digital images can be estimated. It also contains a discussion on how orientation can be averaged over small regions. In particular, histograms, the structure tensor and kernel density estimators are mentioned.

Chapter 6 starts from curvature of a line and then introduces curvature concepts related to two-dimensional surfaces that can be found in three-dimensional space. Focus is on curvature estimation for surfaces that are sampled in volumetric images.

Chapter 7 is about minimal cuts that can be calculated from maximal flows. Minimal cuts are formulated both for graphs and for continuous domains and it is discussed how they can be used for image segmentation.

Chapter 8 contains a list of the included papers together with details on each authors's contributions.

Chapter 9 contains the conclusions that can be drawn from the work in this thesis and the related publications. The chapter also contains some ideas on how this work can be continued and extended.

The appendices contain details on specific issues that did not fit into the chapters. Appendix A shows how to find parameters for the absorption retrieval filter, Chapter 4, from image features. In Appendix B, the series expansions for the kernel density estimators on circles and spheres, which are used in Chapter 5, are discussed. In Appendix C I discuss how and why Jacobi's method should be used to find the eigenvalues and eigenvectors of the structure tensor, (relates to Chapters 5 and 6).

2 Characterisation of fibrous materials

In this chapter it will be discussed how to measure properties of materials that contain wood fibres from CT images. More precisely, paper and composite materials where fibres are mixed with a plastic material will be discussed.

Paper is a material with a surprisingly complex structure. It consists of a network of fibres, mostly from wood, which are to a large extent randomly distributed. Properties of both individual fibres and the fibre network are important to the final products. There are many parameters involved in paper making. Some alter the overall fibre organisation while others change properties of individual fibres. Most paper is made from softwood species, and especially spruce. In the *pulping* stage, solid wood is decomposed into its fibres. The fibres are later deposited, dispersed and dried before they can be recognised as paper. Each of these steps has its own set of parameters, and the production is even more complicated since fillers and coatings can be applied as well. For optimization of yield and quality it is essential to know how the manufacturing parameters affect the end product, and especially *why*.

Three-dimensional CT images of wood-fibre-based materials can be used to characterise both individual fibres and the fibre network. The first study of paper using these premises was done by E. J. Samuelsen et. al in 1999 [94]. CT has, since then, become more accessible, as discussed in Chapter 4, and is nowadays commonly used in paper characterisation labs.

There are other imaging techniques, besides CT, which are used to study fibre-based materials *in situ*. They involve light microscopy and scanning electron microscopy (SEM) [27]. Fibres can also be studied *ex situ*. For example, wood fibres can be dissolved in fluid and imaged as they pass a thin tube in front of a microscope [60].

It is possible to make three-dimensional volumetric images of paper by cutting paper sheets with a microtome and then imaging the slices with scanning electron microscopy (SEM). The images of the slices are then digitally assembled to a volumetric image. This was first done in 2002 [3] and has since then been used again in a few studies [125]. CT imaging is very time efficient compared to that procedure. The resolution in the images cannot match that of SEM, however, the CT images are not distorted by cutting. A comparison between imaging modalities can be found in [7].

Segmentation of wood fibre has much in common with segmentation of blood vessels [72] and techniques designed for segmentation of arteries have with some success been applied to wood fibres [3]. Both wood fibres and blood vessels are hollow in a natural state and have varying diameters.

Nevertheless, methods designed for blood vessels are likely to fail for many wood fibres since blood vessels have a more regular structure and wood fibres that have gone through the manufacturing steps involved to make paper or wood-fibre-plastic composites.

This chapter contains a review of available image analysis algorithms for characterisation of wood-fibre-based materials such as paper and composites of plastics and wood fibres. My contributions to this research area can be found in Papers IV, V, VI, VIII and, indirectly, in Paper IX, where possible uses of helical-CT for wood analysis are developed. The chapter begins with a section that describes wood and wood fibres. After that follows a classify of the approaches used to characterise fibrous materials from CT images. Lastly, a few specific issues of imaging and characterisation are discussed.

2.1 Wood fibres

The world production of paper was about 400 000 000 tonnes in 2012 [44], which makes it an important trade product. Most paper is made from wood fibres but also other plant fibres can be used including cotton, bamboo and oil palm.

Wood fibres are cells in tree trunks and consist of cellulose (40–44%), hemicellulose (15–32%) and lignin (18–35%). In softwood species, which are most important for paper making, most of the volume is filled with *longitudinal tracheids*. They are slender cells with an aspect ratio of about 1 to 100. The average diameter is 25–45 μm , and the average length 3–4 mm, see Fig. 1. The tracheids are hollow, and the inside is called *lumen*. The cell walls have pits with thin membranes that connects them to the neighbouring cells.

The growth rate of trees, and tree cells, follows the cycle of the year. Since wood grows in the cambium, just below the bark, this give rise to annual rings, which can be used for dating, or *dendrochronology*. In Paper IX, we have investigated how densiometric profiling can benefit from helical X-ray CT. We found that it can avoid biases inherent in two-dimensional conventional imaging and it also requires less sample preparation.

To make paper from wood involves several processing steps. First of all, the wood has to be converted to pulp, i.e., be fiberised, which is usually done by the sulfate (Kraft) or sulphite process. The pulp is then washed to remove impurities, and possibly bleached. To get strong bondings between the fibres, it is beneficial if they are flattened and have a rough surface. These properties are gained by *beating* and *refinement*. Lastly, the pulp is formed into a sheet by deposition onto a screen before it is finally dried by pressing

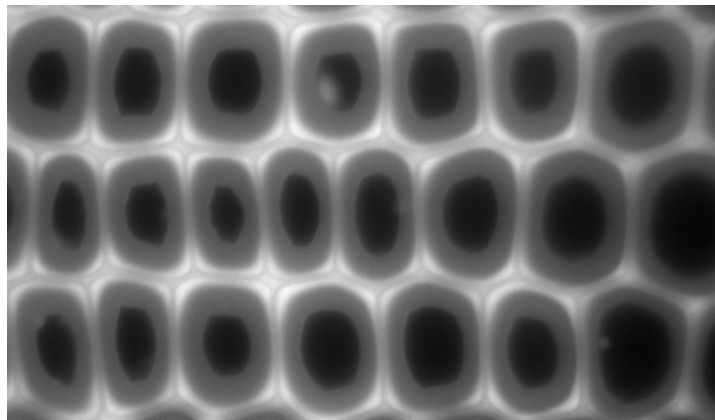


Figure 1: Microscopy image of wood cells from a cross section of pine (a blue filter was used). Normal cells have a diameter of 25–45 μm . [image by Bettina Selig]

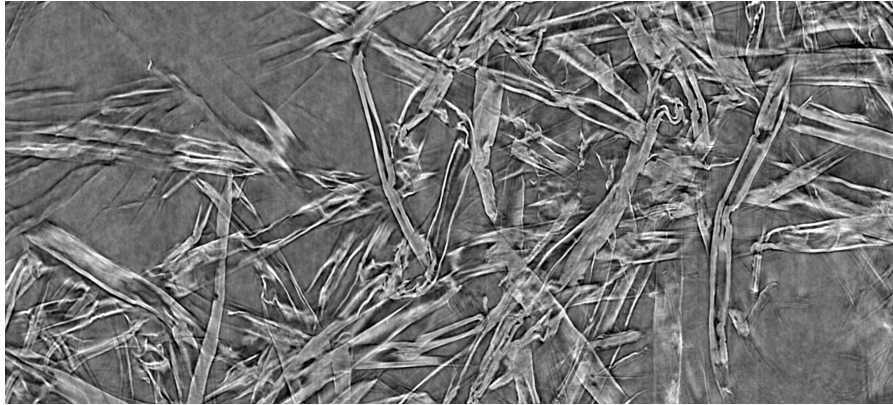
and heating. For a more detailed description, see [58]. See also Fig. 2–a for a tomogram of a paper.

Wood fibres can also be used to alter properties of polymers. When wood fibres are mixed into plastic they make a *composite* material, see Fig. 2–b. Composite materials can be made stronger and lighter than pure plastics while also containing a larger portion of renewable material. The main downside of using wood fibres in plastics is an increased sensitivity to moisture. Uneven mixing of wood fibres is also a potential problem. In paper VII, we have investigated how defects in terms of clusters of wood fibres alters the strength of composites.

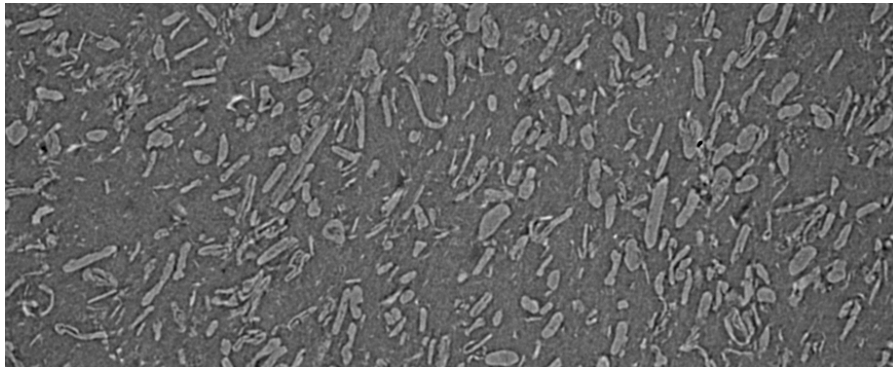
The processing steps, when making composite materials and paper, change the shape of wood fibres, which makes subsequent analysis hard. Lumen collapse and the pith membranes break. Fibres also break, flatten and deform into shapes that are hard to describe in words.

2.2 Approaches

When all individual fibres in a CT image of a paper or a composite are identified, most measurements are readily available. Unfortunately, it is not so easy to separate the fibres. An ultimate goal of fibre and fibre network characterisation from CT images could be stated as *Find and label all individual fibres*. The modality itself makes this an unreachable goal. CT images are records of X-ray absorption and hence it is not possible to see where one fibre ends and another begins when they are bonded. Neither is it possible



(a)



(b)

Figure 2: a) A tomogram of a sheet of paper, slightly tilted. [image by Joanna Hornatowska, Innventia, Stockholm] b) A tomogram of a composite material. [captured at the Swiss Light Source (SLS) at the Paul Scherrer Institut (PSI)]

to identify fines (split fibres or small cells), which adheres to fibres, based on absorption solely. The resolution is simply too low and there is no difference in absorption between two fibres that are pressed together and two fibres that bond.

The interest in these characterisation problems has resulted in several theses [3, 7, 37, 106] and a growing number of publications. I've attempted to classify their goals (implicitly or explicitly stated) and have come up with the following categories:

1. *Concentrate on overall properties:* Overall properties that do not depend on labelled fibres include the distribution of pores (the pore network), measurements of individual pores [100], density, and orientation [6]. Also surface location falls under this label; it is a prerequisite for calculating density, see Fig. 3 for an example. In paper VIII we have estimated the orientation of wood fibres in paper sheets, to validate a novel theoretical model for light scattering in fibrous materials.
2. *Find as many fibres as possible:* All methods that start out with this goal seem to miss a fraction (large or small). This is, or is not, important for the following analysis depending on what is of interest. Work with such starting point include [56, 61]. I would also like to add reference [113] under this label. It presents, what looks like, a complete segmentation but not enough details are given for a reproduction of the results.
3. *Find the extension of seeded fibres:* This approach is also known as tracking. Starting from some location of a fibre such methods aim to find the rest of the fibre. Most attempts use two-dimensional cross sections [8, 38] but there is at least one approach that is fully three-dimensional [5].
4. *Measure properties of already segmented fibres:* This an expedient problem since the hardest task is assumed solved. But it is of course vital that such methods are available, developed and ready for segmented fibres [30, 81, 105].
5. *Measure properties from coarsely segmented fibres:* This us our approach described in Paper VI. Fully automatic segmentation seems unreachable and manual segmentation too time consuming. This approach is based on a coarse but fast manual segmentation and then employs automatic measurements.

6. *Separate coarsely segmented fibres:* The underlying assumption is that it is easier to find some approximations to the segmentation problem first and later refine the segmentation. Lumen has e.g., been used as a clue to where fibres are. This can never give a complete segmentation of fibres since the lumen do not remain in all fibres in paper and composites. There are methods designed for 2-D cross sections [4] as well as 3-D images [119, 120].
7. *Manual measurements from images:* Except for being time consuming, error prone and non-repetitive, this approach makes a good use of the human brain. Such an approach is used, e.g., in [87] where corners of quadrilaterals are marked manually and the quadrilaterals are used to approximate fibre bond areas.
8. *Evaluation and simulations.* A few papers focus on questions like: How precise are the methods? Within what ranges should we expect this parameter? How will noise effect this approach? and so on. A little more will be said about that in section 2.4.

2.3 Acquisition and pre-processing

The goal of X-ray imaging and pre-processing is to get a faithful record of the X-ray absorption within the sample. This representation, or volumetric image, should be sampled according to the Nyquist rate to make use of sub-pixel precision. It is however common that binary images are used instead. This might be because some algorithm in the processing chain is only defined for binary input or output.

If CT images are acquired in absorption mode, i.e., if the detector has been close to the sample, relatively little preprocessing has to be done. If the image is noisy, it has to be filtered, for example with a low pass filter, which is the most general approach. However, filters that make use of homogeneity have been found to be better alternatives [46, 73], including bilateral filtering [108].

If the image is acquired in mixed mode, i.e., if both absorption and phase contrast is present, there are more pre-processing alternatives. To get a well sampled image of the absorption, the phase contrast can be removed with the technique of Paper I, but it can also be done prior to reconstruction [15].

If the image is purely in phase contrast, conclusions about absorption have to be drawn based on the interface bands or fringes. For wood fibres, such procedure has been employed by C. Antoine et al. [1], but the best

alternative is likely to be the approach by Malmberg et al. [85]. No comparison has been done between these two methods but the former processes the image line by line while the later is fully 3-D.

2.4 Validation and simulations

There is no reference data set for wood fibre segmentation. Hence, there is no good way to compare the performance of characterisation methods against each other. There are several reasons why no such data set is available. 1) Someone has to create a ground truth segmentation, and that means manual segmentation, which is very time consuming. 2) Fibres are different; they are processed in different ways and the manufactured materials are also different. 3) There are several pre-processing options and also different imaging modalities.

Reason number (2) and (3) above implies that more than one reference data set is required to cover all situations, but even just one would have been very useful. We have simulated individual wood fibres with varied morphology, including pores, to generate reference images in Paper IV, and also packed them together. We have also studied some of the common artefacts, which are inherent to micro-meter-resolution CT imaging in Paper IV, and can include them in simulations of CT images of wood-fibre based materials. There are also other approaches to fibre network simulations, using solid tubes [114] and based on theoretical predictions [47].

2.5 Area of fibre-fibre bonds

Paper is held together where fibres are bonded, and these bonds cannot be seen in CT images. Based on CT images it is however possible to measure the area of contact, not knowing if it is bonded or not. Since the exact contact interface cannot be imaged, some educated guess has to be done.

We have defined the area of contact between two fibres as the surface of minimal area between them. Minimal surfaces are calculated by continuous graph cuts as described in Chapter 7. This work was initialised in Paper V and further developed in paper VI. The approach has since been used to study the effect of polyallylamine hydrochloride absorption onto the surface of unbleached kraft pulp fibres [86]. The method requires seeding, more specifically the area of the seeds has to be larger than the bond area. This condition can be verified after the bond area has been calculated.

There is another alternative for fibre-fibre areas assessments, based on ray casting [84]. It is, however, not invariant to the orientation of the volumetric image. A fully manual approach has been suggested in [87], where

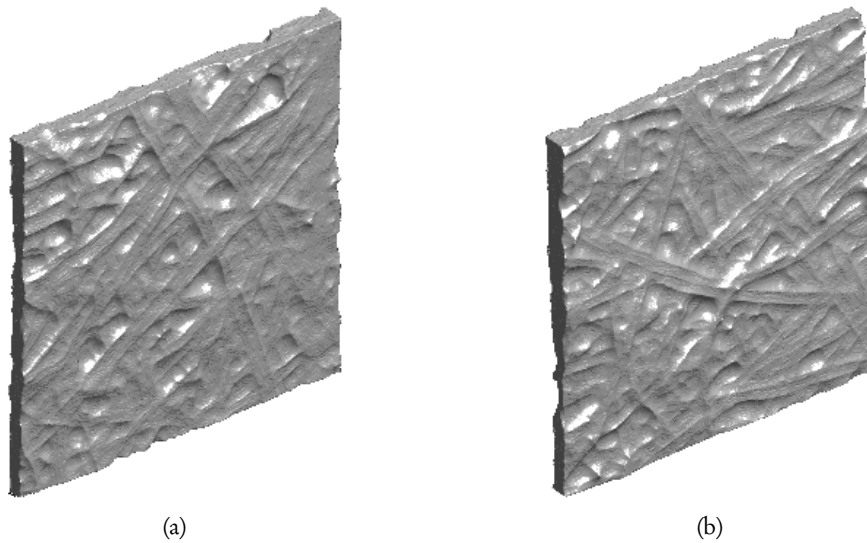


Figure 3: Two paper sheets of about 1×1 mm. A morphological closing with a spherical structuring element of radius $30 \mu\text{m}$ has been applied to define the surfaces.

the fibre-fibre areas are found by marking out corner points of a quadrilateral.

2.6 Surface area, thickness and volume of paper sheets

To define the surface of paper sheets is necessary prior to any calculations of area, thickness and volume. This is somewhat problematic since surfaces (and surface areas) are fractal. Accordingly, surface localisation depends on the resolution used. The fractal properties of surfaces can usually be neglected, e.g., according to ISO 216, an A0 sheet is defined to have an area of 1 m^2 . In this case, the area is the area spanned by the corners of the sheet, and the surface is assumed to be perfectly flat. At a smaller scale, the surface is hilly, or uneven, as seen in Fig. 3.

Since the area depends on scale, precise measurements can only be given with reference to a scale. Using morphological closing, scale can be defined with reference to the size of a rotationally invariant 3-D structuring element.

2.7 Pulp-to-paper shrinkage

Volumetric images of paper only cover small parts of sheets and hence the distribution of fibre lengths measured from such images does not correspond to the true distribution of fibre lengths in the full paper sheets. In this section, we describe how the distribution of the full-length fibres can be estimated.

The tool for fibre selection presented in Paper VI can be used to calculate the fibre length distribution in paper samples, which we call \mathcal{L}_M . We require that there is an estimation of the fibre length distribution prior to paper making. Such distributions can be sampled from dissolved fibres, as discussed earlier. We will denote this distribution \mathcal{L}_W . Then we simulate how fibres are dispersed onto a sheet, as they are when used in paper production. Then we measure the distribution of lengths within in a ROI of this (virtual) sheet, which we call \mathcal{L}_S .

If fibres did not shrink in the paper making process, \mathcal{L}_M and \mathcal{L}_W would be identical. But paper is dry, and pulp is wet, so we expect that $\mathcal{L}_W(x) = c_1 \mathcal{L}_M(c_2 x)$, where c_1 is a normalisation parameter, $c_1 > 1$, and c_2 is a scale parameter, $c_2 < 1$. By simulating paper deposition, using a range of shrinkage, it is possible to find the actual shrinkage from pulp to paper by comparing length distributions. The simulations can be made even more realistic by including the orientation distribution of the fibres, which can be found by several methods, see Paper VIII.

The simulation tool in this section is not previously published and hence this description is quite detailed.

Forward simulation

Fibres in the simulated sheet are represented by their end points, **a** and **b**. To avoid biases, fibres will be measured only within a region of interest that is placed in the middle of a larger sheet such that the padding is larger than the maximal fibre length. The fibre length distribution used in the simulations is denoted \mathcal{L} , and is a scaled version \mathcal{L}_W . The distribution of fibre directions is denoted \mathcal{T} .

Fibres, represented by their end points **a** and **b**, are placed in the sheet by the following procedure:

1. The fibre end point **a** is picked randomly within the sheet.
2. The direction θ is picked randomly in the interval $[0, 2\pi]$ or sampled from \mathcal{T} , if supplied.
3. The fibre length, l , is sampled from the measured fibre length distribution, \mathcal{L} .

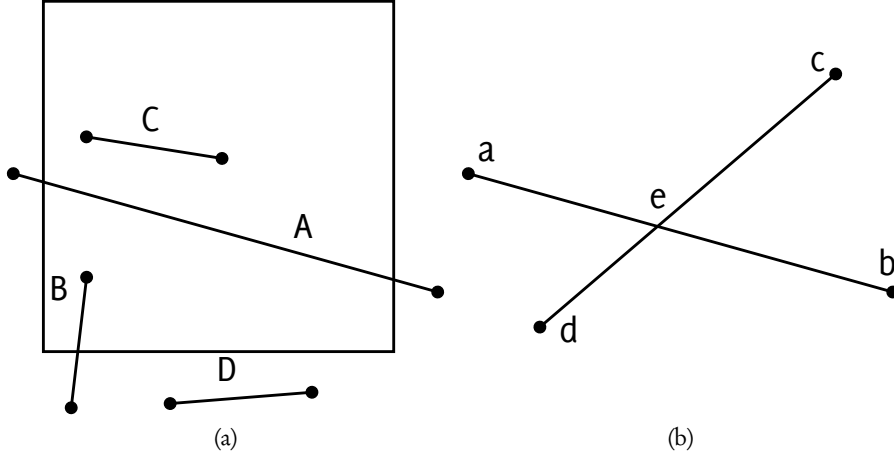


Figure 4: a) The different cases of fibre placement relative to the ROI. b) Illustration for the intersection algorithm.

4. The other end point $\mathbf{b} = \mathbf{a} + l(\cos \theta, \sin \theta)$.

To find out the length of each fibre within the ROI, three cases have to be considered, which are illustrated in Fig. 4-a:

1. The fibre intersects with two of the edges. The length is then determined as the distance between the intersections.
2. The fibre intersects with one of the edges. Then the length is defined as the distance between the intersection and the end point within the ROI.
3. No intersections. This means that the fibre is completely inside or outside the ROI and that no length is obtained or that the length between the end points should be used.

A graphical representation of a simulation is shown in Fig. 5.

Intersections

If the lines in Fig. 4-b are represented by constant vectors, \mathbf{p} , and a direction, \mathbf{t} , then the intersection between the lines numbered 1 and 2 are:

$$\mathbf{p}_0 + k_0 \mathbf{t}_0 = \mathbf{p}_1 + k_1 \mathbf{t}_1, \quad (1)$$

or in vector form

$$\begin{pmatrix} t_{0x} & -t_{1x} \\ t_{0y} & -t_{1y} \end{pmatrix} \begin{pmatrix} k_0 \\ k_1 \end{pmatrix} = \begin{pmatrix} p_{1x} - p_{0x} \\ p_{1y} - p_{0y} \end{pmatrix}, \quad (2)$$

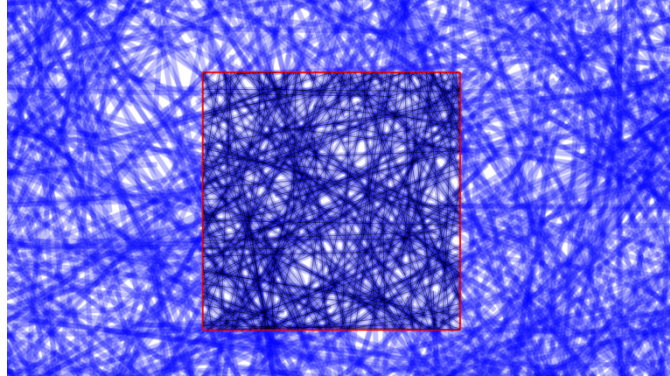


Figure 5: Example of how the simulation results can be visualised, showing the ROI as a box and fibres as transparent bars.

and the point of intersection, \mathbf{e} , is given by $\mathbf{e} = \mathbf{p}_0 + k_0 \mathbf{t}_0$. If $k_0 > 0$ and $k_0 < \|c - d\|$, the line segments intersect.

Inside or outside

To determine if a point, \mathbf{a} , is inside a shape S or not, the following procedure can be used. First, find a point, \mathbf{b} , which is not in S . This can be done by simply taking a point far away from S . Then the number of intersections of the line \mathbf{ab} and S are calculated with the algorithm described above. If the number of intersections is odd, the point \mathbf{a} is inside S .

Results

Simulation results (i.e., measured lengths, \mathcal{L}_S) are compared to actual measurements from CT images, \mathcal{L}_M , as shown in Fig. 6. The simulations are based on a distribution of fibre lengths, \mathcal{L}_W , that was measured from the pulp prior to paper making. The ROI is 1×1 mm and the domain is planar. The plots indicate that the length of the fibres in the CT image is about 50% to 75% of the length in dry state.

It seems that a rather simple procedure can be used for the simulation of paper networks to get estimates of length, or at least shrinkage. The length distribution from the simulations has a higher proportion of short fibres than what is measured in the CT images. We do not know the reasons for this, but it is known that the measurements from pulp have a high variation [60]. It is also possible that very short fibres are hard to see and select manually and that \mathcal{L}_M is biased.

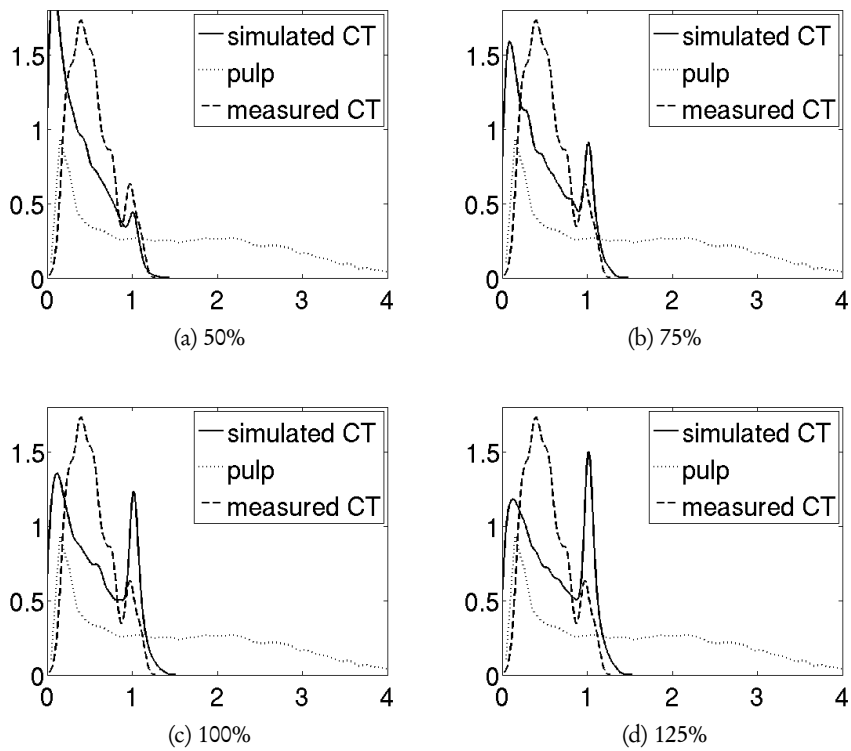


Figure 6: Simulations with different scaling of the input length distribution. 250 000 fibres were used in the simulations and about 8 500 that fell into the ROI were measured. Pulp: length distribution measured on wet fibres. Measured CT: Using the method of Paper VI.

3 Digital Images

In popular culture, digital images can be infinitely enhanced and are believed to contain small sharp-cornered squares. This chapter takes a more technical standpoint and introduces some of the fundamental image processing methods that are used in the later chapters. There are several textbooks that reviews the basics of digital image processing and image analysis, e.g., [50, 102].

A *digital image*, I is a mapping from a finite and metric lattice D , to a finite, ordered and possibly multi-dimensional set, R . The lattice points will be called *pixels*, which is short for picture elements. If we let $F_k = \{0, 1, \dots, k\}$ denote the set of positive integers up to k , and form Cartesian product by $F_{\alpha} = F_{\alpha_1} \otimes F_{\alpha_2} \cdots$, $\alpha = [\alpha_1, \alpha_2, \dots]$ then the mapping can be expressed as

$$I : F_{\alpha} \rightarrow F_{\beta}. \quad (3)$$

The mapping in Eq. 3 includes gray scale images where $\beta = [k]$, k typically 2^8 or 2^{16} , RGB images where $\beta = [\beta_1, \beta_2, \beta_3]$ as well as two-dimensional (2-D) images where $\alpha = [\alpha_1, \alpha_2]$ and 3-D images where $\alpha = [\alpha_1, \alpha_2, \alpha_3]$. In this work, most of the images are three-dimensional (3-D) and usually of the type where $\alpha = [1024, 1024, 1024]$ and $\beta = [2^{12}]$.

The range of a digital image is discrete but it is common practice to extend it, or embed it, in the space of real numbers to get a comfortable ring structure [55]. This is then approximated by floating point numbers in our computers, with several consequences, which can not be neglected, especially cancellation effects [57].

It is common to extend the domain of the image from the lattice to a line, surface or volume by interpolation, i.e., define $I^*(\mathbf{x}) = d(I, \mathbf{x})$ where $\mathbf{x} = (x_1, x_2, \dots, x_n) \in \mathbb{R}^n$ and d is an interpolation function. The choice of interpolation function is important and will influence most calculations. Some of the most common interpolation types are:

- nearest neighbour,
- linear interpolation,
- cubic interpolation,
- spline interpolation, and
- Lanczos interpolation.

Digital images often contains samples of a continuous signal, S , and therefore it is quite natural to embed the domain. A sampled image is described by

$$I(\mathbf{x} \in D) = (S * p)(\mathbf{x}), \quad S : \mathbb{R}^{|\alpha|} \rightarrow \mathbb{R}^{|\beta|}, \quad (4)$$

where $*$ denotes convolution and p is the *sampling kernel*. An imaging system can often be described by a certain p , which can often be approximated by either:

- δ , the Dirac impulse functional in the point sampling model,
- $[-.5, .5]^{|\beta|}$, a unit box in the partial coverage model [101], or,
- G_σ , a Gaussian kernel in the signal processing model.

We will only use isotropic Gaussian kernels, G_σ located at $\mathbf{0}$, given by

$$G_\sigma(\mathbf{x}) = (\sigma \sqrt{2\pi})^{-k} \exp\left(\frac{-1}{2\sigma^2} \langle \mathbf{x}, \mathbf{x} \rangle\right), \quad (5)$$

where σ denotes the standard deviation and $\langle \cdot, \cdot \rangle$ denotes the scalar product.

The sampling function is usually dictated by the imaging system, and an appropriate interpolation function can be selected based on that function.

The point sampling model has the important property that S is exactly representable by I when the Nyquist sampling theorem is satisfied. This means that given the right choice of d ,

$$I^*(\mathbf{x}) = S(\mathbf{x}), \quad (6)$$

if and only if S is band-limited and D is dense enough. From now on, we drop the star notation and write simply I instead of I^* since there will always be, at least potentially, an interpolation function available. As we will see, the interpolation function has consequences for low level operations, which in turn are important for high level analysis.

3.1 Derivatives

With the usual definition of the right side derivative dI/dx of a one-dimensional function,

$$\frac{dI}{dx} = \lim_{h \rightarrow 0} \frac{I(x+h) - I(x)}{h}, \quad (7)$$

and using nearest neighbour interpolation, we see that the expressions in Eq. 7 are zero on all grid points, where x is an integer. When linear interpolation is used between the grid points, the image can locally be described by

$f(x) = a_0 + a_1x$ on $[0, 1]$, with the derivative, $f'(0) = a_1 = I(x + 1) - I(x)$ while higher order derivatives are zero. This result is also obtained by setting h , the denominator of Eq. 7, to 1. Using quadratic interpolation, $f(x) = a_0 + a_1x + a_2x^2$ on $[-1, 1]$, and $f'(0) = a_1 = .5(f(1) - f(-1))$. This result can be derived from the following linear equation system

$$\begin{pmatrix} f(-1) \\ f(0) \\ f(1) \end{pmatrix} = \begin{pmatrix} 1 & -1 & 1 \\ 1 & 0 & 0 \\ 1 & 1 & 1 \end{pmatrix} \begin{pmatrix} a_0 \\ a_1 \\ a_2 \end{pmatrix}, \quad (8)$$

with the solution

$$\begin{pmatrix} a_0 \\ a_1 \\ a_2 \end{pmatrix} = \begin{pmatrix} 0 & 1 & 0 \\ -1/2 & 0 & 1/2 \\ 1/2 & -1 & 1/2 \end{pmatrix} \begin{pmatrix} f(-1) \\ f(0) \\ f(1) \end{pmatrix}.$$

A consequence of this is that images have to be interpolated by polynomial of order two or higher for second order derivatives to be non-zero. Also more points are needed for higher order derivatives. These results are also valid for images of higher dimensions.

Derivatives enhance noise, or high frequency components of the Fourier spectra. Hence it is often beneficial to low pass filter digital images before or after the derivatives are calculated. This can be done by, for instance, convolving the image with a Gaussian kernel to get a low pass filtered image, I_σ , by

$$I_\sigma(I, \sigma) = G_\sigma * I. \quad (9)$$

As a result, the derivatives can be calculated by

$$\frac{\partial I_\sigma}{\partial x} = \frac{\partial}{\partial x} (G_\sigma * I) = \frac{\partial G_\sigma}{\partial x} * I, \quad (10)$$

which means that the derivative operation can be applied to the Gaussian kernel rather than to the sampled image.

The value of σ must small, to keep the filter support small. On the other hand, it can not be too small since then the Gaussian kernel will be badly sampled. It has been argued that σ should be at least 0.9 [111]. To calculate derivatives, Eq. 10 is only one of several options. However, this option is, separable into one-dimensional filters, which makes it fast and also rotationally invariant. It is also optimal for detecting step edges in noisy images [26].

3.2 Segmentation and measurements

To delineate certain objects in images is called *segmentation* and is one of the fundamental tasks of image analysis. That which is not the objects of interest is usually called background when there is no other, application specific, name available.

Segmentation by *thresholding* can be used when the objects of interest have a distinct intensity, higher or lower than the background. When the objects are distinguished by a high intensity, they can be defined by

$$O = \{\mathbf{x}, I(\mathbf{x}) > t\}, \quad (11)$$

where t is the *threshold value*. The set O can then be analysed in several ways to produce *measurements* of the image. It is common to separate it into subsets or components by discrete connectedness.

Many methods do not only classify individual grid points as object or background but are able to draw smooth boundaries, which partially cover individual pixels. These methods are said to have *sub-pixel precision* and among them are, continuous graph cuts [2] and level sets [98].

Graph cuts are used for segmentation in Paper V and VI and will be described in Chapter 7.

3.3 Scales and resolution

It is often desirable to simplify images and remove small details. This is natural when the *resolution* or detail level of the image is such that the smallest detail that can be resolved is smaller than the smallest object of interest.

The resolution of a microscope is an example of the *scale* at which details can be resolved. A Gaussian filter can be used to digitally simulate the effect of a lower resolution microscope This demonstrated in Fig. 7 and much is written about this approach in the literature [69, 74, 126].

Mathematical morphology can also be used for image simplification, besides a large range of other applications. It relies on non-linear filtering of mainly two types: erosions and dilations, which do as the names suggests – erode and dilate digital objects. The filters can be realised in many ways and tailored to specific applications; they can also be combined sequentially to form openings and closings, which visually open up holes and remove small details or vice versa [97].

3.4 The Discrete Fourier transform

The *discrete Fourier transform* (DFT) is a special case of the Fourier transform [22] where the domain is finite and the signal is regarded as periodic.

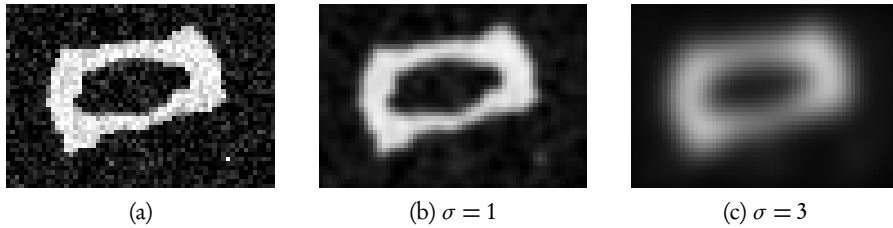


Figure 7: A cross section of a wood fibre shown in (a). Low-pass filtered with a Gaussian kernel determined by σ , according to Eq. 9, in (b) and (c). This is just one out of many ways to alter the contents of an image.

The *fast Fourier transform* (FFT) is a clever method for calculating the DFT components. It was first discovered by C. F. Gauss [59], but rediscovered and made popular by J. W. Cooley and J. W. Tukey [32] who explained how to implement it efficiently on a computer. For a one-dimensional image with side length N , the cost to convolve with a filter with side length M ($M < N$) is $\mathcal{O}(MN)$, if the convolution is performed directly. Using the FFT, the cost is $\mathcal{O}(N \log N)$, which is cheaper, in terms of the number of operation, for large M . For three-dimensional images, the direct convolution cost is $\mathcal{O}(N^3 M^3)$, which is reduced to $\mathcal{O}(N^3 \log N)$ using the FFT.

The fastest way to calculate linear filters is not always through the Fourier transform. This is sometimes dictated by the desired boundary effects. Recursive filters are preferential in some cases, see for example G. Farneback and C.-F. Westin [43]. And sometimes direct convolutions are fastest, for small M .

4 X-ray computed tomography

Tomograms (ancient greek: τόμος – tomos, "slice, section", γραφω – graphō, "to write") are two-dimensional images that depict the inside of matter and can be computed from projection images of X-ray absorption; the term *X-ray computed tomography*, or shortly CT, refers to this technique. Consecutive tomograms constitute volumetric images that map three-dimensional coordinates to X-ray absorption. This technique is non-destructive but samples have to be small enough to fit in the field of view of the camera, and usually have to be cut into small pieces for micro-metre resolution images.

Several inventions were crucial for the development of CT. Most of all the discovery of X-rays by W. C. Röntgen in the 1890s. Then came the development of the X-ray tube in the early 1900s, which creates radiation without radioactive elements. Theoretical work on line integrals, including an inversion formula was done by J. Radon in 1917 [92] and A. M. Cormack developed the theoretical foundations of CT scanning in the 1960s [33, 34]. Another essential component is the development of integrated circuits and the modern computer. Fast circuits are needed since CT is computationally heavy. The first CT scanner was built by G. Hounsfield with medical uses in mind, at Electric and Musical Industries Ltd (EMI) in the early 1970s. At the time of writing, synchrotrons are the best X-ray sources; the quality of their radiation makes it possible to create tomograms with sub-micrometre resolution. Synchrotrons are enormous machines of which only a few exist in the world. Table-top systems have appeared as an attractive alternative. They can be bought from commercial manufacturers, are relatively small, and can be operated by a single person. Nevertheless, X-ray beams in table-top systems are less bright and have a much wider spectrum compared to the beam of a synchrotron. Therefore, table-top systems produce lower quality images, which makes subsequent image analysis more difficult.

Light propagation in matter is a complex phenomenon and analytic solutions are only available for a few cases. For all other cases, Monte Carlo methods [75] or simplifications are used. CT relies on the latter strategy and employs a geometric view on optics. The inverse problem, where a tomogram is created from projection data is usually called a tomographic reconstruction. Most reconstructions are made with the filtered back projection (FBP) algorithm and its spawns; which one depends on the geometry of the source, object and detector. It has been shown that the mean square reconstruction error for FBP is close to a theoretical minimal bound. The bound was derived independently to the reconstruction method, which means that no big improvements can be expected from any other method [65]. Nevertheless, the image quality got better over time, which can be explained

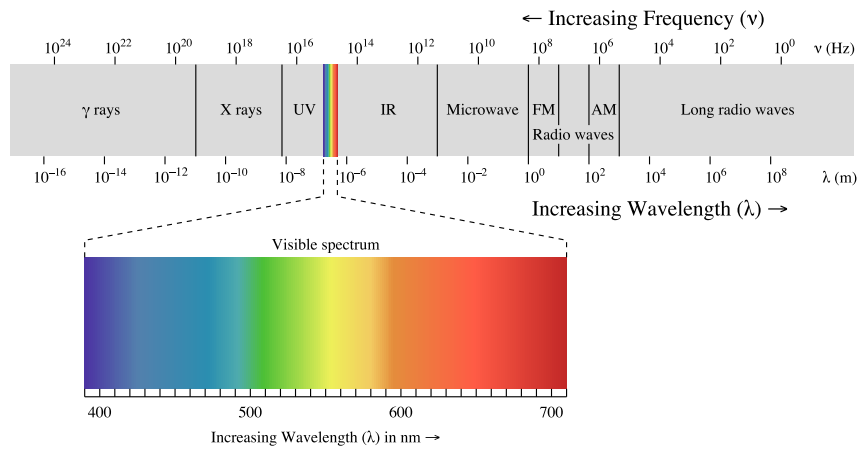


Figure 8: The electromagnetic radiation in a vacuum. The light in X-ray imaging is found between γ radiation and ultra violet. [© CC BY-SA 3.0]

by mainly three factors: The X-ray sources and detectors get better, which lowers the noise levels, increases the resolution and possibly eliminates ring artefacts. Second, we get better at the tomographic reconstructions, both by incorporating information about the imaged objects, such as homogeneity, [104], and by better handling of incomplete and corrupted data, e.g. compressive sensing has shown to outperform traditional reconstruction techniques when the measurements are noisy and incomplete [28, 40]. Finally, more accurate physical models of the X-ray propagation are used.

The basics of X-ray imaging and computed tomography techniques will be described in this chapter. Most of this material can also be found in the references [18, 54, 65, 77]. This background is relevant to all included papers, especially for Paper IV where we characterise and simulate noise in synchrotron CT, and for Paper I where we retrieve absorption from CT images with diffraction artefacts.

4.1 Geometric optics

X-rays are electromagnetic waves that principally behaves like ordinary visible light. However, the frequency is too high for human eyes to see, and X-rays penetrate deeper into most materials than visible light (see Fig. 8 for a comparison).

Visible light is commonly understood as travelling in straight paths.

The straight-path model a good description when the wavelength is much shorter than the size of imaged objects. Optical theory, in which light is treated as straight lines is usually called *geometrical optics*. Equivalently, light can be treated as small as small particles, in *corpuscular theory* [18].

The filtered back projection algorithm (FBP) is used for reconstruction of parallel beam CT, and is the basis for other reconstruction algorithms that correspond to other geometries, see Fig. 9. FBP takes projection images as input and is used to calculate tomograms as well as volumetric images, which can be seen as consecutive tomograms.

The FBP founded on geometrical optics where light is treated as straight lines. To derive the FBP, we also need to know how these lines interact with matter, which is described by the Beer–Lambert law, which again is a simplification. No other physical laws are used and notably neither reflections nor refraction.

The Beer–Lambert law states that when a ray that passes through some material, with an attenuation coefficient, $\mu(\mathbf{x})$, along a straight path, p , intensity the intensity changes from I_0 to I by

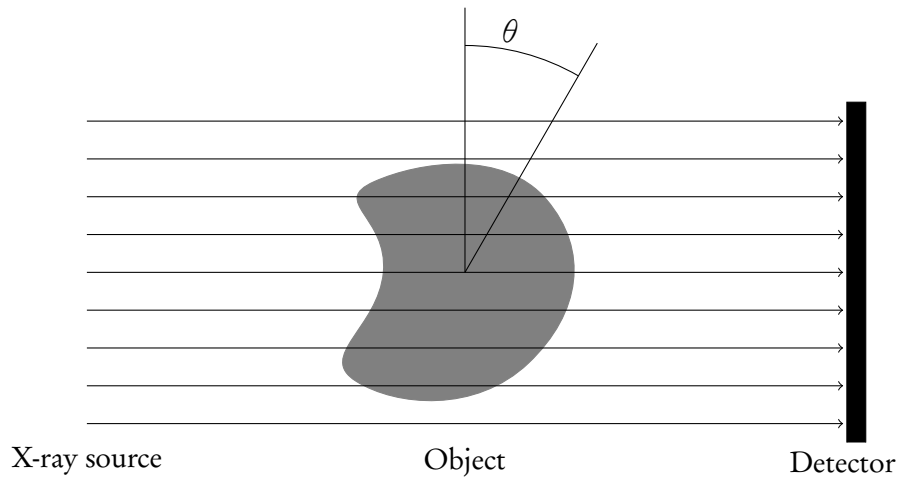
$$I = I_0 \exp \left(- \int_p \mu(\mathbf{x}) \right). \quad (12)$$

The attenuation along p is found from Eq. 12 and is by

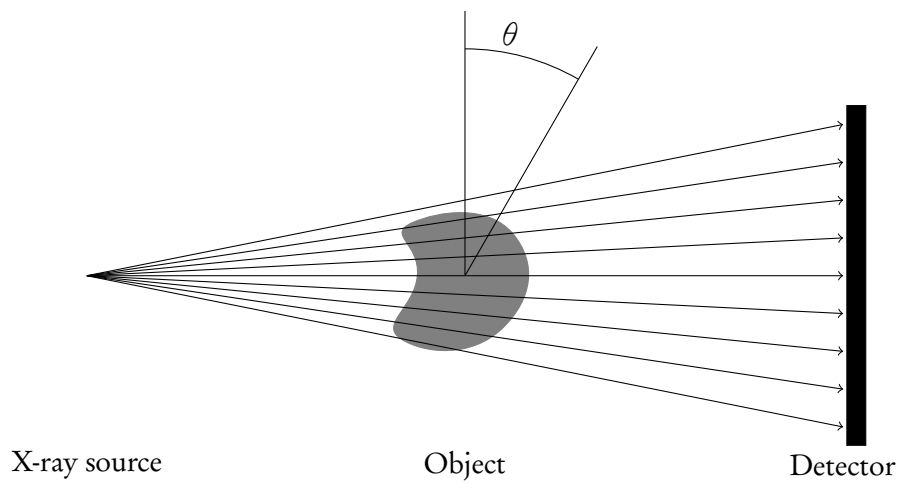
$$\int_p \mu(\mathbf{x}) = - \ln(I/I_0). \quad (13)$$

An average value along a path through μ corresponds to a point of $\mathcal{F}(\mu)$ since averages correspond to zero frequency. A straight X-ray that is sent through an object will correspond to a single point and an array of straight and parallel lines through an object gives a line in $\mathcal{F}(\mu)$. This is also the essence of the Fourier Slice Theorem (FST) [65] that says that the Fourier transform of a one-dimensional projection of a two-dimensional function is equivalent to a line of the Fourier transform of the two-dimensional function.

Since each projection image provides a line in $\mathcal{F}(\mu)$, it can be populated by multiple projections from different angles. When the object is rotated and projected throughout 180 degrees by fine increments, the object is completely described, together with some interpolation. However, the sample density is highest toward the centre of the Fourier domain so the samples have to be weighed. To weight the samples according to the density and then inversely transform them by the FFT, is the foundation of the FBP. In



(a)



(b)

Figure 9: Two possible geometries of CT machines are displayed by a few X-ray paths from source to detector through a sample. a: Parallel beams. b: Fan beam in two dimensions or a cross section of the three-dimensional cone beam geometry.

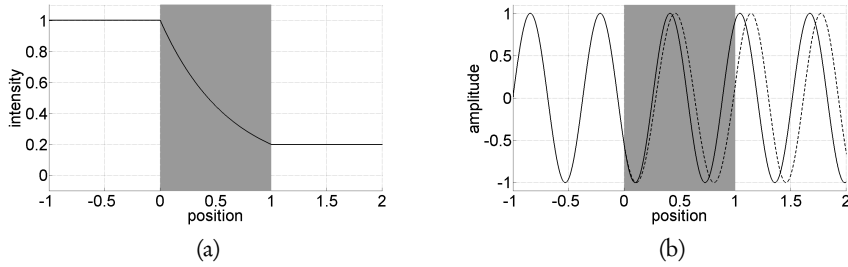


Figure 10: Both amplitude and phase change when light traverses most things but a vacuum. a: The amplitude is decreased according to the Beer-Lambert law, when passing the object shown in grey. b: The phase is delayed; both delayed (solid line) and non delayed phase (dotted line) shown.

principle, this description is also valid for cone- and parallel beam CT if the samples are re-arranged.

4.2 Physical optics and diffraction

Due to the model commonly used in CT, all variations in light are assumed to be caused by absorption of X-rays; diffraction is not part of the model. The wave nature of light has to be incorporated into the physical model of the tomograph for a differentiation between these two phenomena. This can be done by introducing phase into the calculations. In this section, we will allow objects to both absorb intensity and change the phase of the light that passes through; as illustrated in Fig. 10. We start the discussion with what happens at an object, and directly after it. We proceed with how the light field changes while it travels to the detector.

At the object

We assume that the sample is thin. It has to be thin since we will neglect any scattering within the sample. An incoming, plane, coherent and monochromatic wave will be denoted $U(x, y)$ where it meets the object. Then the wave is transformed by the sample, which is described by a complex function $S(x, y)$, to produce $T(x, y)$ just after the sample. We write this as

$$T(x, y) = S(x, y)U(x, y), \quad (14)$$

where S is a complex function $S = M(x, y)P(x, y)$. It alters both amplitude, by the real part M , and phase, by the complex part, P . M can be calculated from the Beer-Lambert law as before. P can be calculated by integrating

over the same paths, p . Without specifying the geometric conditions for any specific configuration, it has the form

$$P(x, y) = \frac{2\pi}{\lambda} \exp(i\phi(x, y)), \quad (15a)$$

where,

$$\phi(x, y) = \int_p (1 - n(x, y, z)) ds, \quad (15b)$$

and n is the refractive index of the sample.

At the detector

The next step is to decide how the wave changes as it leaves the object at the so-called contact plane, and travels to the detector through air. Ultimately we want to find the intensity that the detector perceives, it does not read the phase.

The principle by C. Huygens, stated in the 17th century, says that, given a wavefront, each point of the wavefront can be considered the source of a spherical wave as illustrated in Fig. 11. This principle was put into equations by A.-J. Fresnel and his formula was later slightly corrected when it was derived from Maxwell's equations by G. Kirchhoff [18].

The so-called *Fresnel propagator* can be derived from Kirchhoff's results. If we let the contact plane, located directly after the object, have $z = 0$, then the intensity at the detector at $z > 0$ is given by

$$I(x, y, z > 0) = |h_z * T|^2, \quad (16)$$

where

$$h_z(x, y) = \frac{\exp(ikz)}{i\lambda z} \exp\left(i\frac{\pi}{\lambda z}(x^2 + y^2)\right). \quad (17)$$

Inevitably, $z > 0$, so the detector will register an intensity that has changed in air, as described by the Fresnel propagator. To remove the phase contrast effects, is the same as recover $M(x, y)$ from I . We have simulated how the detected intensity would vary at different distances z using Eq. 16, shown in Fig. 12.

The last step before we have a suitable description that can be inverted is to simplify the expression given by the Fresnel propagator. Such formulas have been derived several times [23, 29] and the details will not be repeated here. The simplifications involve truncation of series expansions, and also

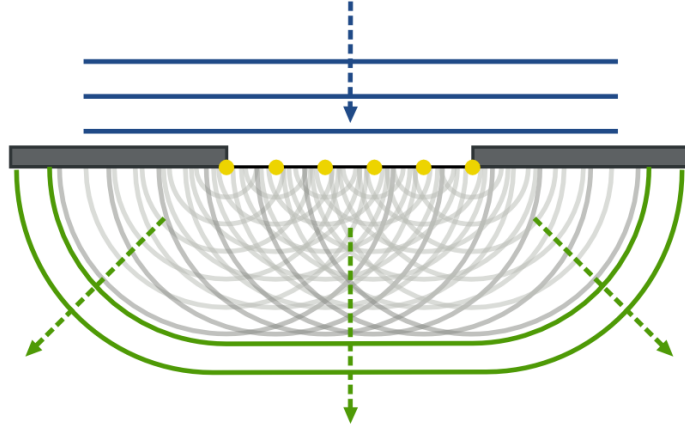


Figure 11: An illustration to Huygens' principle. A wave enters a slit from above. The propagation after passing the slit can be calculated from each point of the slit, which is considered to emit a spherical wave. [Illustration: A. Nordmann]

assume that $\phi(x, y)$ varies slowly. The resulting approximation for the image at the detector, I , at a distance z is

$$I(x, y, z > 0) \approx M(x, y) \left(1 - \frac{\lambda z}{2\pi} \nabla^2 \phi(x, y) \right). \quad (18)$$

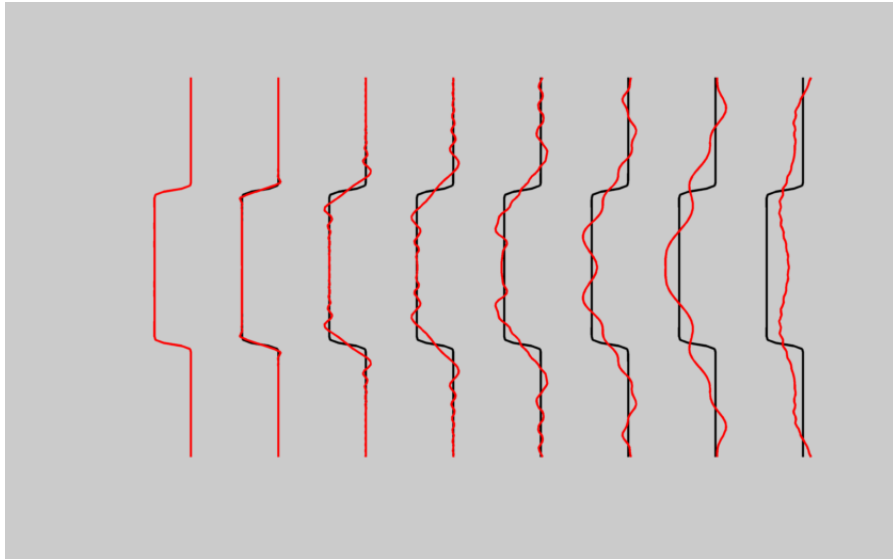
To retrieve the intensity at the contact plane where $z = 0$ is not directly achievable from here. Directly at the contact plane the irradiance is independent of the phase shift and is given by Beer-Lambert's law, hence $I(x, y, z = 0)$ is expected in conventional CT. If we add the assumption that the phase change is proportional to the absorption we get

$$I(x, y, z > 0) \approx M(x, y) \left(1 - z k \nabla^2 M(x, y) \right), \quad (19)$$

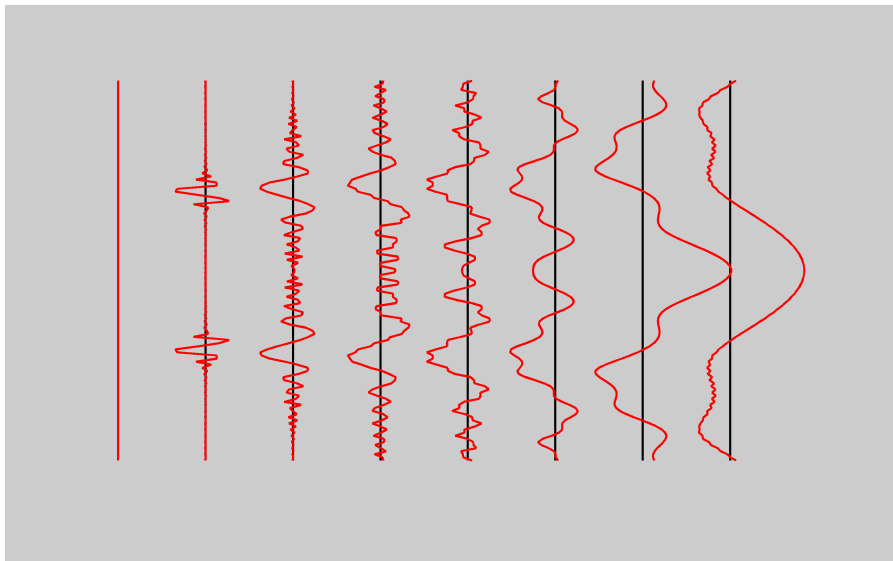
where k is some constant. This equation is invertible. The last assumption that we used is valid when the object consist of only one type of material. This holds for paper that contain only air and wood fibres and also approximately at the inside of composites that contain a plastic matrix and wood fibres.

4.3 Absorption retrieval

For single image CT, phase retrieval can be done by inverting Eq. 19, but there are other ways with different setups using images at different distances



(a)



(b)

Figure 12: The intensity shown as a beam passes objects at distances (from left to right): 0, 10, 50, 100, 200, 500, 1000, and 2000 mm. Black lines: absorption at the contact plane. Gray lines: a: amplitude and phase changes. b: only phase is delayed.

or using gratings, see Ref. [16].

FBP commutes with the Laplace operator and most of the diffraction fringes seen in micro-metre-resolution CT can be explained as an addition of second order derivatives to the projection images. Hence, it should be possible to remove the phase contribution or equivalently retrieve the absorption also in the CT images. These arguments were presented in Paper I where the main conclusions are:

- The processing is faster since the filtering does not have to be followed by an FBP.
- The processing can be done for any region of interest, which saves even more time and makes it possible to try many filter settings.
- The projection data does not have to be at hand, which saves storage.
- The quality is identical to state of the art methods, and can possibly be even better since no low pass filtering has to be done simultaneous to the absorption retrieval.

In [116] we have also explained how the parameters of this method can be determined from the geometry of the imaged objects, summarised in Appendix A. These results provide an objective and fast way to determine the absorption retrieval parameters.

4.4 Image quality and artefacts

CT images of wood fibre composites and paper materials, which are acquired at about $1\ \mu\text{m}$ resolution, can be affected by several classes of degradation. In Paper IV, we characterised and simulated the most typical ones that we had found in synchrotron CT. They include:

- *Blurring and smearing.* This can be caused by motion of (or inside) the sample. Motion can be caused by mechanical vibrations of the stage and shrinkage due to drying during the scan.
- *Reflection artefacts.* X-ray scattering or reflecting inclusions can cause star-like artefacts or shadows [95]. These are hard to get rid of with a direct reconstruction algorithm, since they are non-linear, but can sometimes be reduced by iterative methods.
- *Ring artefacts.* They appear as circles or half circles around the centre of rotation in the tomograms. The causes are most likely defective or

badly calibrated detector elements. There are methods to correct ring artefacts before or after tomographic reconstructions.

- *Fringes around edges.* These appear as dark and bright bands at edges that can not be explained by the X-ray absorption of the samples. They are caused by refraction and can be removed prior to reconstructions if the parameters of the tomograph are well known [23].

As shown Paper IV, most of these degradations can be modelled well. That means that even if these artefacts can not be prevented, we can study how automatic methods react to them.

5 Directional data

A direction at a pixel in an image is a fundamental measurement and only second to the actual pixel value in importance. Directions in digital images can be given multiple meanings, in principle it could be any mapping from the image to a vector field.

In this chapter, directions are calculated as gradients, but the representation methods work also for other definitions of directions. For scalar images, the direction is a property that can be given to single pixels, but several pixels are required to calculate it. Directions in N -dimensional images will be described by unit length vectors in \mathbb{R}^N , i.e., for two-dimensional images as points on the circle $S^1 : \{x, y; x^2 + y^2 = 1\}$ and for three-dimensional images as points on the sphere $S^2 : \{x, y, z; x^2 + y^2 + z^2 = 1\}$.

The smallest symmetric patch around a pixel in an image consist of the pixel itself and the facing neighbours. For two-dimensional images that gives five pixels, for three-dimensional images seven pixels, and so on. Such patches are large enough for a rough direction estimation, which can be obtained as the first order coefficients of a Taylor series expansion. Typically, larger patches are used to ensure rotational invariance, and that is a consequence of the interpolation function as discussed in Chapter 3.

The local distribution of directions around a pixel is a texture property and can be used to calculate higher order properties such as curvature. It can also be used for tasks such as tracking and orientation space constructions.

This chapter is the basis for the following one on curvature, and is also fundamental to Paper II and III. The techniques that will be presented are also used in Paper VI, IX and VIII. The first section describes how to get the local orientation at specific pixels in images, i.e., at the smallest scale. After that follows a section that presents techniques for averaging orientations and directions, i.e., that takes the discussion to larger regions. A closed form for the coefficients of a kernel density estimator is derived in the accompanying Appendix B; this is done both for directional data on the circle, S^1 and on the sphere S^2 . These series expansions allow for efficient computations.

5.1 Directions from images

Local gradients, rather than local pixel values, are used in many situations to analyse image content. One reason is the invariance to absolute intensity – gradients are invariant to constant additions to the image, that is $\nabla(I(\mathbf{x}) + c) = \nabla I(\mathbf{x})$, where c is a constant. Gradient *directions* are furthermore invariant to multiplications, i.e., $\angle \nabla(c_1 + c_2 I)(\mathbf{x}) = \angle \nabla I(\mathbf{x})$, where \angle denotes the angle to some arbitrary reference vector.

We have used Gaussian derivatives to calculate direction vectors $\mathbf{x}_j, j = 1 \dots J$, as motivated and introduced in Chapter 3. However, there are more alternatives alternative. Quadrature filters have excellent properties, being phase invariant and very compact [51, 52, 67, 68]. There is also the option to calculate derivatives using morphological operations [97].

5.2 Representing directions and orientation

When directions are available at each pixel, we would like to find suitable ways to summarise and visualise them for neighbourhoods, i.e., groups of pixels. This problem is independent of the method that was used to obtain the directions. The following properties are important:

1. *Rotational invariance.* To compare points from images that are rotated differently.
2. *Good localization of modes.* I.e., localisation of maxima and minima to distinguish fine rotations.
3. *Averaging.* An averaging method should be available, to reduce noise and act as an interpolation function when only a few points are used, e.g., for small neighbourhoods.
4. *Computational efficiency.* This is particularly important when the method is applied to all pixels in an image.

Directional data is usually represented by histograms, for example in the popular scale invariant feature transform (SIFT) by D. G. Lowe [78, 79]. Kernel density estimations (KDE) are not as common in the literature but are an attractive alternative, especially for S^2 , as we will see. The structure tensor is a symmetric representation, which can be seen as a special kind of KDE, as will be demonstrated.

Histograms

To use histograms is more or less the default option when representing directional data – probably since they are simple to understand and implement. In histograms, N -dimensional directions are put into distinct bins, b_1, b_2, \dots, b_B , each one corresponding to a part of S^{N-1} such that $\cup b_i = S^{N-1}$ and $b_i \cap b_j = \emptyset$, unless $i = j$.

If the range of the data is known, there is usually only one parameter to choose: The number of bins, B , or, equivalently, the width of the bins. In some situations, it can also be beneficial to have bins of varying width. In relation to the list of properties above, we can say that:

1. Histograms over S^1 are in general not rotationally invariant, only for angles that are integer multiples of $2\pi/B$. For S^2 the situation is even less satisfactory since the surface can not be regularly divided in more than five different ways, the Platonic solids [31]. There are also other ways to divide the surface of the sphere that might be useful for histogram constructions [17, 41].
2. Extreme values are only found with precision $\pm\pi/B$ on S^1 . However, interpolation can be used to increase this in some situations [79].
3. Any discrete low pass filter can be used for S^1 , and the quality depends on B .
4. The computational efficiency is best with small B . The properties above do, on the other hand, benefit from large B so there is always a compromise between these goals.

Kernel Density Estimators

The technique *kernel density estimation* (KDE) is common in statistics and was introduced in the 1960s by E. Parzen [91]. It is used to estimate an unknown, continuous distribution, based on samples from the distribution which are weighed by a certain kernel.

A KDE of some distribution, K , is a linear combination of the samples convolved with a weighting function w , according to:

$$K(x) = \sum_{j=1}^J w(x - x_j), \quad \mathbb{R} \rightarrow \mathbb{R}. \quad (20)$$

This estimate converges to the true distribution as the number of samples goes to infinity and the weighting function converges to the Dirac impulse function. The estimate is also a good approximation in the case of a finite number of samples, but then the weighting function needs a large support, i.e., region where it is non-zero.

For this thesis, KDEs are used for S^1 and S^2 . In Appendix B we find the coefficients c_k for the KDE K_1 on S^1 as

$$K_1(\theta) = \sum_{k=-\infty}^{\infty} c_k e^{ik\theta}, \quad S^1 \rightarrow \mathbb{R}, \quad (21)$$

and also the coefficients f_{lm} for the KDE K_2 on S^2 as

$$K_2(\theta, \phi) = \sum_{l=-\infty}^{\infty} \sum_{|m| \leq l} f_{lm} Y_{lm}(\theta, \phi), \quad S^2 \rightarrow \mathbb{R}, \quad (22)$$

where Y_{lm} are the spherical harmonics. Efficient computations can be achieved by truncating these series, which introduces smoothness. These representations have the following properties:

1. K_1 is rotationally invariant and can be rotated by simple formulas. When the coefficients are calculated for K_2 , it can be rotated around θ using simple formulas, but not around any other axis.
2. Modes can be located with numerical precision using steepest gradient descent or other optimisation methods.
3. Averaging can be understood through the diffusion equation [24]. The solution to the diffusion equation gives a one parameter formula, which can be used to continuously change the KDE to its average.
4. The complexity is $\mathcal{O}(MJ)$ for K_1 where M is the number of terms and J the number of samples. For K_2 , it is $\mathcal{O}(JM^2)$. To find the coefficients also involves evaluation of trigonometric functions, which is expensive if done naïvely [12].

The Structure Tensor

The structure tensor, Λ , sometimes called the second moment matrix [51, 74], is formed from J direction vectors, \mathbf{d}_j by

$$\Lambda = \sum_{j=1}^J \mathbf{d}_j \mathbf{d}_j^T. \quad (23)$$

The directions can also be weighted by scalars and the sum above may be formulated as an integral over a neighbourhood in a digital image.

Λ can be seen as a mapping from $S^N \subset \mathbb{R}^{N+1}$ to \mathbb{R} in two ways. We let $\mathbf{x} \in S^N$, $\theta = \angle \mathbf{x}$, then we define the following two functions (which give Λ multiple meanings):

$$\Lambda(\theta) = \Lambda(\mathbf{x}) = \mathbf{x} \Lambda \mathbf{x}^T. \quad (24)$$

Λ is symmetric and bimodal, the maxima being antipodal, which means that $\Lambda(\theta) = \Lambda(\theta + n\pi)$, $n \in \mathbb{Z}$ and that $\Lambda(\theta)$ has at most one distinct maxima in $(0, \pi]$. This makes Λ a coarse but robust orientation representation. Other than that, it shares the properties of K_1 except being very fast since only $(N+1)N/2$ coefficients are used. It might be interesting to know that the structure tensor concept has been generalised [96] to encode multiple antipodal modes.

Now we will show why Λ can be seen as a special KDE. We let \mathbf{d}_j be vectors of $S^1 \in \mathbb{R}^2$ and denote their angles, with respect to some reference

direction, \mathbf{e} , by θ_j . Now, let these directional data be represented by a *KDE* with weighting function, $w(x) = \cos^2(x)$, then

$$K_1(\theta) = \sum_{j=1}^J \cos^2(\theta - \theta_j). \quad (25)$$

We can represent these directions using the structure tensor as well, then

$$\Lambda(\mathbf{d}) = \mathbf{d} \left(\sum_{j=1}^J \mathbf{d}_j^T \mathbf{d}_j \right) \mathbf{d}^T \quad (26a)$$

$$= \sum_{j=1}^J \left(\mathbf{d} \mathbf{d}_j^T \mathbf{d}_j \mathbf{d}^T \right) \quad (26b)$$

$$= \sum_{j=1}^J \left(\mathbf{d} \mathbf{d}_j^T \right) \left(\mathbf{d}_j \mathbf{d}^T \right) \quad (26c)$$

$$= \sum_{j=1}^J \cos^2(\theta - \theta_j), \quad (26d)$$

which shows that the representations K_1 and Λ are equivalent.

6 Surfaces and curvatures

.. the ratios between straight and curved lines are not known,
and I believe cannot be discovered by human minds ...

–Descartes

Differential geometry is the application of calculus to geometry. It provides fundamental concepts for understanding and describing surfaces, such as mean and Gaussian curvature, geodesics and principal frames. The important classification of points on surfaces as convex, concave, flat or saddle points also gets a precise meaning in terms of curvature by differential geometry. The field is relatively new, coordinates have only been used since they were introduced in the seventeenth century by Descartes, and the development of differential geometry could start only after the introduction of calculus by Newton. The basic tools of differential geometry were developed in the eighteenth and nineteenth century by C. F. Gauss, J. B. Meusnier, G. Monge and others.

A surface can often be described in many ways; it can be given by explicit formulas and implicit formulas and it may be sampled at a finite number of points. It can also be translated, rotated and scaled, which produce, yet again, more possible descriptions of intrinsically the same object. In this chapter we will see curvature properties that depend only on the shape of objects and not on how they are represented. First, we will see how these concepts applies to surfaces given by explicit formulas, and then for sampled surfaces such as those found in CT images.

Curvature appeared in the digital image processing community in 1983 in a publication by R. Machuca and K. Philips, where curvature is calculated for edges in 2-D gray scale images [82]. Nowadays curvature is used for a wide range of applications, including level set propagation, visualization, recognition and segmentation. Curvature properties are used not only for digital images but also for meshes, the standard representation of digital objects in computer graphics.

The standard method for curvature calculation of surfaces in 3-D volumetric images [66, 89, 107], is based on first and second order differentials and is to a large extent a direct application of the formulas for parametric surfaces. It is likely to be the best choice in most situations, at least when objects are sampled according to the Nyquist rate, when they are not too thin, and when individual objects are well separated from each other in the images.

Our work in this area, which is found in Paper II and III, is motivated by

volumetric images of fibre networks, in which the situation is far from optimal for the standard method. Fibre walls are thin, the material is densely packed, and we are not interested in curvature of the smallest details, so either the digital objects or the curvatures have to be averaged. Our method can be seen as an extension of the work by B. Rieger et al. [93] and is somewhat related to the work by Y.-L. Yang [127] on meshes. In contrast to the standard method, it has the following properties:

- No second order derivatives are used to find the principal curvature directions; instead an integral formula is used. We will show that this gives less disturbances due to noise.
- The structure tensor, not the gradient, is averaged, and therefore the gradient is allowed to vanish completely at points of interest. This means that curvature can be calculated for ridges, and not only for edges.
- Averaging can be done in different ways. It shares Gaussian low pass filtering of the image with the standard method, but there is the option to increase the integration region as well as to choose other methods to average the orientation representation, including non linear filters.

The first two sections of this chapter summarises some of the classical theory of curvature and is based on the book by E. Kreyzig [71]. Section 6.1 and 6.2 present the standard method for curvature calculation in volumetric images and the last sections are devoted to our method.

6.1 Differential geometry of curves

To understand surface shape, we first need to understand how shape of curves can be described in terms of curvature and torsion. Let \mathbf{c} be a curve in three-dimensional space, parameterised by t such that

$$\mathbf{c} : t \rightarrow (x, y, z), \quad (27)$$

and, further, we let $l(t)$ be the arc length of the curve such that

$$l(t) = \int_0^t \left\| \frac{d\mathbf{c}(t)}{dt} \right\| dt. \quad (28)$$

When the line is parameterised by l , we say that the curve is *parameterised by arc length* or that it has a natural parameterisation. The derivative, \mathbf{t} , of

the curve with respect to the arc length,

$$\mathbf{t}(l) = \frac{d\mathbf{c}}{dl} = \dot{\mathbf{c}}, \quad (29)$$

is the unit length tangent vector at l . We have use arc length parameterisations of the contours of fibre cross sections in Paper V and of fibre centre lines in Paper VI. From now on, derivatives with respect to l will be denoted with a dot as in Eq. 29. The tangent vector defines a one-dimensional tangent space at each location, l , by

$$\mathbf{y}(u) = \mathbf{c}(l) + u\mathbf{t}(l). \quad (30)$$

The next object that is natural to introduce is the osculating (kissing) plane, which contains both the tangent and the derivative of the tangent. The osculating plane can be described as the plane in which the curve lives. At a point of interest, $\mathbf{c}(l)$, it is formally defined as the \mathbf{z} that satisfies the determinant equation

$$|(\mathbf{z} - \mathbf{c}(l)) \dot{\mathbf{c}}(l) \ddot{\mathbf{c}}(l)| = 0. \quad (31)$$

Curvature

The unit principal normal, \mathbf{p} , is directed along the derivative of the normal

$$\mathbf{p}(l) = \frac{\dot{\mathbf{t}}(l)}{\|\dot{\mathbf{t}}(l)\|} = \frac{\ddot{\mathbf{c}}(l)}{\|\ddot{\mathbf{c}}(l)\|} \quad (32)$$

The *curvature*, κ , of \mathbf{c} at any location l is defined as the rate of change of the tangent such that

$$|\kappa(l)| = \|\dot{\mathbf{t}}\|, \quad \text{or,} \quad |\kappa(l)| = \langle \dot{\mathbf{t}}, \mathbf{p} \rangle. \quad (33)$$

Note that no sign is used in this definition of curvature since it is arbitrary at the moment.

The reciprocal of the curvature, ρ , is given by

$$\rho(l) = \frac{1}{\kappa(l)}. \quad (34)$$

Is called the *radius of curvature* since a circle of radius r has curvature $|\kappa| = 1/r$ everywhere.

Curvature of curves is used in Paper V to locate and close openings in fibre walls. A discrete curvature estimator, with applications to wood fibres, can be found in [30].

Torsion

In a similar way as the change in the tangent vector along a curve gave rise to the curvature, the change of the *binormal*, \mathbf{b} ,

$$\mathbf{b}(l) = \mathbf{t}(l) \times \mathbf{p}(l), \quad (35)$$

gives rise to the *torsion*, τ , sometimes called the second curvature. It is defined by the following relation

$$\dot{\mathbf{b}}(l) = -\tau \mathbf{p}(l) \quad (36)$$

so,

$$\tau(l) = -\langle \mathbf{p}(l), \dot{\mathbf{b}}(l) \rangle. \quad (37)$$

Torsion can be interpreted as rotation of the osculating plane and hence a planar curve has zero torsion. A curve can be determined, up to position and orientation, if κ and τ are known by solving the Frenet-Serret formulas. That means that knowing curvature and torsion, there is not very much more to know about a curve. That implies that a curve can be described without any reference to a specific coordinate system.

6.2 Differential geometry of surfaces

To derive expressions for curvatures of surfaces, we will use the definitions that were introduced for curves. Let us begin with a surface, explicitly parameterised by

$$\mathbf{x}(u, v) = (x_1(u, v), x_2(u, v), x_3(u, v)) \quad (38)$$

and assume that the first derivatives

$$\mathbf{x}_u = \frac{\partial \mathbf{x}}{\partial u}, \quad \mathbf{x}_v = \frac{\partial \mathbf{x}}{\partial v}, \quad (39)$$

span a two-dimensional subspace, i.e., $\langle \mathbf{x}_u, \mathbf{x}_v \rangle \neq 0$. Then the tangent plane at $\mathbf{x}(u, v)$ can be described as

$$\mathbf{y}(p, q) = \mathbf{x} + p\mathbf{x}_u + q\mathbf{x}_v, \quad (40)$$

compare to Eq. 30. If there is an implicit representation of the surface available, $G(x_1, x_2, x_3) = 0$, then the surface normal can be expressed as

$$\left(\frac{\partial G}{\partial x_1}, \frac{\partial G}{\partial x_2}, \frac{\partial G}{\partial x_3} \right). \quad (41)$$

The first fundamental form

If we start with a surface like in Eq. 38, any curve in such surface can be described by

$$u = u(s), \quad v = v(s). \quad (42)$$

The tangent to the curve on the surface, is readily found using the chain rule

$$\dot{\mathbf{x}} = \frac{d\mathbf{x}}{ds} = \frac{\partial \mathbf{x}}{\partial u} \frac{du}{ds} + \frac{\partial \mathbf{x}}{\partial v} \frac{dv}{ds}, \quad (43)$$

which means that the *element of arc*, ds^2 , is

$$ds^2 = \langle \mathbf{x}_u du + \mathbf{x}_v dv, \mathbf{x}_u du + \mathbf{x}_v dv \rangle, \quad (44)$$

or

$$ds^2 = \langle \mathbf{x}_u, \mathbf{x}_u \rangle (du)^2 + 2\langle \mathbf{x}_u, \mathbf{x}_v \rangle du dv + \langle \mathbf{x}_v, \mathbf{x}_v \rangle (dv)^2. \quad (45)$$

When we introduce the notation

$$g_{\alpha\beta} = \langle \mathbf{x}_\alpha, \mathbf{x}_\beta \rangle, \quad \alpha, \beta \in \{u, v\}, \quad (46)$$

the *element of arc* is

$$ds^2 = g_{uu}(du)^2 + 2g_{uv} du dv + g_{vv}(dv)^2. \quad (47)$$

In vector notation it is

$$ds^2 = (du \quad dv) \begin{pmatrix} g_{uu} & g_{uv} \\ g_{vu} & g_{vv} \end{pmatrix} \begin{pmatrix} du \\ dv \end{pmatrix}. \quad (48)$$

The coefficients $g_{\alpha\beta}$ are the components of a tensor, which is called the *first fundamental form*. We denote by G the matrix that contains the $g_{\alpha\beta}$ in the equation above.

The second fundamental form

Once again, the starting point is a curve on a surface. At any point, the surface and the curve can be related by

$$\cos \gamma = \langle \mathbf{p}, \mathbf{n} \rangle, \quad (49)$$

where \mathbf{n} is the surface normal and \mathbf{p} is the unit principal vector to the curve, i.e.,

$$\mathbf{p}(l) = \ddot{\mathbf{x}}(l)/\kappa, \quad (50)$$

so

$$\kappa \cos \gamma = \langle \ddot{\mathbf{x}}, \mathbf{n} \rangle. \quad (51)$$

We introduce the coefficients of the *second fundamental form*, $b_{\alpha\beta}$ as

$$b_{\alpha\beta} = \langle \mathbf{x}_{\alpha\beta}, \mathbf{n} \rangle, \quad \alpha, \beta \in \{u, v\}, \quad (52)$$

and collect the coefficients in a matrix, B . By expand and simplify (see Ref. [71] for a detailed derivation) the second order derivative, $\ddot{\mathbf{x}}$, of \mathbf{x} with respect to the arc length and using the facts that $\langle \mathbf{x}_u, \mathbf{n} \rangle = 0$, and $\langle \mathbf{x}_v, \mathbf{n} \rangle = 0$ we can arrive at a much more useful representation of Eq. 51 as the quotient of the first and second fundamental forms:

$$\kappa \cos \gamma = \frac{u^T B u}{u^T G u}. \quad (53)$$

The *normal curvature*, κ_n is the curvature of the plane curve that live in the plane spanned by \mathbf{n} and the tangent of the curve itself. For those curves, $\gamma = 0$ and

$$\kappa_n(l) = \frac{u^T B u}{u^T G u}, \quad (54)$$

i.e., the curvature at $\mathbf{c}(l)$ when $\mathbf{t}(l) = (du, dv)$.

Principal curvatures

The *principal curvature directions*, \mathbf{d}_1 and \mathbf{d}_2 , are the eigenvectors to Eq. 54 and the corresponding eigenvalues $\kappa_1 > \kappa_2$ are the *principal curvatures*, sometimes defined $|\kappa_1| > |\kappa_2|$.

Since $|u| = 1$ and $\det G \neq 0$

$$\kappa_n (u^T G u) = u^T B u, \quad (55)$$

which converts into

$$\kappa_n u = B G^{-1} u. \quad (56)$$

Now, this appears as the promised eigenvalue problem, where the eigenvalues are the solutions κ_n to

$$\det(BG^{-1} - \kappa_n I) = 0. \quad (57)$$

The matrix BG^{-1} is sometimes called the Weingarten curvature matrix and the eigenvalues κ_1 and κ_2 form the *Gaussian curvature*, $G = \kappa_1 \kappa_2$ and the *mean curvature* $H = (\kappa_1 + \kappa_2)/2$.

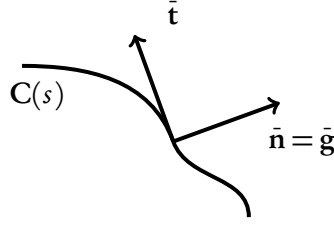


Figure 13: A curve, C along an isocontour of an image, where $I = k$.

First forms of a polynomial surface

To give a practical example of the calculations involved to get the coefficients of the first two fundamental forms, we do so for a polynomial surface. We start with the surface

$$\mathbf{x}(u, v) = (u, v, a + bu + cv + duv + eu^2 + fv^2), \quad (58)$$

At the point $(0, 0)$ the first order derivatives are

$$\mathbf{x}_u = (1, 0, b), \quad \mathbf{x}_v = (0, 1, c), \quad (59)$$

since only derivatives of second order terms remain. The second order derivatives are

$$\mathbf{x}_{uu} = (0, 0, 2e), \quad \mathbf{x}_{uv} = \mathbf{x}_{21} = (0, 0, d), \quad \mathbf{x}_{vv} = (0, 0, 2f), \quad (60)$$

and in this case, only terms of order two remain. That gives the following coefficients, using Eqs. 46 and 52:

$$g_{11} = 1 + b^2, \quad g_{12} = bc, \quad g_{22} = 1 + c^2 \quad (61)$$

$$\mathbf{n} = \frac{(-b, -c, 1)}{\sqrt{1 + b^2 + c^2}} \quad (62)$$

$$b_{11} = \frac{2e}{b^2 + c^2 + 1}, \quad b_{12} = \frac{d}{b^2 + c^2 + 1}, \quad b_{22} = \frac{2f}{b^2 + c^2 + 1}. \quad (63)$$

6.3 Curvature in digital images from differentials

We will now present the standard method for curvature calculations, as can be found in the work by Monga et al. [88] and Thirion and Gourdon [107].

We start with a Taylor expansion of the image I at the point \mathbf{x}

$$I(\mathbf{x} + \delta) = I(\mathbf{x}) + J(\mathbf{x})\delta + \delta^T H(\mathbf{x})\delta + \mathcal{O}(\delta^3), \quad (64)$$

where J is the Jacobian matrix and H is the Hessian matrix, which contain derivatives of order one and two, respectively. Then, we assume that there is a two-dimensional curve $\mathbf{c}(s) = (x(s), y(s))$, and that it is parameterised by arc length. We let it follow an iso-level of a function so that it can be expressed as $\mathbf{c} = \{(x, y) | I(x, y) = k\}$, where k is a constant (this situation is illustrated in Fig. 13).

At the point \mathbf{p} , on \mathbf{c} , we have

$$\frac{d\mathbf{c}}{ds} = \mathbf{t}, \quad \text{and}, \quad \frac{d\mathbf{t}}{ds} = \mathbf{n}, \quad (65)$$

and assuming that the gradient is non-zero,

$$\mathbf{g} = \left(\frac{\partial I}{\partial x}, \frac{\partial I}{\partial y} \right). \quad (66)$$

The gradient and the derivative of the tangent have the same direction but are not necessarily of the same magnitude, i.e.,

$$\frac{\mathbf{g}}{\|\mathbf{g}\|} = \frac{\mathbf{n}}{\|\mathbf{n}\|}. \quad (67)$$

From Eq. 33 we know that curvature can be expressed as

$$\kappa = -\left\langle \frac{d\mathbf{g}}{ds}, \bar{\mathbf{t}} \right\rangle / \|\mathbf{g}\|. \quad (68)$$

By applying the chain rule, , Eq. 68 is simplified to

$$\kappa = -\frac{\bar{\mathbf{t}} H \bar{\mathbf{t}}^T}{\|\mathbf{g}\|}. \quad (69)$$

To generalise this result for 3-D curves, we have to consider that there are infinitely many lines through each point in the tangent plane, i.e., the space orthogonal to the image gradient. The curvature expression corresponding to Eq. 69 becomes

$$\kappa(\theta) = -\frac{\bar{\mathbf{t}}(\theta) H \bar{\mathbf{t}}^T(\theta)}{\|\mathbf{g}\|}. \quad (70)$$

The subspace spanned by the gradient does not contain the principal directions so we can restrict the search to the tangent space. If we deflate H with the gradient direction we get,

$$G = (\mathbf{1} - \bar{\mathbf{g}}^T \bar{\mathbf{g}}) H (\mathbf{1} - \bar{\mathbf{g}}^T \bar{\mathbf{g}}), \quad (71)$$

and then

$$\kappa_1 + \kappa_2 = \text{Tr } G, \quad \text{and,} \quad \sqrt{\kappa_1^2 + \kappa_2^2} = \text{Fr } G, \quad (72)$$

so the principal curvatures can be found as

$$\kappa_{1,2} = \frac{\text{Tr } G \pm \sqrt{2(\text{Fr } G)^2 - (\text{Tr } G)^2}}{2}. \quad (73)$$

6.4 Curvature from orientation fields

We have just seen the derivation of the standard method for calculation of curvatures in digital images, which is based on differentials of first and second order.

Parallel to this is a group of methods that use an orientation representation to calculate and average the normal direction. The first method that can be attributed to this group is by Bårman et al., in 1989 [9].

Their approach is based on quadrature filters [51], which are used to get the local orientation from the image. Then the so-called *double angle technique* is used for representation and averaging of the local orientation. The curvature estimator is finally described in the Fourier domain. The approach is for curves in 2-D images and was later extended to 3-D images, where the double angle representation is functionally replaced by the structure tensor [10, 11]. These first methods do not arrive at any closed form for the curvatures, only expressions that *relate* to the curvatures. In 2004, Rieger et al. were able to continue this work, and found explicit formulas for the curvatures [93].

Our contributions, extending that of Rieger et al. are several. The most important are:

- The bias is considerably lowered for high curvature points.
- The relation between the principal curvature directions and the structure tensor is elucidated.
- The signs of the curvatures are included.
- Alternatives to low pass filtering for averaging the tensor components are proposed and show to be useful.

Details of our approach can be found in Paper II and III, but we will give an extended discussion on the relation between the principal curvature directions and the eigenvalues to the structure tensor here. For completeness, we also show how the principal curvatures are calculated.

Principal curvature directions

The principal curvature directions are the directions with extremal curvature. It has been proposed that they can be found as the eigenvectors to the structure tensor [93], and also as eigenvectors to a similar matrix [127] in addition to being the eigenvectors to the Weingarten curvature matrix. In this section, we will study this assumption and try to pinpoint how strong this relation is.

We start with the surface of Eq. 58 and discard the higher order terms, which do not affect the curvature calculations. Let's call it

$$L''(u, v) = w = a + bu + cv + duv + eu^2 + fv^2. \quad (74)$$

It should be obvious that this surface can be translated so that the constant a disappears. Then the resulting surface can be rotated, for example by two Euler rotations so that the normal is parallel to the w -axis, removing b and c .

Lemma: Given a second order surface patch of the form

$$z = L'(x, y) = c_0x^2 + 2c_1xy + c_2y^2 \quad (75)$$

there is a rotation around the z -axis such that

$$L(u, v) = w = Au^2 + Bv^2, \quad A \geq B. \quad (76)$$

Proof: Write L' in matrix form,

$$L' = \mathbf{x}C\mathbf{x}^T = (x, y) \begin{pmatrix} c_0 & c_1 \\ c_1 & c_2 \end{pmatrix} \begin{pmatrix} x \\ y \end{pmatrix}. \quad (77)$$

The coefficient matrix C , is normal, i.e., $C^T C = C C^T$. That means that it can be diagonalised by

$$C = R^T D R, \quad (78)$$

where R is a rotation matrix and D is a diagonal matrix, which contains the eigenvalues to M , according to the spectral theorem [99]. To ensure that $A \geq B$, the upper left element of D should be chosen as the largest eigenvalue. \square

Lemma: The principal curvature directions of L are $(1, 0, 0)$ and $(0, 1, 0)$ in the (u, v, w) coordinate system. To get the corresponding directions in the (x, y, z) coordinate system, we simply need to rotate around the z -axis by R .

Proof: Since $g_{11} = g_{22} = 1$, $g_{12} = b_{12} = 0$, $b_{11} = e$ and $b_{22} = f$, the Weingarten curvature matrix is diagonal and the principal curvature directions coincide with the coordinate axes. \square

To establish a relationship between the parametric surface patch and the volumetric objects that are found in digital images, we need to specify what we mean by a "surface" in the digital images.

We say that I is a realisation of L when

$$I(u, v, w) = \begin{cases} 0, & L(u, v) > 0, \\ 1, & L(u, v) \leq 0. \end{cases} \quad (79)$$

From that follows that ∇I is proportional to $L_u \times L_v$ when $(u, v, w) \in \{(u, v, L(u, v))\}$ and 0 otherwise.

Lemma: The eigenvectors of

$$\int_{B_\epsilon} (\nabla I)^T (\nabla I) dx dy dz, \quad (80)$$

where the region of integration B_ϵ is an infinite cylinder around the w -axis of radius, ϵ , are

$$\begin{pmatrix} 1 \\ 0 \\ 0 \end{pmatrix}, \begin{pmatrix} 0 \\ 1 \\ 0 \end{pmatrix} \text{ and } \begin{pmatrix} 0 \\ 0 \\ 1 \end{pmatrix}, \quad (81)$$

in the (u, v, w) coordinate system, i.e., the same as the principal curvature directions for L .

Proof: With a change to polar coordinates using $r = \sqrt{u^2 + v^2}$, $u = r \cos \theta$, $v = r \sin \theta$, and the notation, $N = \nabla I$, $T := N^T N$, $\|N(r, \theta)\| = \|N(r, \theta + \pi)\|$ and Eq. 80 can be expressed as

$$\begin{aligned} (*) &= \int_0^\epsilon \int_0^{2\pi} T(r, \theta) \|N\| r d\theta dr \\ &= \int_0^\epsilon \int_0^\pi \underbrace{[T(r, \theta) + T(r, \theta + \pi)]}_{2\Gamma} \|N(r, \theta)\| r d\theta dr, \end{aligned} \quad (82)$$

Using $N(u, v) = (-2Au, -2Bv, 1)$ or $N(r, \theta) = (-2Ar \cos \theta, -2Br \sin \theta, 1)$, we get

$$\Gamma = \begin{pmatrix} \mathbf{M} & 0 \\ 0 & 1 \end{pmatrix}, \quad (83)$$

where

$$\mathbf{M} = (2r)^2 \begin{pmatrix} A^2 \cos^2 \theta & AB \cos \theta \sin \theta \\ AB \cos \theta \sin \theta & B^2 \sin^2 \theta \end{pmatrix}. \quad (84)$$

Eq. 82 essentially contains up to four non-zero integrals when integration is carried out with respect to θ :

$$\alpha = 4A^2 r^3 \int_0^\pi \cos^2 \theta \|N\| d\theta, \quad (85)$$

and

$$0 = 4AB r^3 \int_0^\pi \cos \theta \sin \theta \|N\| d\theta, \quad (86)$$

since the integrand is anti-symmetric around $\theta = \pi/2$. The last integrals are

$$\beta = 4B^2 r^3 \int_0^\pi \sin^2 \theta \|N\| d\theta, \quad (87)$$

and

$$\gamma = 2r \int_0^\pi \|N\| d\theta. \quad (88)$$

All together, this gives a concise expression for Eq. 82:

$$(*) = \int_0^\epsilon \begin{pmatrix} r^2 \alpha & 0 & 0 \\ 0 & r^2 \beta & 0 \\ 0 & 0 & \gamma \end{pmatrix} r dr, \quad (89)$$

where $\alpha > \beta$ as long as $|A| > |B|$ and $\alpha < \gamma > \beta$ as long as the surface is relatively flat. \square

Eq. 89 shows that the eigenvectors corresponding to the two smallest eigenvalues point out the principal curvature directions. But when the integration region is large, it might happen that the directions get mixed up.

The relationship above is only approximate for digital images due to these reasons:

- We can seldom use small enough surfaces patches (filters) to only include variations of second order from the digitized surfaces.
- The images are always band limited and do not have the sharp discontinuity of I defined in Eq. 79.
- The proof uses a cylindrical integration region, whereas it only makes sense to use filters with spherical integration region for any situation that I can think of.

Since we have not established a theoretical relation that corresponds completely to the way in which we integrate the structure tensor – using Gaussian filters – we are obliged to test the relationship numerically.

We set up an experiment by realising second order polynomial patches as volumetric images of $17 \times 17 \times 17$ voxels. The patches have the form

$$z = \alpha x^2 + \beta y^2, \quad (90)$$

so that we always know the correct principal curvature directions. Visualisations of a few such surfaces can be seen in Fig. 14. The parameters α and β were varied between -2 and $.2$ at discrete steps as seen in Fig. 15. All σ s were set to 1 and the experiments were run five times to present the average. Note that the case when $|\alpha| = |\beta|$ was not considered since the principal curvature directions have no preferential direction for that case.

My conclusions from this experiment are that the structure tensor indeed points out the principal curvature directions, and that it is more accurate in the presence of noise than the Hessian for finding the principal curvature directions.

Principal curvatures

Rieger et. al calculate the principal curvature values by the following procedure. First they calculate the structure tensor, M , from the volumetric image,

$$M = S * G_\sigma(\mathbf{x}), \quad (91)$$

where G_σ is a Gaussian kernel with a standard deviation of σ pixels. If we denote the eigenvectors of M , largest first, by $\mathbf{v}_1, \mathbf{v}_2, \mathbf{v}_3$ then the absolute values of the principal curvature values κ_1 and κ_2 are found by

$$|\kappa_{1,2}| = \frac{1}{\sqrt{2}} \|\nabla_{\mathbf{v}_{2,3}} M(\mathbf{v}_1)\|_F, \quad (92)$$

where $\|\cdot\|_F$ denotes Frobenius norm and $\nabla_{\mathbf{v}} M$ denotes the directional derivative of M .

To calculate principal curvature values from Eq. 92 will introduce even more low pass filtering since Gaussian derivatives are used. This is confirmed by the relatively high bias of the method.

In Paper III we instead propose that the curvature values should be found by calculating the derivative of the tensor field using interpolation at an offset from the position of interest. We also introduce a correction term, which cancel out the negative effects of a non-vanishing distance between the interpolation points.

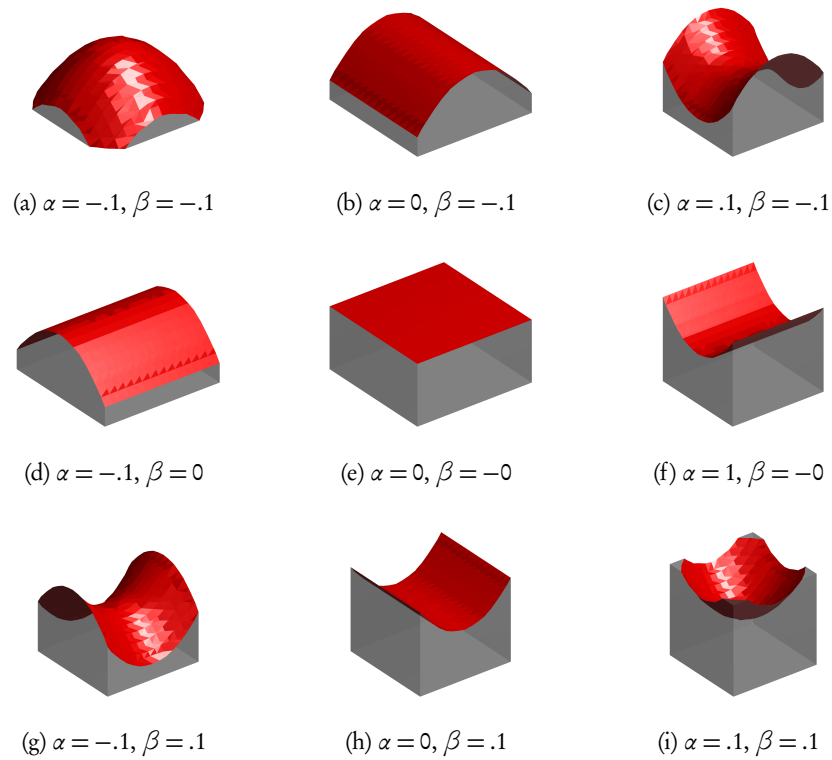


Figure 14: Second order polynomial surfaces defines the top of solid objects; implemented using erf clipping [111] on the vertical distance from the analytic surface location. Visualization by marching cubes on the volumetric data. In Fig. (a)–(i), the shape of the polynomial surfaces are visualised for a few parameter values.

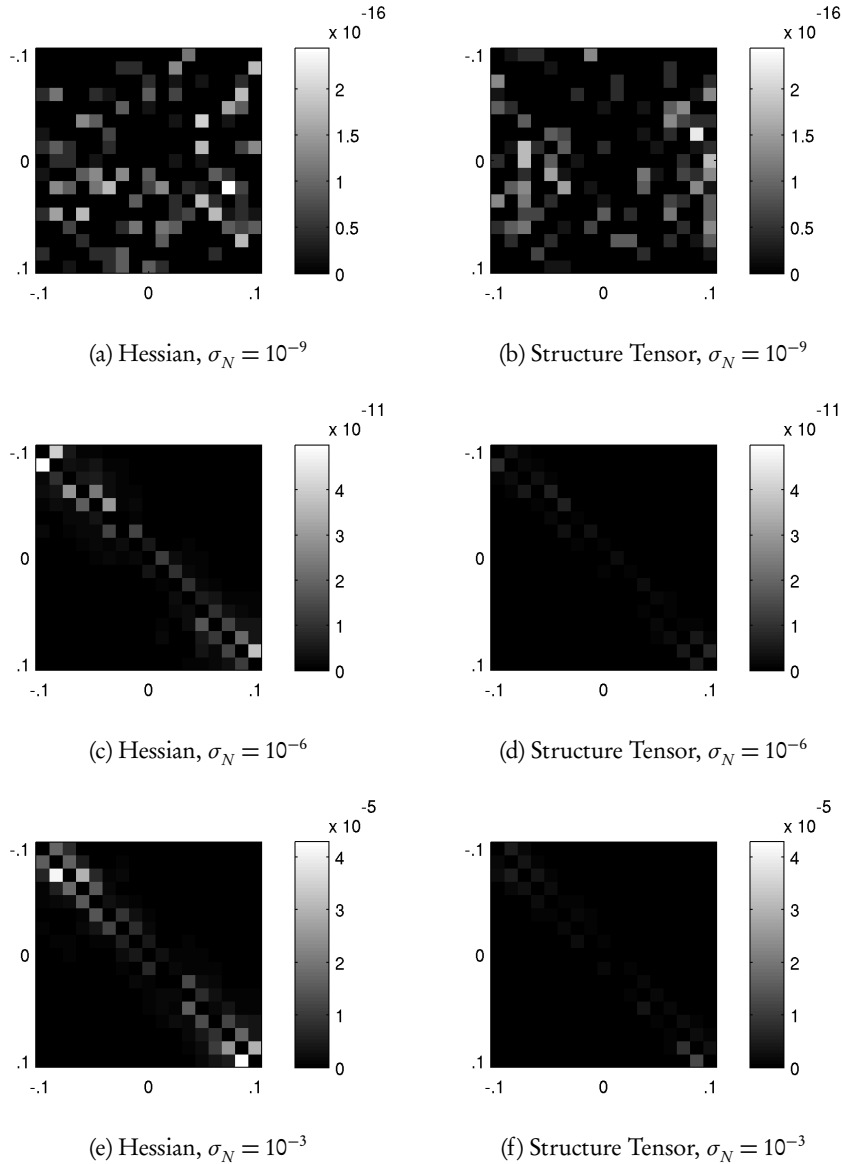


Figure 15: Error in the first principal curvature direction estimation defined as $1 - |\langle \mathbf{t}, \mathbf{p} \rangle|$, where \mathbf{t} is the true direction and \mathbf{p} is the estimated direction, are shown in Fig. (a)–(f). Axes in the figures show the parameters of the quadratic surface, i.e., a and b in Eq. 90. To get an idea of how these surfaces look, I’ve plotted a few in Fig. 14. The noise that is added is Gaussian, with standard deviation σ_N .

6.5 Curvature signature of shapes

We conclude this chapter with a few examples of how sampled digital surfaces in volumetric images can be classified by their curvature.

At our disposal we have the principal curvature, the Gaussian and the mean curvature. There are also derived properties; for example J. J. Koenderink and A. J. van Doorn [70] propose that κ_1 and κ_2 are separated into a shape and a size component. The *shape index*, s , is given by

$$s = \frac{2}{\pi} \arctan \frac{\kappa_2 + \kappa_1}{\kappa_2 - \kappa_1}, \quad \kappa_1 \geq \kappa_2, \quad (93)$$

and the *curvedness*, c that encodes scale

$$c = \left(\frac{\kappa_1^2 + \kappa_2^2}{2} \right)^{1/2}. \quad (94)$$

Rescaling an object changes c while s is invariant. Both measurements are of course invariant to rotations and translations as already mentioned in the beginning of this chapter.

See Fig. 16 for examples of curvature pairs from sample points at surfaces plotted. It should be seen that basic shapes are really distinguishable from their set of curvature values.

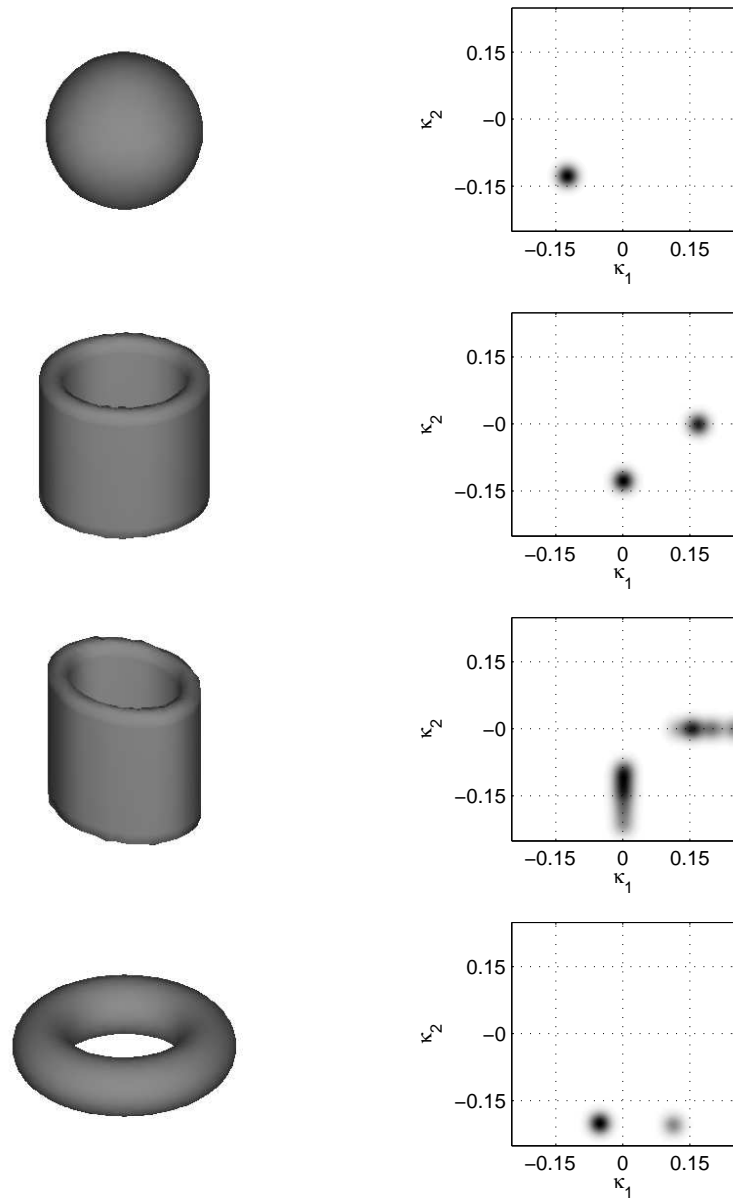


Figure 16: Shapes can be recognised by their curvature signature, i.e., set of principal curvatures. Volumetric objects are rendered by the marching cubes algorithm, they are, a: a sphere, c: a cylinder, e: a cylinder with oval cross section, g: a torus. Their respective curvature signatures are rendered in (b), (d), (f) and (h).

7 Maximal flow algorithms

Optimisation methods that find maximal flows have an essential role in image analysis and processing. There is an assortment of applications including stereo matching [19], image reconstruction [19] and minimal surface construction [2]. By re-stating problems into maximal flows these methods can now solve problems that were previously solved by *iterated conditional modes* and *simulated annealing*, and often much more efficiently.

To find the maximal flow through a domain between a source node, s , and a sink node, t , is equivalent to finding the smallest cut in the domain that separates the source and sink nodes according to the *max-flow min-cut* theorem. The solution is called the *s-t minimal cut*.

The first published solution to s-t minimal cut problem is known as the Ford-Fulkerson algorithm [45], which today is used in modified forms since it is known not to converge in some situations [129]. A small modification brings the Edmonds-Karp algorithm, which is based on repetitive calculations of shortest paths [39]. These paths are found by Dijkstra's algorithm [36] or, to be more precise, by the solution to problem number two in Dijkstra's paper: "*Find the path of minimum total length between two given nodes P and Q*".

Maximal flow algorithms emerged in image analysis in 1989 when D. M. Grieg et al. [53] showed that a certain image restoration problem, posed three years earlier [13], could be solved exactly by an s-t cut. In 1988 there were at least fourteen different published algorithms that solved such problems [48]. These methods were made popular in image analysis in the beginning of the 21st century when Y. Boykov and V. Kolmogorov published a new, often faster method, based on the Goldberg-Tarjan algorithm, with several application examples [19–21].

With this chapter I hope to share some insights about these methods. It begins with a review of the Edmonds-Karp algorithm since it is probably the easiest one to understand. Then, continuous graph cuts whose solutions are less hampered by discretization artefacts, are reviewed. The chapter is closed with a few implementation details and examples relevant to separation of fibres in paper sheets and composites, which is performed in Paper V and VI.

7.1 Maximal flow in graphs

Images can be converted to a graph and back again without loss of information. Usually each pixel in an image is represented by a vertex v_i and neighbouring pixel pairs (v_i, v_j) are connected by an edge, e_{ij} , with a certain pos-

itive cost or capacity, c_{ij} . In total that makes up the graph, $\mathcal{G} = \{V, E, C\}$, where $V = \{v_j\}$, $E = \{e_{jk}\}$, $C = \{c_{ij}\}$ and $e_{jk} \in E$ when v_j and v_k are connected with a capacity $c_{ij} > 0$.

A certain minimization problem will have a certain graph construction. There are several options how to connect the vertices and the capacities are assigned differently depending on the problem. The terms capacity and flow are of course physical *analogues*, the equations are similar for those of idealised liquid flow when there is neither viscosity nor compressibility. The flow in the graph will be defined over the set of edges, for each edge, e_{jk} , we allow a flow, f_{jk} . We say that a flow is valid when the net flow is zero at each node and is constrained by the capacity at each edge, in other words

$$\sum_j f_{ij} = 0, \quad \forall i, \quad (95a)$$

$$f_{ij} \leq c_{ij}. \quad (95b)$$

s-t cuts and maximal flow

We add two special vertices to V , one source node, s , and one sink node, t together with suitable edges, which connects them to the nodes already in V . Then, we can define an s-t cut, which is a partition of V such that $s \in S$, $t \in T$, $V = S \cup T$, and $\emptyset = S \cap T$. To each such cut we associate a cost, C , which is given by:

$$C(S, T) = \sum_{v_i \in S, v_j \in T} c_{ij}. \quad (96)$$

A *minimal* s-t cut has a minimal cost among all possible s-t cuts on a graph. Such solutions do not readily match any of the sampling models discussed in Chapter 3 and do not give any further indication of what happens between the pixels. A remedy could be to re-sample the image more densely prior to the graph construction, but there are also other alternatives [83].

Edmonds-Karp algorithm

The heuristics behind the Edmonds-Karp algorithm, which finds maximal flows, are rather simple. As long as there is a path from s to t with remaining capacity: find it, calculate its maximal capacity determined by the minimal remaining edge capacity along the path, and subtract it from the graph. This procedure is then repeated for the remaining graph also known as the *residual graph*.

One edge will be saturated at each iteration using these steps. The maximal flow is found when there is no more paths from s to t . Then the graph

is disjoint and split into the sets S and T . According to the max-flow min-cut theorem, the min-cut is found at the same time. Starting from s and t respectively, those two sets can be found by region growing. The minimal cut is found as the set of edges with one node in S and the other in T . See Algorithm 1 for the details.

Algorithm 1 The Edmonds-Karp algorithm for maximum flow from s to t .

Require: $\mathcal{G}(V, E, C), s, t \in V$
 $f = 0$, total flow
 $F = \{f_{ij}\}, f_{ij} = 0$, flow for each edge
while \exists shortest path, π , from s to t in $\mathcal{G}(V, E, C)$ **do**
 $m(\pi) = \min c_{ij}, \forall (i, j) \in \pi$, maximum flow of the path
 $f_{ij} = f_{ij} + m, \forall (i, j) \in \pi$, save the found flow
 $c_{ij} = c_{ij} - m, \forall (i, j) \in \pi$, residual capacity
 $f = f + m$,
end while
return f, F

The shortest paths are found by some variety of Dijkstra's algorithm, which can be found in any textbook on basic algorithms, e.g., [115]. The worst case complexity, using a naive implementation, is $\mathcal{O}(|V|^2)$. Useful implementations use priority queues and have a complexity of $\mathcal{O}(|E| + |V|\log(|V|))$. See [80] for a recent comparison of priority queues that can be used for implementations.

We can expect that a graph-cut solution has a complexity bound by $\mathcal{O}(|E|^2 + |E||V|\log(|V|))$ since at least one edge is eliminated at each iteration. That is a good indication of the complexity, although there are certain algorithms designed to have peak performance for graphs with specific characteristics [48].

7.2 Maximal flow in continuous domains

Continuous graph cuts are the counterpart to graph cuts in the continuous domain. Properties of such systems and their solutions were first investigated by G. Strang [103]. The domain is given a scalar metric, g , and the flow F is defined everywhere. The following equations describe a valid flow in this setting:

$$\nabla \cdot \mathbf{F} = 0, \tag{97a}$$

$$\|\mathbf{F}\| \leq g. \tag{97b}$$

For us, the most important difference between Eq. 97 and 95 is that the L^2 -norm is used in the continuous formulation. That means that the equation is isotropic and invariant to rotations, in contrast to Eq. 95.

The flow from source to sink, F_{st} , is in this case calculated by a surface integral around the source according to

$$F_{st} = \oint_{\partial S} \mathbf{F} \cdot \mathbf{N}_S dS \leq \oint_{\partial S} g dS, \quad (98)$$

where \mathbf{N} is the outward normal to S and \mathbf{F} is the flow defined by a vector field. The minimal cut is also the minimal surface that separates the source and sink.

The problem has been discretized, or rather adapted for digital images, by B. Appleton and H. Talbot [2]. Their paper contains an algorithm that finds maximal flows. The algorithm uses a scalar field P over the domain, and evolve the following equations:

$$\frac{\partial P}{\partial t} = -\nabla \cdot \mathbf{F}, \quad (99a)$$

$$\frac{\partial \mathbf{F}}{\partial t} = -\nabla P, \quad (99b)$$

$$\|\mathbf{F}\| \leq g. \quad (99c)$$

Details can be found in their paper, along with a proof that the maximal flow is found at convergence. In Fig. 17 the pressure, P , is visualised before convergence for a problem designed so that reflections at the boundaries can be seen.

I've implemented their method and it is used in Paper VI. Some observations that I've made include:

- Exact convergence can usually not be achieved and the iterations have to be cancelled before that, to maintain acceptable running times. The method has especially slow convergence for problems where there are several possible cuts with almost the same area, i.e., local minima close to the global. This means that usually only an approximation of the minimal surface is found.
- Even though the algorithm is run for a long time, there usually remains a slight discrepancy between the flow from the source node and the area of the cut.

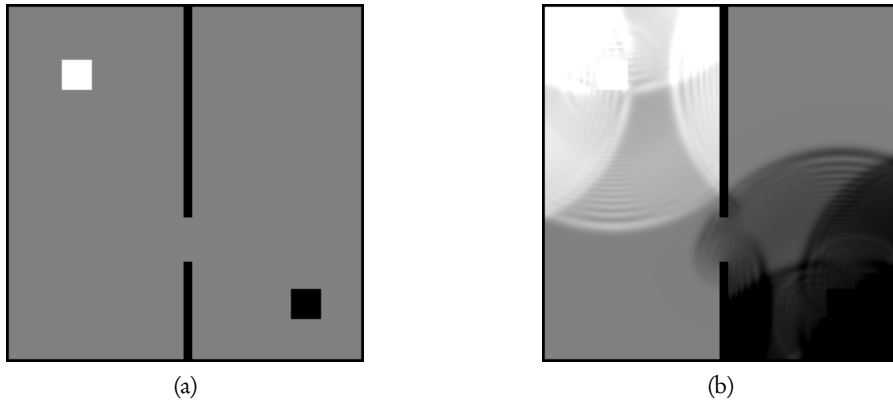


Figure 17: Pressure evolves according to Eq. 99 in a planar problem with hard constraints, see [2]. This is not how such systems usually is initialised but the example reveals the wave nature of the system. a: white square: hard constraint, $P = 1$, black square: hard constraint, $P = 0$. Gray area: initial pressure, $P = .5$ and $g = 1$. b: After a 1000 iterations with time steps of .1.

- There are more recent studies, for example by J. Yuan et al. [128], and possible better solution methods available now.
- The continuous problem is much harder to solve since it is non-linear. Does the improved metric quality of the minimal cut really motivate the extra computational cost? Yes, it should in most cases and the example in Fig. 18 should be motivation enough. It can be seen in the figure how the discrete graph cut solution prefers, or finds, straight edges that are not in the original image.

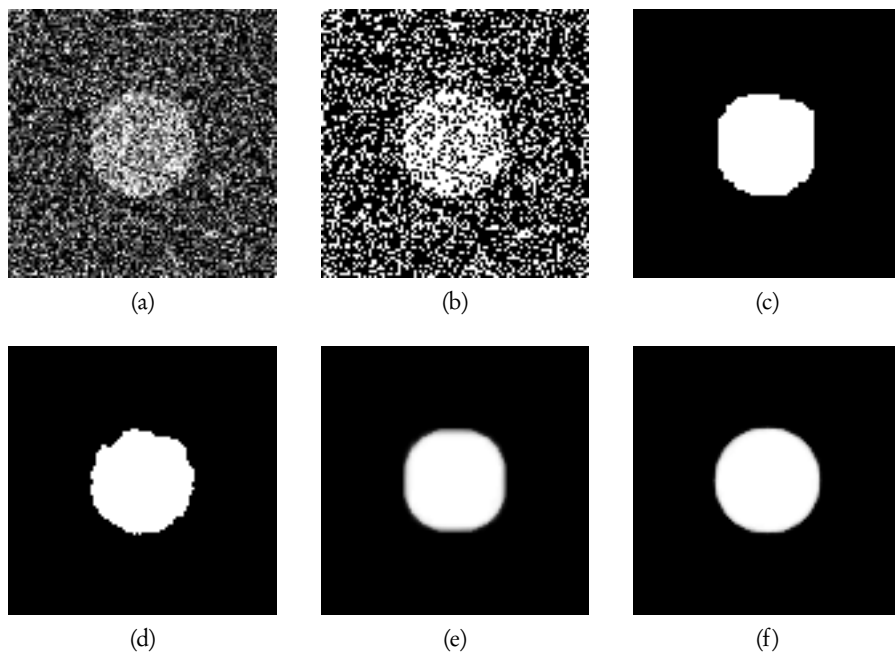


Figure 18: A characteristic difference between the continuous and discrete graph cuts can be seen here. a: Input image, I , with a round disk where, $I = 1$, on a background where $I = 0$, immersed in Gaussian additive noise. b: Thresholded at 0.5. c: Discrete cut, note the straight edges. d: Continuous cut. e: average of 100 discrete cuts. f: average of 100 continuous cuts.

8 Summary of the papers

Paper I	<i>Postprocessing method for reducing phase effects in reconstructed microcomputed-tomography data</i> Journal of the Optical Society of America A (JOSA A), 2013
Summary	The standard methods for phase contrast removal are applied prior to reconstruction. They are compared to a new one that works on already reconstructed data.
Conclusions	Our method is evaluated to have a performance almost identical to previous methods. At the same time, it is considerably faster and more versatile. No projection images are needed, it can process also small regions of interest and it is not limited to low pass filtering for noise suppression.
Contributions	Wernersson: Developed the method, implemented the filter and wrote the paper. Boone: Provided data sets, run the other methods, contributed to writing. Van den Bulcke and Van Hoorebeke and Luengo Hendriks: contributed to writing and discussions.
Paper II	<i>Accurate Estimation of Gaussian and Mean Curvature in Volumetric Images,</i> 3D Imaging Modeling Processing Visualization Transmission (3DIMPVT), Hangzhou, China, 2011
Summary	A new way to calculate curvature of surfaces in volumetric images is proposed.
Conclusions	The method is more accurate where curvature is high compared to the most similar alternative [93]. The way that the sign of the curvature is calculated is beneficial for separating inside from outside, of wood-fibre-like structures.
Contributions	Wernersson: Idea, implementation and writing. Luengo Hendriks and Brun: Suggestions for evaluation and detailed comments on the manuscript.

Paper III	<i>Robust and Unbiased Curvature of Isophote Surfaces in Volumetric Images,</i> Manuscript
Summary	The work in Paper II is improved by introduction of a correction factor. Non-Gaussian methods are used to filter the tensor components of the orientation field, including anisotropic diffusion and a novel bilateral filter.
Conclusions	The correction factor does decrease the curvature bias. The non-Gaussian filters are superior in regions where surfaces are close to each other.
Contributions	Wernersson: Idea, implementation and writing. Luengo Hendriks & Brun: Suggestions for evaluation and detailed comments on the manuscript.
Paper IV	<i>Generating synthetic μCT images of wood fibre materials,</i> 6th International Symposium on Image and Signal Processing and Analysis (ISISPA), Salzburg, Austria, 2009
Summary	It is hard to evaluate segmentation methods for wood fibres in CT volumes due to the lack of ground truth. In the paper, we simulate a range of wood-fibre morphologies. We also simulate noise present in the CT imaging setup and are able to reproduce characteristic noise and artifacts in CT images.
Conclusions	It is feasible to simulate wood fibres captured by CT machines. Even though the packing of synthetic fibres can be improved, this provides a useful tool for future evaluations.
Contributions	Wernersson: Idea for the paper. CT machine characterisation and simulation. Wrote the manuscript. Luengo Hendriks: Valuable comments on the manuscript. Brun: Wood fibre shape simulations and wood-fibre packing.

Paper V	<i>Segmentation of Wood Fibres in 3D CT Images Using Graph Cuts,</i> International Conference on Image Analysis and Processing (ICIAP), Vietri sul Mare, Italy, 2009
Summary	Pores and cracks in fibre walls have been troublesome for previous segmentation methods. Here we suggest a method to identify these features and to close them. Individual wood fibres are then segmented by first identifying the lumen and then separated with a graph cut based method.
Conclusions	The curvature of fibre cross sections seems to be a good feature for detection of defects with the purpose of a topographical closing of fibre cross sections. Graph cuts can be used to refine the quality of the segmentation compared to a previous approach given that some weighting is introduced on the edges.
Contributions	Wernersson: Idea, writing and implementation. Brun & Luengo Hendriks: Detailed comments on the manuscript and suggestions on the implementations of the algorithms.

Paper VI	<i>Characterisations of fibre networks in paper using computed tomography images,</i> Nordic Pulp & Paper research Journal (NPPRJ), 2014
Summary	Instead of trying to automatically segment single wood fibres in volumes, a semi-manual approach is suggested where each fibre is marked by a few control points, which are interpolated to a line. Automatic methods can then be used with that line as input.
Conclusions	The suggested methodology is a good balance between low manual input and high quality output in terms of measurements. The measurements of contact area seems especially successful. Other methods require more manual labour and are limited to flat contact areas. The manual input of this method is about one minute per fibre.
Contributions	Wernersson: Development of fibre characterisation software and measurement methods. Writing most of the paper. Borodulina: Wrote most of the introduction section. Did manually mark the fibres on which the method was tested. Prepared the samples. Kulachenko & Borgefors: Detailed comments on the manuscript.

Paper VII	<i>Effects of defects on the tensile strength of short-fibre composite materials,</i> Mechanics of Materials, 2014
Summary	Dog bone samples of plastic-wood-fibre composites were scanned with a μ CT machine to detect defects due to imperfections in mixing. The same samples were later on tested for Young's modulus.
Conclusions	The largest defect is likely to cause the breakage. The strength at the interface between matrix and defects is negligible.
Contributions	Joffre: Wrote the paper. Mechanical testing and theory. Miettinen: Scanning of samples and ellipsoidal fitting. Wernersson: Correction for beam hardening artifacts in the images. Implementation of a MRF-based segmentation method to detect the defects. Manual verification of the segmentation results. Isaksson: Mechanical theory. Gamstedt: Planning and writing
Paper VIII	<i>Light scattering in fibrous media with different degrees of in-plane fiber alignment,</i> Optics Express, 2014
Summary	The direction of scatter from incoming light into paper can be modelled based on Maxwell's equations. Theoretical predictions are compared to measurements of laser scatter patterns as well as orientations measured from CT images.
Conclusions	A high correlation between the orientation measurements based on laser and CT images was shown.
Contributions	Linder: Wrote the paper. Performed the light diffusions measurements and simulations. Löfqvist: Writing and planning. Wernersson: Suggested resolution for the CT images. Estimated orientation in the CT images and wrote the corresponding section. Gren: Design of the experimental setup for the light diffusion measurements.

Paper IX	<i>3D tree-ring analysis using helical X-ray tomography</i> , Dendrochronologia, 2014
Summary	Densiometric profiling and ring width measurements are usually done with flat bed scanners. In this paper, the possibility to use high resolution helical CT imaging is investigated.
Conclusions	High resolution CT seems to be well suited for dendrochronological investigations. Advantages over the classical methodology are that the bias due to the drilling- or cutting angles can be eliminated, and the sample preparation simplified. The publicly released software shows that very little manual work needs to be added after the scanning.
Contributions	<p>Van den Bulcke: Wrote and planned the paper, implemented the manual method, performed and analysed the scans.</p> <p>Wernersson: Wrote the mathematical parts of the paper. Implemented and suggested the image based measurement methods.</p> <p>Dierick: comments and suggestions on the manuscript, suggestions on density calculations</p> <p>Van Loo: comments and suggestions on the manuscript, suggestions on scan procedure and scan time.</p> <p>Brabant: comments and suggestions on the manuscript, suggestions on the usage of Morpho+ for calculations of vessel-free density.</p> <p>Haneca: comments and suggestions on the manuscript, specifically focusing on dendrochronology.</p> <p>Boone, Van Hoorebeke, Masschaele, Brun, Luengo Hendriks, Van Acker: comments and suggestions on the manuscript.</p>

9 Conclusions and future work

You observe that in the life of the intellect there is also a law of inertia.

–Felix Klein

The theme of this thesis is characterisation of wood-fibre-based materials. There are many problems associated with this, which need specific approaches and tools. I have worked throughout the whole process, from pre-processing of CT images to representations of fibre directions for whole images by just a few coefficients.

The range of wood-fibre shapes is wide. These shape variations are interesting in themselves, but unfortunately, make general approaches hard to pursue. X-ray computed tomography at micrometre resolution has turned out to be a good tool for characterisation of wood fibres and wood-fibre organisation in materials. However, CT is not the universal answer to all measurements. It is natural to assume that all fibres could be segmented automatically but that is impossible due to fundamental reasons. This is because the boundaries between individual fibres look the same both when they are bonded and when they are only pressed against each since there is no difference in X-ray absorption.

There is, however, numerous properties that can be measured from CT images of wood-fibre based methods. These properties include fibre length distributions, fibre orientation, fibre bonds, fibre dimensions as well as properties that can be derived from these. The quality of the extracted parameters depends on the quality of the image acquisition and the status of the fibres and fibre network.

As the quality of CT images increases and images become cheaper to acquire, it is my hope and belief that automated methods can play a role in online measurements, besides being a valuable tool in scientific studies. An effort to collect the best methods into a unified software framework could accelerate this goal. There is also a need for reference data sets in the community. Without such images it is simply not possible to assess the quality of a new method compared to previous approaches.

This chapter continues with a summary of the contributions from this thesis and the included papers. After that follows suggestions for future work.

9.1 Summary of contributions

I believe that the main contributions of this thesis are these:

- *New ways to characterise paper samples.* The contributions are mainly due to Paper VI, in which a complete software tool is presented. It is based on the assumption that manual interactions are necessary (until fully automated methods are developed), but should be minimal. We have proposed a very fast manual fibre-selection methodology; only a few seconds per fibre are needed by the operator because only one curve that approximately follows each fibre is used and can be defined by a handful of points. Based on that line, many measurements can be performed automatically.

These characterisation algorithms can be used to create reference volumes needed in the development of fully automated methods. The software is published as open source, to initiate more collaboration in the field.

- *A new method for fibre-fibre bond analysis.* Among the included measurement algorithms in the software tool mentioned above is an algorithm that analyses fibre-fibre bonds. It can be seen as an extension of the work in Paper V. A fibre-fibre bond region is defined as the surface with minimal area between two marked fibres. This allows for more complex bond regions than the previously most accurate method [87], while it requires less manual effort. It is also fully three-dimensional, in contrast to a previous approach [84].

The increased precision and the viability of this method makes bond analysis much more available than previously.

- *Tools for simulation of CT images of wood-fibre-based materials.* In Paper IV, tools were developed both for the simulation of wood-fibre-shapes and for simulation of realistic noise. The noise model is based on measurements of images from the TOMCAT beamline at the Swiss Light Source (SLS).

This work makes it possible to generate noise that is characteristic for micrometre resolution images of wood-fibre-based materials. With this tool it is possible to study how this noise affects algorithms designed for wood-fibre-based materials. The modelling of wood-fibres can also be used to create realistic synthetic images of composites and paper sheets.

- *Absorption retrieval in CT images.* For the first time, in Paper I, we have demonstrated that phase contrast can be removed from CT images to retrieve absorption from mixed mode images. Previous methods are applied prior to the tomographic reconstruction, which in

many ways is a more complicated procedure. With our method, the correction can be applied to small regions. There is no need for large projection data sets and the imaging parameters do not need to be known. The idea behind this solution appeared while working on simulations of the noise in μ CT images in Paper IV. Since the publication of Paper I, we also derived formulas, which are found in Appendix A, for how the two parameters can be calculated. The parameters can be calculated from the shape of imaged edges, which is more precise than the heuristic method that we used at first.

The impact of this study could be that phase contrast artefacts will be removed routinely. This is especially important when working with cross sections, since the phase contrast artefacts due to objects outside the cross sections can cause strange patterns.

- *A new method for calculation of curvature in volumetric images.* This work was presented in Paper II. It can be seen as an extension of the work by B. Rieger in [93], in which the sign of the principal curvatures is also included. The bias of our approach is lower, and the method is further improved in Paper III. Furthermore, a bilateral filter was introduced that makes the calculations less sensitive to surfaces nearby.

We hope that this method will be appreciated and used for analysis of volumetric images, especially in the analysis of wood-fibre based materials, where our experiments in Paper II indicate that this is a good tool for lumen segmentation.

- *We have shown that helical CT is an ideal tool for dendrochronology.* Methods for high precision measurements of annual ring density in wood from helical μ CT images were presented in Paper IX. This work shows the potential of this relatively new scanning method. The image analysis in the study is based on directional estimators, something that was learned during the work on Paper II.

We hope that this approach will increase the precision of wood-ring-based dating and that it can decrease the costs, since the sample preparation is simplified.

- *Tailored image analysis solutions.* In Paper VIII, fibre orientations are measured and compared with simulations and light scattering patterns to relate these techniques. In Paper VII, clusters of fibres, agglomerates or defects are segmented and measured.

The main importance of these contributions are that they introduce computerised image analysis to fields where it is not so commonly used.

9.2 Future work

During my work with this thesis I continuously found interesting things that could have been investigated further. Unfortunately, a lot of them were lost in the moment of inspiration. Nevertheless, here is a list of topics that I think are worthwhile to investigate:

- As previously mentioned, reference data sets would be highly useful for further developments within this research field.
- Further automatisations of the fibre-characterisation tools presented in Paper VI should be pursued. Verification based on reference images should be an integral part of that work.
- Most methods developed for fibre segmentation rely on *heuristic* methods. I think it is time to take a more formal approach, and investigate how the fibre segmentation problems can be stated as minimisation problems. It is natural to start with the question: What constitutes a good segmentation? As discussed before, there is an ambiguity involved in this problem statement since it is not possible to exactly locate boundaries between fibres in CT images. With a well-defined goal, it is a matter of finding suitable optimization tools, to get the segmentation. I have touched upon this approach slightly and tried, among other things, the image foresting transform [42] using different metrics formulated on orientation fields, but so far I have not found any fruitful formulation. It should be natural to include curvature in one way or another into such formulas, and that was the main motivation for the work in Paper II and III.
- The fibre–fibre bond analysis method should be studied in more detail. To do so, fibres could be imaged individually and then lightly pressed together and imaged again. That would yield morphologies for the fibres both individually and pairwise, which could be used to evaluate our fibre–fibre bond analysis method, as well as the other published methods.

Sammanfattning (Summary in Swedish)

Datoriserad bildanalys är att låta datorer analysera digitala bilder och räkna fram olika egenskaper från dem. Användningen av datoriserad bildanalys har fullständigt exploderat de senaste årtiondena och man finner nu avancerade automatiska matematiska metoder, i allt från mobiltelefoner och kompaktkameror till medicinsk utrustning.

Att låta datorer analysera bilder är praktiskt i många sammanhang – inte minst när man har stora mängder bilddata, eller när det finns krav på objektivitet och reproducerbarhet. Den bärande frågan är dock, hur konstruerar man dessa automatiska metoder?

Syftet med denna avhandling är att ta fram automatiska bildanalysmetoder för att karaktärisera enstaka träfiber och fiberstruktur i papper och kompositmaterial. Träfibrer är de avlånga cellerna i trädens stammar. Deras mekaniska egenskaper och dess längd- till bredd-förhållande på upp till 100 till 1 gör att de passar till många olika ändamål. Framförallt används de till att tillverka papper men även till att förstärka plaster i så kallade plast-träfiberkompositer. Papper tillverkas i många olika kvalitéer, allt från toalettpapper till högglassigt fotopapper. Skillnaden mellan dessa produkter kan till stor del beskrivas genom egenskaper hos träfibrerna och dess fiberstruktur i pappret. Dessa beror i sin tur på vilken råvara som har använts och hur den har processerats.

Bildmaterialet som används är datortomografiska bilder (CT), eller snitt, som beräknats fram från multipla röntgenprojektioner. I de flesta fall har bildserier används som tillsammans bildar volymetriska bilder, tredimensionella bilder av en volym. Upplösningen i bilderna är omkring en mikrometer, vilket är tillräckligt högt för att formvariationer hos enskilda fibrer ska kunna ses, inklusive dess längsgående hålrum, kallat lumen. Samtidigt är upplösningen sådan att tillräckligt stora områden kan avbildas för att ge kunskap även om fiberstrukturen hos material.

Arbetet sträcker sig över ett stort område. Det innehåller metoder för att simulera det brus eller de störningar som är vanligt förekommande hos bildtagningsutrustningen. Med hjälp av simuleringarna går det att uppskatta hur stora fel dessa störningar skapar i mätningarna. Faskontrast är ett viktigt fenomen som gör att man kan avbilda material som är helt eller delvis transparenta för ljus genom att utnyttja diffraktion. Högupplösta röntgenbilder av papper och kompositer innehåller som regel både absorptions- och faskontrast. En del av arbetet har bestått i att reducera faskontrasten i bilderna för att kunna få fram absorptionen. Detta är viktigt dels för att kunna använda bildanalysmetoder som är designade utifrån modeller som inte tar hänsyn till fastkontrast, dels när man ska analysera enskilda snitt, eftersom

utbredningen av faskontrasteffekterna kan påverka flera närliggande snitt. Det faskontrastreducerande filter som presenteras baseras på avfaltung av volymetriska tomogram.

Avhandlingen innehåller också metoder för att karaktärisera tvärsnitt av fibrer och fördelningen av fiberorienteringar i material. Dessa kan användas för att analysera tillverkningsprocesser och för att förfina mekaniska modeller av papper. En viktig komponent i detta är en metod för att mäta kontaktytorna mellan enskilda fibrer. Problemet är egentligen inte exakt lösbart eftersom kontaktytan inte har någon distinkt röntgenabsorption, men genom att definiera kontaktområdet med hjälp av en yta med minimal area mellan fibrerna så erhålls en mycket hög precision.

Kurvaturer hos ytor är rotations- och translationsinvarianta egenskaper. I avhandlingen presenteras en grupp av metoder som är mycket lämpliga att använda på fiberbaserade material. De här metoderna störs mycket litet av det faktum att fibrer ligger nära varandra, till skillnad från standardmetoderna för att beräkna kurvatur i volymbilder. Detta är viktigt framförallt när man vill filtrera bort små variationer hos ytor som inte är viktiga. Träfibrer har oundvikligen mycket variationer i ytan, som de får i de olika processstegen: från stam till papper. CT-bilder har dessutom en del brus som ger ytor ytterligare geometriska störningar. Det visas också att kurvaturegenskaper är mycket användbara för att finna lumen som i sin tur kan användas för att segmentera individuella fibrer.

En metod för att ta fram densitetsprofiler från borrhärnor av trä har också utvecklats. Den baseras på tredimensionella bilder tagna med spiral-CT i kontrast till tvådimensionella bilder som är den nuvarande standarden. Avhandlingen innehåller också arbete kring att detektera fiberkluster i bilder av kompositmaterial samt en jämförelse mellan olika metoder för att jämföra fiberorientering i pappersark.

Den här avhandlingen visar att datoriserad bildanalys redan är ett användbart verktyg för att karaktärisera enskilda fibrer och fibernätverk i papper och kompositmaterial. En stor utmaning kvarstår i att ta fram material för att verifiera nuvarande och framtida metoder och några förslag för hur det kan göras diskuteras i avhandlingen.

Acknowledgements

To all current and former colleges, thank you! – you made me enjoy the years at the Centre for Image Analysis. I would like to express my special gratitude to a few persons, who directly or indirectly contributed to this thesis.

- Gunilla Borgefors for believing in me and undertaking the task of turning me into a researcher.
- Cris L. Luengo Hendriks for your endless curiosity, all good advice, and the ever open door.
- Anders Brun for all deep insights that you shared with me.
- Jan Van den Bulcke, Matthieu Boone, Tomas Linder, Thomas Joffre, Arttu Miettinen, Ulf Hammarkvist, Shuo Li and Svetlana Borodulina for all the fun I had working with you.
- Everyone at SP Trä – you almost made me forget that I should finish my thesis.
- Staffan Jacobsson Svärd, Sophie Grape and Erik Branger for the interesting cooperation.
- Alexander Petutschnigg, Karl Entacher, Johann Charwat-Pessler, Ger- not Standfest, Gianluca Tondi and Thomas Wimmer for taking care of me in Kuchl. Also Arttu Miettinen and Tuomas Turpinen for the company in Jyväskylä.
- Lena Nordström who kept me away from any administrative bur- dens.
- Olle Eriksson for the long uptime(s).
- Gunilla Borgefors, Cris L. Luengo Hendriks, Anders Brun, Filip Malm- berg, Gunnar Sparr, Lisa Henningsson and Matthieu Boone for valu- able comments on the manuscript(s).
- Lisa and Hedvig for all your love and for enduring my absent mind at busy times.
- You. I hope that you found this thesis useful and I'd be grateful if you report any mistake that you find to me at erikw@cb.uu.se.

This research was partially funded through WoodWisdom-Net under project number 352006A and has been supported by the European Commission under the 6th Framework Programme: Strengthening the European Research Area, Research Infrastructures. Contract no: RII3-CT-2004-506008. It was also supported by Stiftelsen Gunnar Sundblads Forskningsfond. This research was given beam time at the TOMCAT beam line at the Paul Scherrer Institut, Villigen, Switzerland under proposal 20081028. The Xradia MicroXCT-200 instrument at Innventia, Stockholm, was supported by the Nils and Dorthi Troëdsson foundation's research fund.

Appendices

A Parameters in the phase contrast filter

The filter for absorption retrieval, which we introduced in Paper I, has two parameters, σ and ϵ , which relate the amplitude and width of the fringes in CT images to the mix of absorption and phase contrast. In Paper I it is proposed that these parameters are determined by a heuristic method. It is however easier to find the parameters directly from the shape of step edges in images, and this also allows for automated parameter selection. The content of this appendix can also be found in our conference contribution in Ref. [116] with the main difference that this presentation is more concise.

A.1 Derivation

If we apply the phase contrast model of Paper I to a three-dimensional step edge we get a function $R_{\sigma,\epsilon}$, i.e.,

$$R_{\sigma,\epsilon}(\mathbf{x}) = \theta(x_1) + \epsilon \Delta G(\mathbf{x})_{\sigma} * \theta(x_1), \quad \epsilon < 0, \quad (100)$$

where θ is a Heaviside step function, G_{σ} is a three-dimensional isotropic normal distribution with standard deviation σ , see Eq. 5. We will now derive two functions in a forward manner: amplitude, $A(\sigma, \epsilon)$, and width, $W(\sigma, \epsilon)$, according to Fig. 19. These functions can then be inverted to get σ and ϵ .

The amplitude can be expressed as the maximum of the integral

$$A(\sigma, \epsilon) = \max R_{\sigma,\epsilon}(\mathbf{x}) - 1 = \max R_{\sigma,\epsilon}(x_1, x_2 = 0, x_3 = 0) - 1 \quad (101)$$

$$= \max \epsilon \int_0^w \int_{-\infty}^{\infty} \int_{-\infty}^{\infty} \Delta G(x_1, x_2, x_3) dx_2 dx_3 dx_1, \quad w > 0, \quad (102)$$

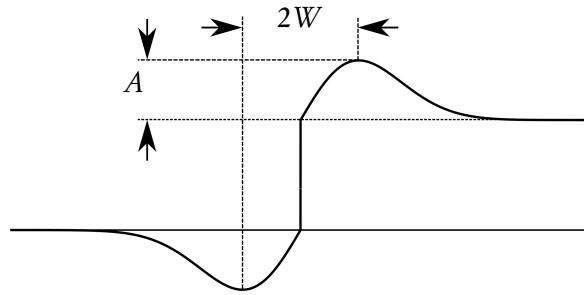


Figure 19: Eq. 100 plotted along r to illustrate the variables, $A = 1 - \max R$ and W , half the distance between $\min R$ and $\max R$. Compare with experimental data in Fig. 20

which is the maximum of the convolution $\epsilon \Delta G * \theta(x_1)$. Similarly, the width of the fringes is

$$W(\sigma, \epsilon) = \arg \max_{x_1} R_{\sigma, \epsilon}(x_1, x_2 = 0, x_3 = 0). \quad (103)$$

First we find the x_1 value that maximises R by integrating x_2 and x_3 over \mathbb{R}^2 , then integrating x_1 from 0 to w . Then we find the location of the maximum, W , of the obtained expression by derivation. A is then found by insertion and we arrive at:

$$A(\sigma, \epsilon) = \frac{\epsilon}{\sigma^2 \exp(1/2) \sqrt{2\pi}}, \quad (104a)$$

$$W(\sigma, \epsilon) = \sigma, \quad (104b)$$

and in the other direction,

$$\sigma(W, A) = W, \quad (105a)$$

$$\epsilon(W, A) = AW^2 \sqrt{2\pi} \exp(1/2). \quad (105b)$$

Note that a step edge of height 1 was used and that scaling will be required for most CT images.

A.2 Experiments

In Fig. 20 we have used this method to determine the filter parameters. A step edge was located and the signal orthogonal to the edge was interpolated. Then the signal was slightly averaged in the directions of the tangent plane to the edge. A and W were then identified according to their definition in Fig. 19. The filter parameters were calculated by Eq. 105 and the absorption retrieved by the method of Paper I.

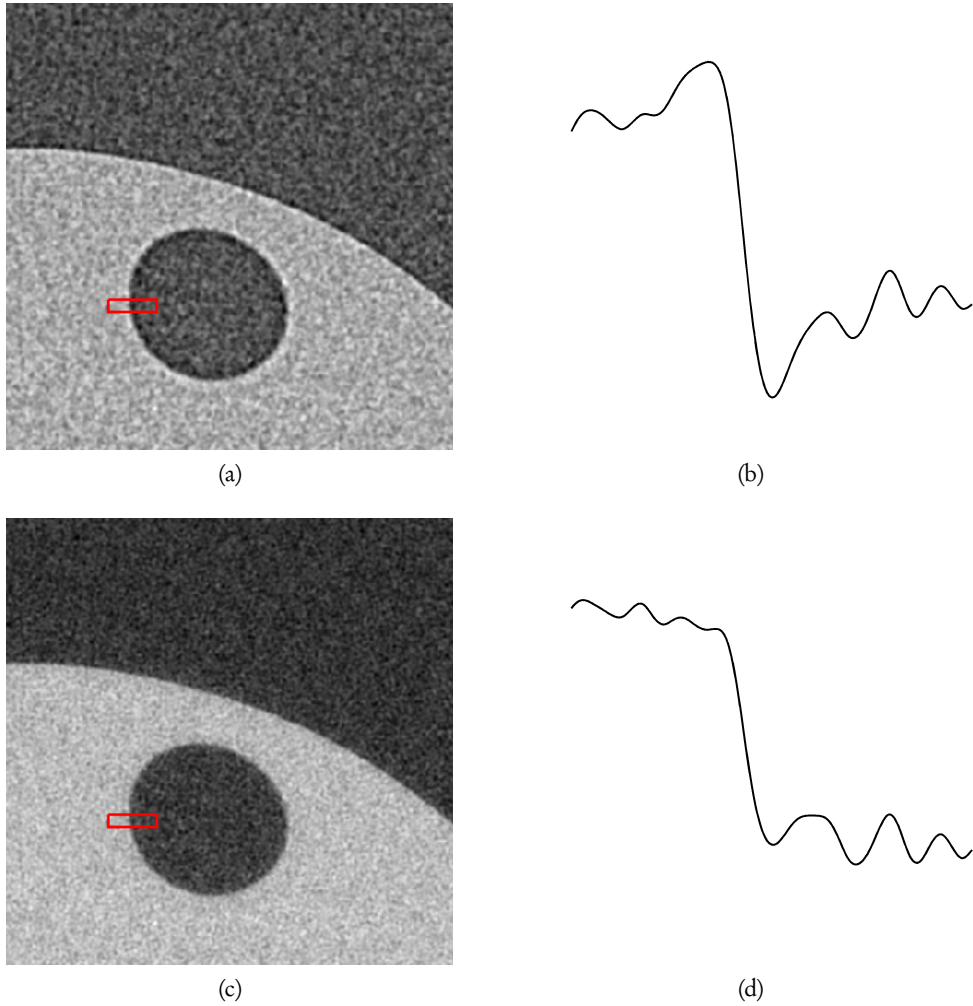


Figure 20: Absorption retrieval with the method presented in Paper I using the method of this appendix for parameter selection. For the visualisations, images are low pass filtered with a Gaussian kernel, with $\sigma = 1$, and stretched maximally. a: A tomogram with both absorption and phase contrast. The box at the edge indicates where a 1-D signal is extracted by averaging across the length direction. b: The extracted edge profile. c: After absorption retrieval, with parameters extracted from the edge profile in (b). d: The profile extracted from (c), i.e., after the absorption retrieval.

B Series for KDEs on S^1 and S^2

In Chapter 5 we saw that kernel density estimation (KDE) of directional data on the circle, S^1 , and sphere S^2 is useful for representing the distribution of gradients around a point in an image. In this appendix we will show the details on how to express them as truncated series, which allows efficient computation. This way of representing KDEs is already used in Paper VIII and VI but we also show application for scale space construction at the end of this appendix.

The starting point is the same for S^1 , and S^2 . Let there be N observations of angles. We will determine the distribution of these using a KDE, [91]. The KDE is a linear combination of weighting functions w centered at the observations

$$K(\mathbf{x}) = \sum_{i=1}^N w(\mathbf{x} - \mathbf{x}_i), \quad \mathcal{D}(K) \rightarrow \mathbb{R}, \quad (106)$$

where the domain, \mathcal{D} of the KDE is first S^1 and then S^2 in the following.

B.1 S^1

The functions $\exp(ik\theta)$ form an orthonormal basis on $[-\pi, \pi]$ with the scalar product $\langle a, b \rangle = \int a b^*$. A KDE on S^1 will be called K_1 and using the exponentials it can be expressed as

$$K_1 = \sum_{k=-\infty}^{\infty} c_k e^{ik\theta}, \quad S^1 \rightarrow \mathbb{R}. \quad (107)$$

Taking the scalar product with the basis functions on both sides, we get

$$c_k = \langle K, e^{-ik\theta} \rangle = \frac{1}{2\pi} \int_{-\pi}^{\pi} K e^{-ik\theta} d\theta = \frac{1}{2\pi} \int_{-\pi}^{\pi} \sum_{i=1}^N \{w(\theta - \theta_i)\} e^{-ik\theta} d\theta. \quad (108)$$

Since the domain is cyclic, we can change the integration bounds to $(-\infty, \infty)$ as long as $w \in L_2$, the space of square integrable functions over \mathbb{R} . Changing the order of summation get:

$$c_k = \frac{1}{2\pi} \sum_{i=1}^N \left\{ \int_{-\infty}^{\infty} w(\theta - \theta_i) e^{-ik\theta} d\theta \right\}. \quad (109)$$

If we consider one term at a time and set $c_k = \sum_{i=1}^N c_{ki}$, the addition from each individual θ_i is

$$c_{ki} = \frac{1}{2\pi} \int_{-\infty}^{\infty} w(\theta - \theta_i) e^{-ik\theta} d\theta. \quad (110)$$

We choose to use a Gaussian weighting function, one that also was proposed by Parzen, which has the form

$$w(\theta) = \frac{1}{\sqrt{2\pi\sigma_w^2}} e^{-\frac{\theta^2}{2\sigma_w^2}}. \quad (111)$$

When Eq. 109 is integrated we find the coefficients as:

$$c_k = \frac{1}{2\pi} e^{-\frac{k^2\sigma_w^2}{2}} \sum_{i=1}^N e^{-ik\theta_i}. \quad (112)$$

The smoothing that is controlled by σ_w has multiple effects. First, it interpolates when the data is sparse. Also, the weighting function acts as a low pass filter, which effectively removes any traces of Gibb's phenomenon, and the smoother the function, the faster it converges as a Fourier series. Note that since the density estimator is real, $c_{-k} = c_k^*$ so only the coefficients for $k \geq 0$ have to be calculated. Also, the first exponential of c_k in Eq. 112 needs to be computed only once and can then be reused.

Truncation is done by keeping only the first $2M - 1$ terms of

$$K_1 = \sum_{k=-\infty}^{\infty} c_k e^{ik\theta} = \underbrace{\sum_{|k| < M} c_k e^{ik\theta}}_{K_{1T}} + \sum_{|k| \geq M} c_k e^{ik\theta}, \quad (113)$$

or rather by not calculating the other terms at all. The amount of terms to keep is a function of the number samples and the desired smoothing.

Implementation as a local image descriptor

When we like to use the KDE in an image, the distribution should most likely be calculated for each position, \mathbf{x} , in that image. To ensure rotational invariance and smoothness, a Gaussian weighting function of the distance to \mathbf{x} is used.

Furthermore, it is usually desired to weight the samples according to the Gradient magnitude, to give details with high contrast more importance. In the experiments, we used $p = 1$ all the time.

With the before mentioned additions and based on Eq. 106 we get the following

$$K_L(\mathbf{x}, \theta) = \sum_{\mathbf{x}_i \in \mathcal{N}_{\mathbf{x}}} \|\nabla I(x_i)\| G_{\sigma_s}(|\mathbf{x} - \mathbf{x}_i|) w(\theta - \theta_i), \quad (114)$$

where $\mathcal{N}_{\mathbf{x}}$ denotes the neighbourhood of \mathbf{x} .

Usually a certain detail level or smoothness of the representation is desired and then σ_w should be set correspondingly. We refer to [91] for a more detailed discussion of this parameter.

The local descriptor K_L given by Eq. 114 has the following properties:

- Invariance to the addition of a constant, C ,

$$K_L(I(\mathbf{x})) = K_L(I(\mathbf{x}) + C). \quad (115)$$

- Invariance to multiplication can be achieved by normalisation of the first coefficient, c_0 , since all coefficients in the Fourier series depend linearly on the image intensity

$$\frac{K_L}{c_0}(C_1 I(\mathbf{x}) + C_2) = \frac{K_L}{c_0}(I(\mathbf{x})). \quad (116)$$

- Rotations of the image equal rotations of the representation, i.e., $K_L(R_\theta I) = R_\theta K_L(I)$ holds. This suggests that lossless alignment of two different representations is possible. That is important when, for example, matching points from different views.
- Group-like behaviour under rotations. For arbitrarily rotation with an angle θ , denoted by R_θ , that means

$$R_\alpha(R_\beta K_L) = R_{\alpha+\beta} K_L. \quad (117)$$

In Fig. 21 some of the benefits of KDEs is shown, where three different representations are used and visualised for the same data set with K_1 , K_{1T} and a histogram.

Detection of extremal directions

Extremal directions can locally be found using steepest gradient descent on the density estimator with

$$\theta_{k+1} = \theta_k + \delta \frac{d}{d\theta} K_L(\theta_k), \quad (118)$$

where δ is the step length. When the number of coefficients are low or σ_w high, all extremal directions can quickly be found by using multiple initial angles.

Alignment

When two distributions are to be compared, rotational invariance is often desired. This can be achieved in multiple ways, the representation can be aligned by rotation of the angle to the maximal mode for example.

Another approach is to first find the opposing nodes from c_2 only, which is best done analytically. $K_L(\theta)$ can then be evaluated at those directions to find the maximal among them.

B.2 S^2

Spherical harmonics are the counterparts to Fourier series on the sphere. They constitute an orthonormal basis for the space of square integrable functions on S^2 under the norm, $\langle a, b \rangle = \int_{S^2} a b^*$. If we parameterise the unit vector by

$$\mathbf{x} = (\cos \theta \sin \phi, \sin \theta \sin \phi, \cos \phi), \quad (119)$$

then the spherical harmonics are

$$Y_{lm}(\theta, \phi) = L_{lm} P_l^m(\cos \phi) e^{im\theta}, \quad l \in \mathbb{N}, |m| \leq l, \quad (120)$$

where L_{lm} are normalisation constants,

$$L_{lm} = \left(\frac{2l+1}{4\pi} \frac{(l-m)!}{(l+m)!} \right)^{1/2}, \quad (121)$$

and P_l^m are the associated Legendre functions (be aware, there are several definitions with different normalisation)

$$P_l^m(x) = \frac{(-1)^m (1-x^2)^{m/2}}{2^l l!} \frac{d^{l+m}}{dx^{l+m}} (x^2-1)^l. \quad (122)$$

We define K_2 as a KDE on S^2 by

$$K_2(\theta, \phi) = \sum_l \sum_m c_{lm} Y_{lm}, \quad S^2 \rightarrow \mathbb{R}. \quad (123)$$

The coefficients are once again found by applying the scalar product with the basis functions on both sides. This time we use a Dirac impulse function, δ as weighting function. That makes a pretty bad estimation of the

distribution of the directions but we will fix that a little later. For a sample with direction (θ, ϕ) , we find the coefficients by:

$$c_{lm} = \langle \delta(\theta, \phi), Y_{lm} \rangle = Y_{lm}^*(\theta, \phi). \quad (124)$$

B.3 Averaging and the diffusions equation

There are several definitions of convolution on spheres and those convolutions are in general non-commutative. Averaging is better solved by a diffusion approach instead.

Such approach is described in [25] where it is used for smoothing of three-dimensional shapes but in this subsection it is modified to represent directional data.

On regular grids, the Gaussian function is the Green's solution to the Laplace equation, i.e., the diffusion or heat equation,

$$\frac{d}{dt}f = -\Delta f. \quad (125)$$

For example, for the interval $[-\pi, \pi]$, we have

$$\frac{d}{dt}f = -\Delta e^{-ikx} = -k^2 e^{-ikx}, \quad (126)$$

and we find that $f = e^{-tk^2} e^{-ikx}$, which is in correspondence with Eq. 112. On the Sphere, we have

$$\Delta_{S^2} Y_{lm} = -l(l+1)Y_{lm}, \quad (127)$$

so the solution to the diffusion equation is

$$Y_{lm}(\theta, \phi, t) = e^{-tl(l+1)} Y_{lm}. \quad (128)$$

One could argue that locally and for small t , the solution to this diffusion equation is similar to the diffusion equation in the plane. And since the diffusion equation in the plane can be expressed in terms of Fourier coefficients as well, we could find an approximate relation between t in Eq. 128 and σ for a 2-D Gaussian distribution.

For both S^1 and S^2 , the diffusion preserves the total probability or the integral over the domain. This is clear since the average is the same as taking the scalar product with Y_{00} and hence the other basis functions does not contribute to the average. Also, c_{00} is not affected by the diffusion.

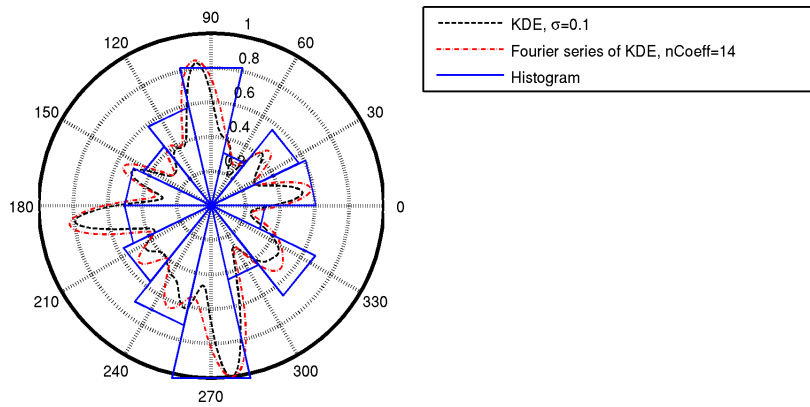


Figure 21: Figure showing three different representations of an angular distribution. Kernel density estimator, the first 14 coefficients of the KDE and also a histogram with 14 bins.

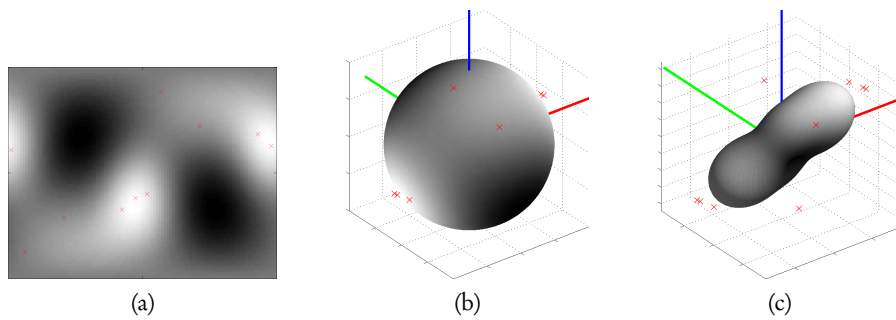


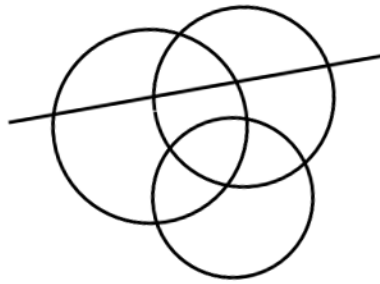
Figure 22: K_2 calculated from five symmetric sample pairs chosen randomly in S^2 . Hence, the samples are represented by spherical harmonics. Here the order is 5 and $kt = .18$. a: Shown with an equirectangular projection. b: Shown on a sphere. c: Shown as a glyph, i.e., as deformations of a sphere.

B.4 Orientation space construction

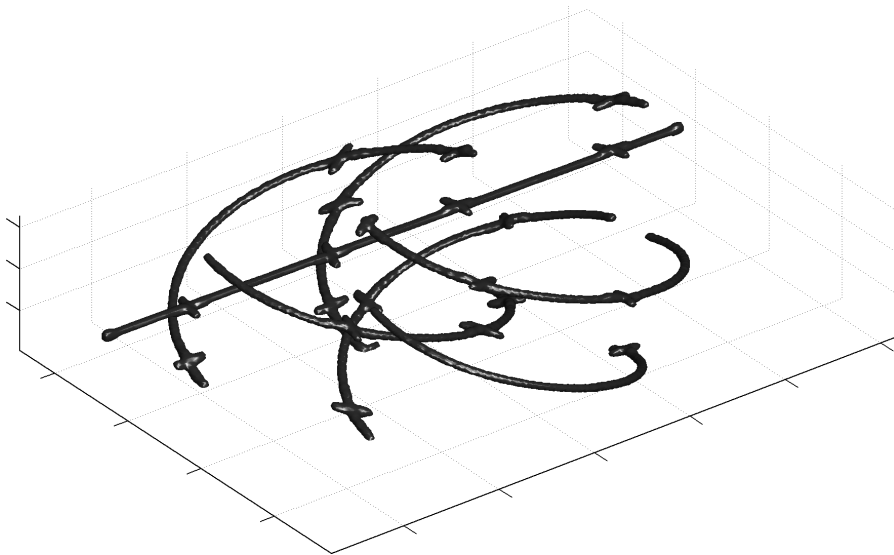
Orientation space or ρ -space as it was called originally by Deborah Walters [112] is the extension of a two-dimensional image into a three-dimensional one, where the third dimension represents local orientation. This method is thoroughly discussed especially on the filter side in the very readable PhD thesis of Michael van Ginkel [110].

In contrast to van Ginkel's approach, we have in Fig. 23 constructed an orientation space for a planar image using K_1 , while he uses the structure tensor with quadrature filters.

For each pixel I've used seven coefficients of K_1 , $\sigma_s = 6$, $\sigma_w = 0.25$. The modes were calculated using steepest descent in Eq. 118 starting from six uniformly distributed angles. The maxima were then discretised and put into a volumetric image. Isosurfaces were then extracted and rendered. Since K_1 can have several maxima, there can also be several orientation values per pixel. One desirable property of the mapping to the orientation space that can be seen in Fig. 23 is that overlapping objects are completely separated while they are still individually connected.



(a)



(b)

Figure 23: An orientation space representation of the figure in (a) is shown in (b). Notice that multiple directions are detected at the intersections.

C Jacobi's method

A problem that occurs when working with the structure tensor is to find eigenvectors and eigenvalues to symmetric matrices with real entries. For example, to get the orientation at each pixel in a slice of size $N \times N$ pixels, as in Paper VIII the eigenvector problem has to be solved N^2 times. To calculate curvature in a volumetric image with the method of Paper III; eigenvalues and eigenvectors have to be calculated three times for each pixel.

M. van Ginkel [110] proposed that the eigenvalues to symmetric and real 3×3 matrices, A , should be found from the characteristic equation, $\det(Ax - \lambda\mathbf{1})$, with Cardano's formula. Such approach is conceptually simple but not well suited for numerical computations [49].

Jacobi's method is an alternative to Cardano's formula for these problems. It has lower error bounds for both eigenvalue and eigenvector than any other known method [35]. Here follows an algorithmic presentation of Jacobi's method, which is based on my implementation.

C.1 Algorithm and implementation

Before discussing 3×3 matrices we say a few words about 2×2 matrices. Such matrices can be expressed as

$$M = \begin{pmatrix} \alpha & \gamma \\ \gamma & \beta \end{pmatrix}, \quad (129)$$

and can be diagonalised by a plane rotation matrix

$$R(\theta) = \begin{pmatrix} \cos \theta & -\sin \theta \\ \sin \theta & \cos \theta \end{pmatrix}, \quad (130)$$

so that

$$R^{-1}MR = D. \quad (131)$$

D and M are similar after the rotation, that is they have the same eigenvalues. The eigenvalues are on the diagonal of D and the eigenvectors are in the columns of R .

R is described by the rotation angle θ . There are different ways to find θ , and, for fast implementation on current CPUs, trigonometric functions should be avoided. The following well known [90] formulas seem to be a good alternative:

$$\epsilon = \frac{\alpha - \beta}{2\gamma}, \quad (132a)$$

$$t = \frac{\text{sign } \epsilon}{|\epsilon| + \sqrt{1 + \epsilon^2}}, \quad (132b)$$

$$c := \cos \theta = (1 + t^2)^{-1/2}, \quad \text{and,} \quad s := \sin \theta = ct. \quad (132c)$$

When Eq. 131 is written out explicitly with the formulas above,

$$\begin{pmatrix} c & -s \\ s & c \end{pmatrix} \begin{pmatrix} \alpha & \gamma \\ \gamma & \beta \end{pmatrix} \begin{pmatrix} c & s \\ -s & c \end{pmatrix} = \begin{pmatrix} \alpha - \gamma t & 0 \\ 0 & \beta + \gamma t \end{pmatrix}.$$

From the plane rotation matrix, rotation matrices for 3×3 matrices can be constructed, called Jacobi rotations (note the relationship to Euler angles, and the similarity to Given's rotations). There are three of them to be used with 3×3 matrices, which will be denoted

$$R_{12} = \begin{pmatrix} c_1 & -s_1 & 0 \\ s_1 & c_1 & 0 \\ 0 & 0 & 1 \end{pmatrix}, R_{13} = \begin{pmatrix} c_2 & 0 & -s_2 \\ 0 & 1 & 0 \\ s_2 & 0 & c_2 \end{pmatrix}, R_{23} = \begin{pmatrix} 1 & 0 & 0 \\ 0 & c_3 & -s_3 \\ 0 & s_3 & c_3 \end{pmatrix}. \quad (133)$$

The core of the Jacobi method is to use these matrices iteratively to diagonalise A . In theory A can be diagonalised by $R_{12}R_{13}R_{23}A(R_{12}R_{13}R_{23})^{-1}$, that is by three rotations only. But to find the corresponding angles directly is harder than to diagonalise A iteratively.

With the Jacobi method A is rotated so that one off-diagonal element is eliminated at each step. Other off-diagonal elements might grow at each iteration but the method can be shown to have quadratic convergence [90].

Here is an outline of the algorithm that is implemented:

1. $n = 0$. Input: $A_n := A$. Initialise $E_n := \mathbb{1}$, which will contain the eigenvectors at convergence. Set the tolerances value $t = 10^{-14}$.
2. Find the location of the largest off-diagonal element in $A_n(i, j)$,

$$(i, j) = \arg \max |A_n(i, j)|, \quad i < j. \quad (134)$$

3. Find c and s of Eq. 132 using

$$\alpha = A_n(i, i), \quad \beta = A_n(j, j), \quad \gamma = A_n(i, j). \quad (135)$$

4. Rotate A , $A_n := R_{ij}A_{n-1}R_{ij}^T$.
5. Rotate E , $E_n := R_{ij}^TE_{n-1}$.
6. If $\max_{i \neq j} |A_n(i, j)| < t$ end, else: $n = n + 1$, repeat from step 2.

C.2 Discussion

It might not be obvious that the eigenvalues will be stored in E at the end, but if we denote the applied rotations by J_1, J_2, \dots, J_n then at the final step n

$$A_n = \left(\prod J_i\right) A_0 \left(\prod J_i^T\right). \quad (136)$$

Since A_n is diagonal its eigenvectors are $V_1 = (1, 0, 0)^T$, $V_2 = (0, 1, 0)^T$ and $V_3 = (0, 0, 1)^T$. That gives,

$$A_n V_i = \lambda_i V_i, \quad (137)$$

or

$$\left(\prod J_i\right) A_0 \left(\prod J_i^T\right) V_i = \lambda_i V_i, \quad (138)$$

so,

$$A_0 \left(\prod J_i^T\right) V_i = \lambda_i \left(\prod J_i\right)^{-1} V_i = \lambda_i \left(\prod J_i^T\right) V_i, \quad (139)$$

and hence $\left(\prod J_i^T\right) V_i$ is an eigenvector to A_0 with eigenvalue λ_i .

Taking into account symmetries and explicitly writing out the matrix multiplications the number of multiplications can be kept low. We have compared our implementation to the one found in DIPimage (<http://www.diplib.org/>), called `dip_symmetriceigensystem3`, based on Cardano's formula. Our implementation of Jacobi's method is 30% faster than the implementation in DIPimage while the precision is at least the same.

References

- [1] C. Antoine, P. Nygård, Ø. W. Gregersen, R. Holmstad, T. Weitkamp and C. Rau, “3D images of paper obtained by phase-contrast X-ray microtomography: image quality and binarisation”, *Nuclear Instruments and Methods in Physics Research Section A: Accelerators, Spectrometers, Detectors and Associated Equipment*, vol. 490, no. 1–2, pp. 392–402, 2002 (cit. on p. 18).
- [2] B. Appleton and H. Talbot, “Globally minimal surfaces by continuous maximal flows”, *IEEE Transactions on Pattern Analysis and Machine Intelligence (PAMI)*, vol. 28, no. 1, pp. 106–118, 2006 (cit. on pp. 28, 65, 68, 69).
- [3] M. Aronsson, “On 3D fibre measurements of digitized paper – from microscopy to fibre network”, *Acta Universitatis agriculturae Sueciae. Silvestria*, 254, PhD thesis, Swedish University of Agricultural Sciences, 2002 (cit. on pp. 13, 17).
- [4] M. Aronsson and G. Borgefors, “2D segmentation and labelling of clustered ring shaped objects”, in *Scandinavian Conference on Image Analysis*, 2001, pp. 272–279 (cit. on p. 18).
- [5] M. Axelsson, “3D tracking of cellulose fibres in volume images”, in *IEEE International Conference on Image Processing (ICIP)*, vol. 4, 2007, pp. 309–312 (cit. on p. 17).
- [6] M. Axelsson, “Estimating 3D fibre orientation in volume images”, in *International Conference on Pattern Recognition (ICPR)*, 2008, pp. 1–4 (cit. on p. 17).
- [7] M. Axelsson, “Image analysis for volumetric characterisation of microstructure”, Thesis No. 2009:19, PhD thesis, Swedish University of Agricultural Sciences, 2009 (cit. on pp. 13, 17).
- [8] J. Bache-Wiig and P. C. Henden, “Individual fiber segmentation of three-dimensional microtomograms of paper and fiber-reinforced composite materials”, Master’s thesis, Norwegian University of Science and Technology, Trondheim, 2005 (cit. on p. 17).
- [9] H. Bårman, G. H. Granlund and H. Knutsson, “A new approach to curvature estimation and description”, in *Third International Conference on image Processing and its Applications*, 1989, pp. 54–58 (cit. on p. 55).

- [10] H. Bårman, G. H. Granlund and H. Knutsson, “Estimation of curvature in 3D images using tensor field filtering”, in *European Conference on Computer Vision (ECCV), Lecture Notes in Computer Science* 437, 1990, pp. 563–565 (cit. on p. 55).
- [11] H. Bårman, “Hierarchical curvature estimation in computer vision”, Dissertation No 253, ISBN 91-7870-797-8, PhD thesis, Linköping University, Sweden, SE-581 83 Linköping, Sweden, 1991 (cit. on p. 55).
- [12] T. Barrera, A. Hast and E. Bengtsson, “Trigonometric splines”, in *Game Programming Gems*, Charles River Media, 2008, pp. 191–198 (cit. on p. 44).
- [13] J. Besag, “On the statistical analysis of dirty pictures”, *Journal of the Royal Statistical Society. Series B (Methodological)*, vol. 48, no. 3, pp. 259–302, 1986 (cit. on p. 65).
- [14] M. Boone, E. L. G. Wernersson, M. Dierick, L. Brabant, E. Pauwels, C. L. Luengo Hendriks and L. Van Hoorebeke, “Comparison of several phase retrieval and phase correction methods for single-image in-line X-ray phase contrast tomography”, in *Proceedings of IEEE 10th International symposium on biomedical imaging: From nano to macro*, abstract, San Francisco, CA, USA, 2013 (cit. on p. 8).
- [15] M. N. Boone, W. Devulder, M. Dierick, L. Brabant, E. Pauwels and L. Van Hoorebeke, “Comparison of two single-image phase-retrieval algorithms for in-line X-ray phase-contrast imaging”, *Journal of the Optical Society of America A*, vol. 29, no. 12, pp. 2667–2672, 2012 (cit. on p. 18).
- [16] M. Boone, “New imaging modalities in high resolution X-ray tomography”, PhD thesis, Ghent University, Belgium, 2013, XXVI, 291 [in multiple pagination] (cit. on p. 39).
- [17] G. Borgefors, “A hierarchical "square" tessellation of the sphere”, *Pattern Recognition Letters*, vol. 13, no. 3, pp. 183–188, Mar. 1992 (cit. on p. 43).
- [18] M. Born and E. Wolf, *Principles of optics 7th ed.* Cambridge University press, 1999 (cit. on pp. 32, 33, 36).
- [19] Y. Boykov and V. Kolmogorov, “An experimental comparison of min-cut/max-flow algorithms for energy minimization in vision”, *IEEE Transactions on Pattern Analysis and Machine Intelligence (PAMI)*, vol. 26, no. 9, pp. 1124–1137, 2004 (cit. on p. 65).

- [20] Y. Boykov, O. Veksler and R. Zabih, “Fast approximate energy minimization via graph cuts”, *IEEE Transactions on Pattern Analysis and Machine Intelligence (PAMI)*, vol. 23, no. 11, pp. 1222–1239, 2001 (cit. on p. 65).
- [21] Y. Boykov and G. Funka-Lea, “Graph cuts and efficient n-d image segmentation”, *International Journal of Computer Vision*, vol. 70, no. 2, pp. 109–131, 2006 (cit. on p. 65).
- [22] E. O. Brigham, *The Fast Fourier Transform*. Prentice-Hall, 1974 (cit. on p. 28).
- [23] A. V. Bronnikov, “Theory of quantitative phase-contrast computed tomography”, *Journal of the Optical Society of America A*, vol. 19, no. 3, pp. 472–480, 2002 (cit. on pp. 36, 40).
- [24] A. Brun, C. Westin, M. Herberthson and H. Knutsson, “Intrinsic and extrinsic means on the circle - a maximum likelihood interpretation”, in *IEEE International Conference on Acoustics, Speech and Signal Processing (ICASSP)*, vol. 3, 2007, pp. III-1053–III-1056 (cit. on p. 44).
- [25] T. Bülow, “Spherical diffusion for 3D surface smoothing”, *IEEE Transactions on Pattern Analysis and Machine Intelligence (PAMI)*, vol. 26, no. 12, pp. 1650–1654, 2004 (cit. on p. 95).
- [26] J. Canny, “A computational approach to edge detection”, *IEEE Transactions on Pattern Analysis and Machine Intelligence (PAMI)*, vol. 8, pp. 679–97, 1986 (cit. on p. 27).
- [27] G. Chinga-Carrasco, A. Miettinen, C. L. Luengo Hendriks, E. K. Gamstedt and M. Kataja, “Nanocomposites and polymers with analytical methods”, in J. Cuppoletti, Ed. *InTech*, 2011, ch. Structural characterisation of kraft pulp fibres and their nanofibrillated materials for biodegradable composite applications (cit. on p. 13).
- [28] K. Choi, J. Wang, L. Zhu, T.-S. Suh, S. Boyd and L. Xing, “Compressed sensing based cone-beam computed tomography reconstruction with a first-order method”, *Medical Physics*, vol. 37, no. 9, pp. 5113–5125, 2010 (cit. on p. 32).
- [29] P. Cloetens, M. Pateyron-Salomé, J. Buffière, G. Peix, J. Baruchel, F. Peyrin and M. Schlenker, “Observation of microstructure damage in materials by phase sensitive radiography and tomography”, *Journal of Applied Physics*, vol. 81, no. 9, pp. 5878–5886, 1997 (cit. on p. 36).

- [30] D. Coeurjolly and S. Svensson, “Estimation of curvature along curves with application to fibres in 3D images of paper”, in *Proceedings of the 13th Scandinavian conference on Image analysis*, ser. SCIA’03, Halmstad, Sweden: Springer-Verlag, 2003, pp. 247–254 (cit. on pp. 17, 49).
- [31] H. S. M. Coexer, *Regular Polytopes*. Dover Publications, Inc, 1973 (cit. on p. 43).
- [32] J. W. Cooley and J. W. Tukey, “An algorithm for the machine calculation of complex fourier series”, *Mathematics of Computation*, vol. 19, pp. 297–301, 1965 (cit. on p. 29).
- [33] A. M. Cormack, “Representation of a function by its line integrals, with some radiological applications”, *Journal of Applied Physics*, vol. 34, no. 9, pp. 2722–2727, 1963 (cit. on p. 31).
- [34] A. M. Cormack, “Representation of a function by its line integrals, with some radiological applications. ii”, *Journal of Applied Physics*, vol. 35, no. 10, pp. 2908–2913, 1964 (cit. on p. 31).
- [35] J. Demmel and K. Veselić, “Jacobi’s method is more accurate than QR”, *SIAM. J. Matrix Anal. & Appl.*, vol. 13, no. 4, pp. 1204–1245, 1992 (cit. on p. 99).
- [36] E. W. Dijkstra, “A note on two problems in connexion with graphs”, *Numerische Mathematik*, vol. 1, no. 1, pp. 269–271, 1959 (cit. on p. 65).
- [37] M. Donoser, “Advanced segmentation and tracking algorithms and their application to 3D paper structure analysis”, PhD thesis, Graz University of Technology, 2007 (cit. on p. 17).
- [38] M. Donoser, T. Mauthner, H. Bischof and J. Kritzinger, “A probabilistic approach for tracking fibers”, in *19th Int. Conf. on Pattern Recognition*, 2008, pp. 1–4 (cit. on p. 17).
- [39] J. Edmonds and R. M. Karp, “Theoretical improvements in algorithmic efficiency for network flow problems”, *Journal of the Association for Computing Machinery (ACM)*, vol. 19, no. 2, pp. 248–264, Apr. 1972 (cit. on p. 65).
- [40] M. Elad, *Sparse and Redundant Representations*. Springer, 2010 (cit. on p. 32).
- [41] F. G. A. Faas, “Orientation analysis; multi-valuedness and shape descriptors”, PhD thesis, Delft University of Technology, 2010 (cit. on p. 43).

- [42] A. Falcão, J. Stolfi and R. de Alencar Lotufo, “The image foresting transform: theory, algorithms, and applications”, *IEEE Transactions on Pattern Analysis and Machine Intelligence (PAMI)*, vol. 26, no. 1, pp. 19–29, 2004 (cit. on p. 80).
- [43] G. Farnebäck and C.-F. Westin, “Improving Deriche-style recursive gaussian filters”, *Journal of Mathematical Imaging and Vision*, vol. 26, no. 3, pp. 293–299, 2006 (cit. on p. 29).
- [44] Food and Agriculture Organization of the United Nations. (2014). Forest products statistics, [Online]. Available: <http://www.fao.org/forestry/statistics/80938/en/> (visited on 16/09/2014) (cit. on p. 14).
- [45] L. R. Ford and D. R. Fulkerson, “Maximal flow through a network”, *Canadian Journal of Mathematics*, vol. 8, pp. 399–404, 1956 (cit. on p. 65).
- [46] D. Fransson, “Noise reduction of X-ray microtomography images of paper using anisotropic filtering methods”, UPTTECH F07 009, Masters thesis, Uppsala University, 2007, p. 67 (cit. on p. 18).
- [47] D. J. Gates and M. Westcott, “Predicting fiber contact in a three-dimensional model of paper”, *Journal Of Statistical Physics*, vol. 94, no. 1/2, 1999 (cit. on p. 19).
- [48] A. V. Goldberg and R. E. Tarjan, “A new approach to the maximum-flow problem”, *Journal of the Association of Computing Machinery (ACM)*, vol. 35, no. 4, pp. 921–940, Oct. 1988 (cit. on pp. 65, 67).
- [49] G. H. Golub and H. A. van der Vorst, “Eigenvalue computation in the 20th century”, *Journal of Computational and Applied Mathematics*, vol. 123, pp. 35–65, 2000 (cit. on p. 99).
- [50] R. C. Gonzales and R. E. Woods, *Digital Image Processing*. Pearson, 2008 (cit. on p. 25).
- [51] G. H. Granlund and H. Knutsson, *Signal Processing for Computer Vision*. Kluwer Academic Press, 1995 (cit. on pp. 42, 44, 55).
- [52] G. H. Granlund, “In search of a general picture processing operator”, *Computer Graphics and Image Processing*, vol. 8, pp. 155–173, 1978 (cit. on p. 42).
- [53] D. M. Grieg, B. T. Porteous and A. H. Seheult, “Exact minimim a posteori estimation for binary images”, *Journal of the Royal Statistical Society. Series B.*, vol. 51, no. 2, pp. 271–279, 1989 (cit. on p. 65).

- [54] D. J. Griffiths, *Introduction to electrodynamics*. Prentice Hall, 1999 (cit. on p. 32).
- [55] P. A. Grillet, *Abstract Algebra*, 2nd. Springer, 1999 (cit. on p. 25).
- [56] M. Hagen, R. Holen, R. Holmstad and R. Blake, “Digital identification of connected paper fibres with cracks”, *Progress in paper physics*, 2004 (cit. on p. 17).
- [57] R. Hamming, *Numerical Methods for Scientists and Engineers*. Dover Publications; 2nd edition, 1987 (cit. on p. 25).
- [58] J. G. Haygreen and J. L. Bowlyer, *Forest Products and Wood Science*, Third. The Iowa State University Press, 1996 (cit. on p. 15).
- [59] M. T. Heidman, D. H. Johnson and C. S. Burrus, “Gauss and the history of the fast fourier transform”, *Archive for History of Exact Sciences*, vol. 34, no. 3, pp. 265–77, 1985 (cit. on p. 29).
- [60] U. Hirn and W. Bauer, “A review of image analysis based methods to evaluate fiber properties”, *Lenzinger Berichte*, vol. 86, 2006 (cit. on pp. 13, 23).
- [61] R. Holen and M. Hagen, “Segmentation of absorption mode X-ray micro tomographic images of paper”, Master’s thesis, Norwegian University of Science and Technology, Trondheim, 2004 (cit. on p. 17).
- [62] T. Joffre, E. K. Gamstedt, A. Miettinen and E. L. G. Wernersson, *Effects of fibre agglomeration on strength of wood-fibre composites*, Workshop: Mixed numerical and experimental methods applied to the mechanical characterization of bio-based materials, Vila Real, Portugal, April 27-28, 2011 (cit. on p. 9).
- [63] T. Joffre, A. Miettinen, E. L. G. Wernersson, P. Isaksson and E. K. Gamstedt, “Effects of defects on the tensile strength of short-fibre composite materials”, *Mechanics of Materials*, vol. 75, pp. 125–134, 2014 (cit. on p. 7).
- [64] T. Joffre, E. L. G. Wernersson, A. Miettinen, C. L. Luengo Hendriks and E. K. Gamstedt, “Swelling of cellulose fibres in composite materials: constraint effects of the surrounding matrix”, *Composites Science and Technology*, vol. 74, pp. 52–59, 2013 (cit. on p. 8).
- [65] A. Kak and M. Slaney, *Principles of Computerized Tomographic Imaging*. IEEE Press, 1999 (cit. on pp. 31–33).

- [66] G. Kindlmann, R. Whitaker, T. Tasdizen and T. Möller, “Curvature-based transfer functions for direct volume rendering: methods and applications”, in *Proceedings of IEEE Visualization*, 2003 (cit. on p. 47).
- [67] H. Knutsson and M. Andersson, “What’s so good about quadrature filters?”, in *International Conference on Image Processing (ICIP 2003)*, vol. 3, 2003, pp. 61–64 (cit. on p. 42).
- [68] H. Knutsson and G. H. Granlund, “Texture Analysis Using Two-Dimensional Quadrature Filters”, in *IEEE Computer Society Workshop on Computer Architecture for Pattern Analysis and Image Database Management - CAPAIDM*, Pasadena, 1983 (cit. on p. 42).
- [69] J. J. Koenderink, “The structure of images”, *Biological Cybernetics*, vol. 50, pp. 363–370, 1984 (cit. on p. 28).
- [70] J. J. Koenderink and A. J. van Doorn, “Surface shape and curvature scales”, *Image and Vision Computing*, vol. 10, no. 8, 2002 (cit. on p. 62).
- [71] E. Kreyszig, *Differential Geometry*. Dover Publications, 1991 (cit. on pp. 48, 52).
- [72] D. Lesage, E. D. Angelini, I. Bloch and G. Funka-Lea, “A review of 3D vessel lumen segmentation techniques: models, features and extraction schemes”, *Medical Image Analysis*, vol. 13, pp. 819–845, 2009 (cit. on p. 13).
- [73] J. Lindblad, N. Sladoje and T. Lukic, “De-noising of SR μ CT fiber images by total variation minimization”, in *International Conference on Pattern Recognition (ICPR)*, IEEE, 2010, pp. 4621–4624 (cit. on p. 18).
- [74] T. Lindeberg, “Scale-space”, in *Encyclopedia of Computer Science and Engineering*, vol. 4, John Wiley and Sons, 2009, pp. 2495–2504 (cit. on pp. 28, 44).
- [75] T. Linder, “Light scattering in fiber-based materials: a foundation for characterization of structural properties”, PhD thesis, Luleå tekniska universitet, Sweden, 2014 (cit. on p. 31).
- [76] T. Linder, T. Löfqvist, E. L. G. Wernersson and P. Gren, “Light scattering in fibrous media with different degrees of in-plane fiber alignment”, *Optics Express*, vol. 22, no. 14, pp. 16 829–16 840, 2014 (cit. on p. 7).

- [77] S. G. Lipson and H. Lipson, *Optical Physics*. Cambridge University Text, 1981 (cit. on p. 32).
- [78] D. G. Lowe, “Object recognition from local scale-invariant features”, in *International Conference on Computer Vision*, 1999, pp. 1150–1157 (cit. on p. 42).
- [79] D. G. Lowe, “Distinctive image features from scale-invariant keypoints”, *International Journal of Computer Vision*, vol. 60, no. 2, pp. 91–110, 2004 (cit. on pp. 42, 43).
- [80] C. L. Luengo Hendriks, “Revisiting priority queues for image analysis”, *Pattern Recognition*, vol. 43, no. 9, pp. 3003–3012, 2010 (cit. on p. 67).
- [81] J. Lunden, “Image analysis methods for evaluation of fibre dimensions in paper cross-sections”, Master’s thesis, Royal Institute of Technology, Stockholm, Sweden, 2002 (cit. on p. 17).
- [82] R. Machuca and K. Phillips, “Applications of vector fields to image processing”, *IEEE Transactions on Pattern Analysis and Machine Intelligence (PAMI)*, vol. 5, no. 3, 1983 (cit. on p. 47).
- [83] F. Malmberg, J. Lindblad, N. Sladoje and I. Nyström, “A graph-based framework for sub-pixel image segmentation”, *Theoretical Computer Science*, vol. 412, no. 15, pp. 1338–1349, 2011, *Theoretical Computer Science Issues in Image Analysis and Processing* (cit. on p. 66).
- [84] F. Malmberg, J. Lindblad, C. Östlund, K. Almgren and E. K. Gamstedt, “An automated image analysis method for measuring fibre contact in fibrous and composite materials”, in *Proceedings of 13th European Conference on Composite Materials, Stockholm*, 2008 (cit. on pp. 19, 78).
- [85] F. Malmberg, C. Östlund and G. Borgefors, “Binarization of phase contrast volume images of fibrous materials: a case study”, in *International Conference on Computer Vision Theory and Applications (VISAPP 2009), Lisboa, Portugal*, 2009 (cit. on p. 19).
- [86] A. Marais, M. S. Magnusson, T. Joffre, E. L. G. Wernersson and L. Wågberg, “New insights into the mechanisms behind the strengthening of lignocellulosic fibrous networks with polyamines”, *Cellulose*, pp. 1–10, 2014 (cit. on pp. 8, 19).

- [87] C. Marulier, P. Dumont, L. Orgéas, D. Caillerie and S. R. du Roscoat, “Towards 3D analysis of pulp fibre networks at the fibre and bond levels”, *Nordic Pulp & Paper Research Journal (NPPRJ)*, vol. 27, pp. 245–255, 2 2012 (cit. on pp. 18, 19, 78).
- [88] O. Monga and S. Benayoun, “Using partial derivatives of 3D images to extract typical surface features”, in *IEEE Computer Vision and Pattern Recognition (CVPR)*, Also INRIA Research Report 1599, 1992 (cit. on p. 53).
- [89] O. Monga, N. Ayache and P. Sander, “From voxel to curvature”, in *IEEE Computer Vision and Pattern Recognition, Washington, DC*, 1991 (cit. on p. 47).
- [90] B. N. Parlett, *The Symmetric Eigenvalue Problem*. Society for Industrial and Applied Mathematics, 1998 (cit. on pp. 99, 100).
- [91] E. Parzen, “On estimation of a probability density function and mode”, *Annals of Mathematical Statistics*, vol. 33, no. 3, pp. 1065–1076, 1962 (cit. on pp. 43, 91, 93).
- [92] J. Radon, “On the determination of functions from their integral values along certain manifolds”, *IEEE Transactions on Medical Imaging*, vol. 5, no. 4, pp. 170–176, 1986 (cit. on p. 31).
- [93] B. Rieger, F. J. Timmermans, L. J. van Vliet and P. W. Verbeek, “On curvature estimation of iso surfaces in 3D gray-value images and the computation of shape descriptors”, *IEEE Transactions on Pattern Analysis and Machine Intelligence (PAMI)*, vol. 26, no. 8, pp. 1088–1094, 2004 (cit. on pp. 48, 55, 56, 71, 79).
- [94] E. J. Samuelsen, P.-J. Houen, Ö. W. Gregersen, T. Helle and C. Raven, “Three-dimensional imaging of paper by use of synchrotron X-ray microtomography”, *Proceedings of International Paper Physics Conference*, pp. 307–12, 1999 (cit. on p. 13).
- [95] H. Sarve, “Evaluation of osseointegration using image analysis and visualization of 2D and 3D image data”, PhD thesis, Centrum för bildanalys, Sveriges lantbruksuniversitet, 2011 (cit. on p. 39).
- [96] T. Schultz, J. Weickert and H.-P. Seidel, “A higher-order structure tensor”, in *Visualization and Processing of Tensor Fields – Advances and Perspectives*, D. H. Laidlaw and J. Weickert, Eds., Springer, 2009, pp. 263–280 (cit. on p. 44).
- [97] J. Serra, *Image Analysis and Mathematical Morphology*. Academic press, 1982 (cit. on pp. 28, 42).

- [98] J. A. Sethian, *Level Set Methods and Fast Marching Methods*. Cambridge University Press, 1999 (cit. on p. 28).
- [99] A. Sheldon, *Linear algebra done right*, 2nd. Springer, 2010 (cit. on p. 56).
- [100] I.-M. Sintorn, S. Svensson and M. Axelsson, “Segmentation of individual pores in 3D paper images”, *Nordic Pulp and Paper Research J.*, vol. 20, pp. 316–9, 2005 (cit. on p. 17).
- [101] N. Sladoje and J. Lindblad, “High-precision boundary length estimation by utilizing gray-level information”, *IEEE Transactions on Pattern Analysis and Machine Intelligence (PAMI)*, vol. 31, no. 2, pp. 357–363, 2009 (cit. on p. 26).
- [102] M. Sonka, V. Hlavac and R. Boyle, *Image Processing, Analysis, and Machine Vision*, 3rd ed. Thomson Engineering, 2008 (cit. on p. 25).
- [103] G. Strang, “Maximal flow through a domain”, *Mathematical programming*, vol. 26, pp. 123–143, 1983 (cit. on p. 67).
- [104] J. Sunnegårdh, “Iterative filtered backprojection methods for helical cone-beam ct”, PhD thesis, Linköping Studies in Science and Technology. Dissertations, ISSN 0345-7524; 1264, 2009 (cit. on p. 32).
- [105] S. Svensson and M. Aronsson, “Using distance transform based algorithms for extracting measures of the fiber network in volume images of paper”, *Systems, Man, and Cybernetics, Part B: Cybernetics, IEEE Transactions on*, vol. 33, no. 4, pp. 562–571, 2003 (cit. on p. 17).
- [106] S. Svensson, “Representing and analyzing 3D digital shape using distance information”, PhD thesis, Swedish University of Agricultural Sciences, 2001 (cit. on p. 17).
- [107] J.-P. Thirion and A. Gourdon, “Computing the differential characteristics of iso-intensity surface”, *Comput. Vis. Image Underst.*, vol. 61, pp. 190–202, 2 1995 (cit. on pp. 47, 53).
- [108] C. Tomasi and R. Manduchi, “Bilateral filtering for gray and color images”, in *IEEE International Conference on Computer Vision*, Bombay, India, 1998 (cit. on p. 18).
- [109] J. Van den Bulcke, E. L. G. Wernersson, M. Dierick, D. Van Loo, B. Masschaele, L. Brabant, M. N. Boone, L. Van Hoorebeke, K. Haneca, A. Brun, C. L. Luengo Hendriks and J. Van Acker, “3D tree-ring analysis using helical X-ray tomography”, *Dendrochronologia*, vol. 32, no. 1, pp. 39–46, 2014 (cit. on p. 8).

- [110] M. van Ginkel, “Image analysis using orientation space based on steerable filters”, PhD thesis, ASCI, 2002 (cit. on pp. 97, 99).
- [111] L. J. van Vliet, “Grey-scale measurements in multi-dimensional digitized images”, PhD thesis, Delft University of Technology, Delft University Press, Delft, 1993, p. 259 (cit. on pp. 27, 60).
- [112] D. Walters, “Selection of image primitives for general-purpose visual processing”, *Computer Vision, Graphics, and Image Processing*, vol. 37, no. 2, pp. 261–298, 1987 (cit. on p. 97).
- [113] T. Walther, H. Thoemen, K. Terzic and H. Meine, “New opportunities for the microstructural analysis of wood fibre networks”, in *Proceedings of the Tenth European Panel Products Symposium (EPPS) 2006*, The BioComposites Centre, University of Wales, Llandudno /Wales, UK, Oct. 2006, pp. 23–32 (cit. on p. 17).
- [114] H. Wang and S. M. Shaler, “Computer-simulated three-dimensional microstructure of wood fibre composite materials”, *Journal of Pulp and Paper Science*, vol. 24, no. 10, pp. 314–319, 1998 (cit. on p. 19).
- [115] M. A. Weiss, *Data Structures & Problem Solving Using Java*, Third. Addison Wesley, 2006 (cit. on p. 67).
- [116] E. L. G. Wernersson, M. N. Boone, J. Van den Bulcke, L. Van Hoorbeke and C. L. Luengo Hendriks, “Understanding phase contrast artefacts in micro computed absorption tomography”, in *Proceedings, Symposium on Image Analysis (SSBA)*, Luleå, Sweden, 2014, pp. 40–45 (cit. on pp. 9, 39, 87).
- [117] E. L. G. Wernersson, A. Brun and C. L. Luengo Hendriks, “Closing pores and segmenting individual fibres in 3D images of wood fibre composites using curvature information and graph cuts”, in *Proceedings, Symposium on Image Analysis (SSBA)*, J. Bigun and A. Verikas, Eds., Halmstad, Sweden, 2009, pp. 113–116 (cit. on p. 8).
- [118] E. L. G. Wernersson, M. N. Boone, J. Van den Bulcke, L. Van Hoorbeke and C. L. Luengo Hendriks, “Postprocessing method for reducing phase effects in reconstructed microcomputed-tomography data”, *Journal of the Optical Society of America A (JOSA A)*, vol. 30, no. 3, pp. 455–461, 2013 (cit. on p. 7).
- [119] E. L. G. Wernersson, S. Borodulina, A. Kulachenko and G. Borgefors, “Characterisations of fibre networks in paper using computed tomography images”, *Nordic Pulp & Paper Research Journal (NPPRJ)*, vol. 29, no. 3, pp. 468–475, 2014 (cit. on pp. 7, 18).

- [120] E. L. G. Wernersson, A. Brun and C. L. Luengo Hendriks, “Segmentation of wood fibres in 3D CT images using graph cuts”, in *Proceedings, Image Analysis and Processing, (ICIAP)*, ser. Lecture Notes in Computer Science, P. Foggia, C. Sansone and M. Vento, Eds., vol. 5716, Springer Berlin / Heidelberg, 2009, pp. 92–102 (cit. on pp. 7, 18).
- [121] E. L. G. Wernersson, A. Brun and C. L. Luengo Hendriks, “Calculating curvature from orientation fields in volumetric images”, in *Proceedings, Symposium on Image Analysis (SSBA)*, R. Lenz, Ed., paper 26, 4 pp., Linköping, Sweden, 2011 (cit. on p. 8).
- [122] E. L. G. Wernersson, C. L. Luengo Hendriks and A. Brun, “Robust and unbiased curvature of isophote surfaces in volumetric images”, manuscript (cit. on p. 7).
- [123] E. L. G. Wernersson, C. L. Luengo Hendriks and A. Brun, “Generating synthetic μ CT images of wood fibre materials”, in *Proceedings, 6th International Symposium on Image and Signal Processing and Analysis (ISPA)*, 2009, pp. 365–370 (cit. on p. 7).
- [124] E. L. G. Wernersson, C. L. Luengo Hendriks and A. Brun, “Accurate estimation of gaussian and mean curvature in volumetric images”, in *3D Imaging Modeling Processing Visualization Transmission (3DIMPVT), Hangzhou, China, May 16-19, 2011*, pp. 312–317 (cit. on p. 7).
- [125] M. Wiltsche, M. Donoser, J. Kritzinger and W. Bauer, “Automated serial sectioning applied to 3D paper structure analysis”, *Journal of Microscopy*, vol. 242, no. 2, pp. 197–205, 2011 (cit. on p. 13).
- [126] A. P. Witkin, “Scale-space filtering: a new approach to multi-scale description”, in *IEEE International Conference on Acoustics, Speech, and Signal Processing (ICASSP’84)*, vol. 9, 1984, pp. 150–153 (cit. on p. 28).
- [127] Y.-L. Yang, Y.-K. Lai, S.-M. Hu and H. Pottmann, “Robust principal curvatures on multiple scales”, in *Proceedings of the Fourth Eurographics Symposium on Geometry Processing*, ser. SGP ’06, Cagliari, Sardinia, Italy: Eurographics Association, 2006, pp. 223–226 (cit. on pp. 48, 56).
- [128] J. Yuan, E. Bae, X.-C. Tai and Y. Boykov, “A spatially continuous max-flow and min-cut framework for binary labeling problems”, *Numerische Mathematik*, vol. 126, no. 3, pp. 559–587, 2014 (cit. on p. 69).

- [129] U. Zwick, “The smallest networks on which the Ford-Fulkerson maximum flow procedure may fail to terminate”, *Theoretical Computer Science*, vol. 148, no. 1, pp. 165–170, 1995 (cit. on p. 65).